

AD-A148 427

RAPID SOLIDIFICATION PROCESSING AND POWDER METALLURGY
OF AL ALLOYS(U) ILLINOIS UNIV AT URBANA DEPT OF
METALLURGY AND MINING ENGINEERING H L FRASER 29 OCT 84

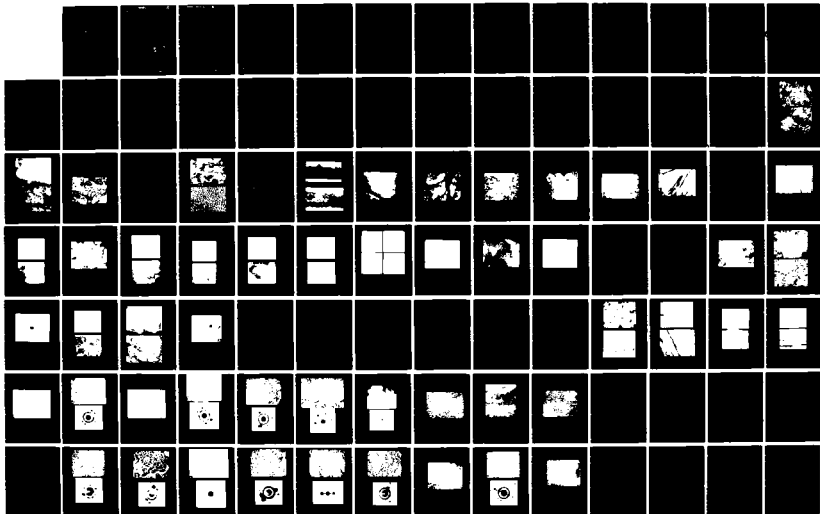
1/2

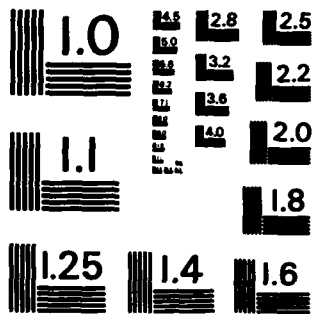
UNCLASSIFIED

AFO5R-TR-84-1018 AFO5R-82-0186

F/G 11/6

NL





MICROCOPY RESOLUTION TEST CHART
NATIONAL BUREAU OF STANDARDS - 1963 - A

UNCLASSIFIED

4

SECURITY CLASSIFICATION OF THIS PAGE

REPORT DOCUMENTATION PAGE

READ INSTRUCTIONS BEFORE COMPLETING FORM

1. REPORT NUMBER AFOSR-TR- 84 - 1018		2. GOVT ACCESSION NO.	3. RECIPIENT'S CATALOG NUMBER
4. TITLE (and Subtitle) Rapid Solidification Processing and Powder Metallurgy of Al Alloys		5. TYPE OF REPORT & PERIOD COVERED second annual technical report 15 Apr 83 to 14 Apr 84	
7. AUTHOR(s) Hamish L. Fraser		8. CONTRACT OR GRANT NUMBER(s) AFOSR-82-0186	
9. PERFORMING ORGANIZATION NAME AND ADDRESS University of Illinois, Dept. of Metallurgy 1304 W. Green, Urbana, IL 61801		10. PROGRAM ELEMENT, PROJECT, TASK AREA & WORK UNIT NUMBERS 61102F 2306/A1	
11. CONTROLLING OFFICE NAME AND ADDRESS Air Force Office of Scientific Research Bolling AFB, Bldg. 410, Washington, DC 20332		12. REPORT DATE 10/29/84	
14. MONITORING AGENCY NAME & ADDRESS (if different from Controlling Office) AD-A148 427		13. NUMBER OF PAGES 122	
		15. SECURITY CLASS. (of this report) unclassified	
		18a. DECLASSIFICATION/DOWNGRADING SCHEDULE	

16. DISTRIBUTION STATEMENT (of this Report)
This document has been approved for public release; its distribution is unlimited.

17. DISTRIBUTION STATEMENT (of the abstract entered in Block 20, if different from Report)

18. SUPPLEMENTARY NOTES

DTIC ELECTED
S DEC 10 1984 D
E

19. KEY WORDS (Continue on reverse side if necessary and identify by block number)
Rapid solidification processing of Al-alloys, powder metallurgy, dynamic powder compaction

20. ABSTRACT (Continue on reverse side if necessary and identify by block number)
On reverse side
DTIC FILE COPY

UNCLASSIFIED

SECURITY CLASSIFICATION OF THIS PAGE(When Data Entered)

During the second year of the program, there have been five areas of emphasis. These are: 1) the development of a model to describe the mechanism of formation of rapidly solidified Al alloys (i.e. zones A and B); ii) the processing of particulate whose microstructure consists entirely of zone A; iii) the microstructures of rapidly solidified particulate of alloys based on Al-8Fe; iv) the identification of metastable phases which form in some of the Al alloys studied; and v) dynamic compaction of particulate.

A simple model for the formation of rapidly solidified hyper-eutectic Al alloys has been developed. This model is based on the degree of undercooling achieved prior to nucleation and the extent to which recalescence effects may be inhibited by a rapid rate of heat-extraction. Zone A microstructures form when the temperature is lowered to below that of the extended α -Al liquidus where primary Al may be nucleated. The microstructures of rapidly solidified Al-Ni and Al-Co alloys may be interpreted satisfactorily by this model. In the case of the Al-Be system, this model represents an oversimplification of the mechanism of formation of rapidly solidified microstructures. Thus, it has been found that the microstructures of rapidly solidified hyper-eutectic alloys may be interpreted on the basis of a metastable monotectic reaction. Such an explanation is reasonable since the equilibrium hyper-eutectic liquidus exhibits a point of inflection.

Various methods for the processing of particulate consisting entirely of zone A morphology have been investigated. It was found that most powders formed by centrifugal atomization involving convective cooling by He gas contain regions of both zones A and B. This can be interpreted on the basis of the model developed for the formation of these microstructures. Thus, although the powders may be under-cooled sufficiently for the formation of zone A morphologies (i.e. below the extended α -Al liquidus), the rate of heat extraction is not sufficient to inhibit recalescence which causes the temperature to rise above the extended liquidus and in this way zone B morphologies result. Particulate consisting of entirely zone A morphologies can be produced by melt-spinning. Thus, when melt-spinning is effected with a substrate surface velocity of $\approx 35 \text{ ms}^{-1}$ and the ribbons are cast into an He environment, zone A microstructures are formed.

Ribbons of Al-8Fe-2Mo (wt.%) consisting of a zone A microstructure were produced. This microstructure was found to be essentially identical to that of the same alloy which has been laser surface melted. The same resistance to thermal decomposition was observed in samples heat-treated at 400°C for four hours. In an attempt to improve the thermal stability of the microstructure, the more slowly diffusing element Zr was substituted for Mo in these ribbons. Although the as rapidly solidified microstructures of the Zr containing ribbons were in essence identical to the case of Mo, the thermal stability was in fact somewhat inferior. V additions were also investigated, although again no improvements in thermal stability were observed.

The metastable phases which have been observed to form in rapidly solidified Al-Mn and Al-Mo have been studied. In the case of the Al-Mn alloy, the diffraction patterns recorded from the phase of interest exhibit 2-, 3- and 5-fold symmetries. A model for the structure of the phase has been developed on the basis of icosahedral symmetry, involving the twenty-fold twinning of rhombohedral cells. The metastable phase found in Al-Mo has been identified as Al_4Mo , with space group of $\text{Fd}\bar{3}\text{m}$ and lattice parameter of 7.23 \AA .

Finally, dynamic compaction of powders of Al and 7091 has been effected. The microstructures found at the prior particle boundaries have been studied using transmission electron microscopy. It is observed that dynamic recrystallization occurs as a result of dynamic compaction. Tensile tests of both Al and 7019, in both the as-compacted condition and following various heat-treatments, have been carried out. Very limited ductilities are measured which have been attributed to the presence of the hydrated oxide layer on the surfaces of the powders.

UNCLASSIFIED

SECURITY CLASSIFICATION OF THIS PAGE(When Data Entered)

Second Annual Technical Report on
Rapid Solidification Processing and
Powder Metallurgy of Al Alloys

AFOSR Grant No: AFOSR-82-0186

Progress in Research during the period

15th April 1983 to 14th April 1984

submitted by:

Hamish L. Fraser
Department of Metallurgy
University of Illinois
1304 W. Green
Urbana, IL 61801

359-56-6563

(217) 333-1975

Approved for public release;
distribution unlimited.

Accession For	
NTIS GRA&I	<input checked="" type="checkbox"/>
DTIC TAB	<input type="checkbox"/>
Unannounced	<input type="checkbox"/>
Justification	
By	
Distribution/	
Availability Codes	
Dist	Avail and/or Special
A-1	



AIR FORCE OFFICE OF SCIENTIFIC RESEARCH (AFSC)
NOTICE OF TRANSMITTAL TO DTIC
This technical report has been reviewed and is
approved for public release in accordance with AFM 190-12.
Distribution is unlimited.
MATTHEW J. KERPNER
Chief, Technical Information Division

ABSTRACT

Alpha

During the second year of the program, there have been five areas of emphasis. These are: 1) the development of a model to describe the mechanism of formation of rapidly solidified Al alloys (i.e. zones A and B); ii) the processing of particulate whose microstructure consists entirely of zone A; iii) the microstructures of rapidly solidified particulate of alloys based on Al-8Fe; iv) the identification of metastable phases which form in some of the Al alloys studied; and v) dynamic compaction of particulate.

A simple model for the formation of rapidly solidified hyper-eutectic Al alloys has been developed. This model is based on the degree of undercooling achieved prior to nucleation and the extent to which recalescence effects may be inhibited by a rapid rate of heat-extraction. Zone A microstructures form when the temperature is lowered to below that of the extended α -Al liquidus where primary Al may be nucleated. The microstructures of rapidly solidified Al-Ni and Al-Co alloys may be interpreted satisfactorily by this model. In the case of the Al-Be system, this model represents an oversimplification of the mechanism of formation of rapidly solidified microstructures. Thus, it has been found that the microstructures of rapidly solidified hyper-eutectic alloys may be interpreted on the basis of a metastable monotectic reaction. Such an explanation is reasonable since the equilibrium hyper-eutectic liquidus exhibits a point of inflection.

Various methods for the processing of particulate consisting entirely of zone A morphology have been investigated. It was found that most powders formed by centrifugal atomization involving convective cooling by He gas contain regions of both zones A and B. This can be interpreted on the basis of the model developed for the formation of these microstructures. Thus, although the powders may be undercooled sufficiently for the formation of zone

A morphologies (i.e. below the extended α -Al liquidus), the rate of heat extraction is not sufficient to inhibit recalescence which causes the temperature to rise above the extended liquidus and in this way zone B morphologies result. Particulate consisting of entirely zone A morphologies can be produced by melt-spinning. Thus, when melt-spinning is effected with a substrate surface velocity of $\approx 35 \text{ ms}^{-1}$ and the ribbons are cast into an He environment, zone A microstructures are formed.

Ribbons of Al-8Fe-2Mo (wt.%) consisting of a zone A microstructure were produced. This microstructure was found to be essentially identical to that of the same alloy which has been laser surface melted. The same resistance to thermal decomposition was observed in samples heat-treated at 400°C for four hours. In an attempt to improve the thermal stability of the microstructure, the more slowly diffusing element Zr was substituted for Mo in these ribbons. Although the as rapidly solidified microstructures of the Zr containing ribbons were in essence identical to the case of Mo, the thermal stability was in fact somewhat inferior. V additions were also investigated, although again no improvements in thermal stability were observed.

The metastable phases which have been observed to form in rapidly solidified Al-Mn and Al-Mo have been studied. In the case of the Al-Mn alloy, the diffraction patterns recorded from the phase of interest exhibit 2-, 3- and 5-fold symmetries. A model for the structure of the phase has been developed on the basis of icosahedral symmetry, involving the twenty-fold twinning of rhombohedral cells. The metastable phase found in Al-Mo has been identified as Al_4Mo , with space group of $Fd\bar{3}m$ and lattice parameter of 7.23 \AA .

Finally, dynamic compaction of powders of Al and 7091 has been effected. The microstructures found at the prior particle boundaries have been studied using transmission electron microscopy. It is observed that

dynamic recrystallization occurs as a result of dynamic compaction. Tensile tests of both Al and 7019, in both the as-compacted condition and following various heat-treatments, have been carried out. Very limited ductilities are measured which have been attributed to the presence of the hydrated oxide layer on the surfaces of the powders.

1. INTRODUCTION

This report describes the work done during the second year of a program involving the rapid solidification processing (RSP) and powder metallurgy of Al alloys. Most of the alloys studied fall into the category of intermediate (or elevated) temperature application, i.e. in the range 250-300°C (~ 480-570°F). The original program of research involved five tasks, including the microstructural response of the alloys to RSP, production of RSP particulate, dynamic powder compaction, heat-treatment and microstructural development, and finally, property evaluation. During the first year of the program, work commenced as planned on the first three of these tasks, and the progress made was described in the first annual technical report. However, as a result of that work, a number of small changes in emphasis were made (with the approval of the Technical Monitor, Dr. A.H. Rosenstein) in the research plan for the second year. The modified plan is presented below together with the reasons for the changes in emphasis where appropriate.

Three major results highlight the work of the first year. Firstly, a simple mechanism for the formation of microstructures of rapidly solidified Al alloys (i.e. zones A and B*) was formulated involving both the undercooling achieved prior to nucleation and the inhibition of recalescence during subsequent solidification. Secondly, the thermal stabilities of the zone A microstructures of Al-8Fe-2Mo and Al-7.9Fe-2.9Ce (composition in wt.%) were compared and it was shown that the Mo containing alloy exhibited a greater resistance to thermal decomposition. Finally, it was found that the optimum strength of rapidly solidified Al-8Fe alloys depends critically on the

*When samples of Al alloys are rapidly solidified and subsequently polished and etched for examination by optical metallography, in general some regions give rise to contrast whereas others are essentially featureless. These regions have been termed zones 'B' and 'A', respectively⁽¹⁾.

presence of the refined intermetallic dispersion at the intercellular (or more strictly correct, intercolumnar) regions. The main emphases of the second year's work have been aimed at an exploitation of these results. Thus, regarding the mechanism of formation of the rapidly solidified microstructures, the work has been expanded to the somewhat more complicated systems Al-Co and Al-Be. The increased resistance to coarsening of the Mo containing alloy is not well understood and so other tertiary alloying elements have been added in an attempt to determine the cause of this important effect. Finally, if optimum strengths are to be achieved in bulk pieces of these RSP alloys, it is important to be able not only to produce particulate possessing a microstructure which consists entirely of zone A, but also to subsequently consolidate this without causing coarsening of the RSP microstructure. Work during this second year has been aimed at methods of producing and consolidating such particulate. Firstly, the use of dynamic powder compaction has been continued where consolidation may be effected in the absence of a prolonged thermal excursion. Secondly, since the Mo containing alloys are fairly stable up to $\approx 400^{\circ}\text{C}$, extrusion at temperatures just less than this value (i.e. in the range $325\text{-}375^{\circ}\text{C}$ ($\approx 600\text{-}700^{\circ}\text{F}$)) may be used to consolidate the given particulate. It should be noted that extrusion has been used to compact powders at these temperatures previously⁽²⁾.

The work described below has been divided into the following five areas: the mechanism of formation of microstructures, processing of 'Zone A' microstructures, microstructures of rapidly solidified alloys based on the Al-Fe system, metastable phase formation and finally, dynamic compaction studies.

2. MECHANISM OF FORMATION OF MICROSTRUCTURES

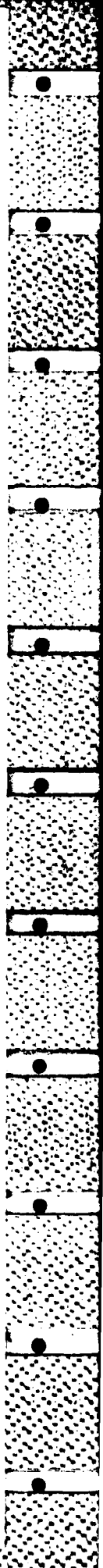
2.1 Al-Ni

During the first year's work, rapidly solidified Al-Ni alloys were studied in an attempt to determine the mechanism of formation of microstructures corresponding to zone A and zone B. Two compositions were studied, namely 3.5Ni and 8.0Ni (compositions in atomic %), and RSP was effected in each case by laser surface melting (LSM). Optical micrographs of LSM samples of the dilute alloy (3.5Ni) revealed the presence of only zone A, whereas those of the more concentrated alloy (8.0Ni) exhibited both types of microstructure. It has been found that zone A for the dilute alloy consists mainly of a cellular microstructure where the α -Al cells are ~ 0.2 - $0.5\mu\text{m}$ in diameter and surrounded by a refined precipitation of the stable intermetallic Al_3Ni . In some areas, small amounts of a micro-eutectic mixture were observed. This latter microstructure consists of a rod-like precipitation of the intermetallic compound Al_3Ni in an Al matrix. The interparticle spacing is $\sim 40\text{nm}$. These various features are shown in Fig. 1 (a,b). In contrast to these observations, zone A in the alloy containing 8.0Ni consisted mostly of the refined micro-eutectic mixture (Fig. 1c) and only small amounts of the cellular morphology (Fig. 1d). In this same more concentrated alloy, zone B has been found to consist of rather coarse primary dendrites of the intermetallic Al_3Ni with Al in the interdendritic regions (shown in Fig. 1e for the sake of completeness).

These various observations have been interpreted on the following basis. Consider the phase diagram shown in Fig. 2. The common feature between the two zone A morphologies is the presence of the continuous matrix of α -Al. Therefore, it seems reasonable to assume that the liquid metal has been undercooled, at least at the advancing solid/liquid interface, such that nucleation occurs at a temperature below the extended α -Al liquidus. Under

these conditions, it is possible for the Al solid solution to form first, especially if it is difficult to nucleate the intermetallic compound. Zone B microstructures would then correspond to the condition where the local temperature lies above the extended liquidus and so it is not possible for primary Al to form and rather the intermetallic compound nucleates as the primary phase in the form of dendrites. In a sample exhibiting both types of morphologies, it is expected that the liquid metal was undercooled initially below the extended liquidus so that zone A formed and then the subsequent liberation of latent heat of fusion caused the local temperature at the interface to increase (recalescence) above the extended liquidus so that zone B formed.

The difference in the two morphologies corresponding to zone A, i.e. mainly a cellular microstructure in the dilute alloy and mostly a micro-eutectic mixture in the concentrated alloy may be explained on the basis of an asymmetric region of coupled growth for liquids undercooled below the eutectic temperature (shown schematically as the shaded region in Fig. 2). Such asymmetry in the coupled growth region of Al-Fe alloys has been reported⁽³⁾ and postulated more recently for the case of an eutectic mixture involving a faceted phase⁽⁴⁾. For zone A to form in the Al-8.0Ni alloy, the liquid appears to have been undercooled $\approx 200^{\circ}\text{C}$. This is sufficient to permit the formation of a micro-eutectic although some cells are also produced. Therefore, the hyper-eutectic boundary of the region of coupled growth appears to lie close to the extended liquidus. For similar undercoolings, the dilute alloy (3.5Ni) appears to lie mostly outside the region of coupled growth, as shown in Fig. 2 and so the hypo-eutectic boundary of the region of coupled growth seems to lie as shown in Fig. 2. If these deductions are correct, then under the conditions imposed by LSM, an alloy containing 6.0Ni would be undercooled into the region of coupled growth such that the microstructure



would consist entirely of micro-eutectic zone A. To verify this, an Al-6.0Ni sample was rapidly solidified using LSM and the resulting microstructure is shown in Fig. 3. As can be seen, the microstructure does indeed consist of the micro-eutectic mixture, a result which helps to substantiate the present model.

In summary, based on observations of rapidly solidified Al-Ni alloys, the formation of zone A and B morphologies corresponds to undercooling of the melt either below or above the extended α -Al liquidus, respectively. Thus, if the undercooling induced by a rapid rate of heat extraction is not sufficient to reduce the temperature of the liquid below the extended liquidus, then nucleation of the intermetallic compound will occur, and a zone B morphology will result. If, however, the temperature of the liquid is reduced to below that of the extended liquidus, it is possible for α -Al to nucleate first. This is accomplished in either a cellular fashion or as a coupled micro-eutectic mixture, depending on factors such as the shape of the region of coupled growth and degree of undercooling prior to nucleation. If during solidification recalescence causes the temperature to rise above the extended liquidus then a zone B microstructure will again form. The microstructures in rapidly solidified Al-Co and Al-Be have been studied and interpreted on the basis of undercooling prior to nucleation in a similar manner to that described here. These results are described below.

2.2 Al-Co

For dilute alloys, the phase diagram of the Al-Co system possesses many of the same features exhibited by the Al-Ni system, i.e. limited solubility of Co in Al, and an eutectic at a low value of Al concentration involving an intermetallic Al_9Co_2 ; one difference involves a steeper slope of the hyper-eutectic liquidus in the case of Al-Co (see Fig. 4). It is interesting,

therefore, to determine whether similar types of microstructure occur when hyper-eutectic Al-Co alloys are rapidly solidified which may then be explained on the basis of the model described above. In fact, such alloys have been rapidly solidified using melt-spinning by Garrett and Sanders⁽⁵⁾. Their observations and conclusions may be summarized as follows (presented in bold print so that they may be differentiated easily from the results and discussion of the present work). Four alloys were studied, namely Al with 2.5, 5.0, 7.5, and 10.0 at.%Co, respectively. For melt-spinning using a Cu wheel with a surface speed of $\approx 36\text{ms}^{-1}$ and casting into air, optical metallography was used to show that the ribbons contained a region of zone A corresponding to where the ribbon had been in contact with the wheel; the extent of the region of zone A increased with decreasing solute content. The remaining parts of the ribbons exhibited a microstructure consisting of zone B. TEM revealed that the zone A regions consist of an extremely refined cellular structure. In addition to this refined morphology, many larger particles of Al_9Co_2 were observed. These large particles are surrounded by a small region of α -Al which is depleted apparently in Co. The micro-cellular morphology was found to be adjacent to these regions of α -Al. A model is presented in which it is thought that these large intermetallic particles nucleate directly from the melt and grow subsequently.

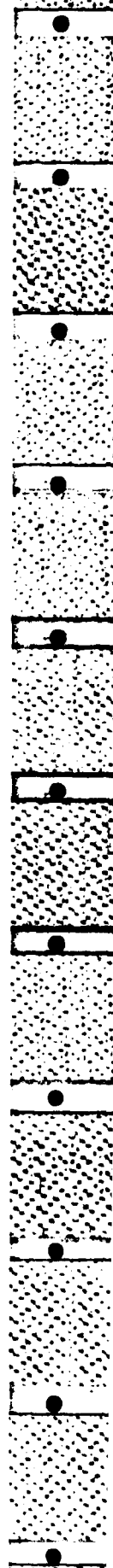
The model of Garrett and Sanders is not in agreement with that presented above based on the results of rapid solidification of Al-Ni alloys. Moreover, the presence of large intermetallic particles surrounded by a refined zone A microstructure is difficult to understand in view of the effect of the latent heat of fusion which would be liberated by the relatively extensive growth of such intermetallic particles. In view of this, as part of the present work two alloys, namely 3.5 and 5.0 at.%Co, were reduced to ribbons by melt-spinning. In the case of the former, melt-spinning was effected in two ways,

firstly by producing ribbon in a vacuum and secondly by using an He environment, so that the rate of heat extraction was varied. Optical micrographs of the ribbons of alloys containing 3.5Co produced in this way are presented in Fig. 5 (a,b). As can be seen, the ribbon produced using an He environment consists largely of areas that do not respond to etching (zone A), whereas the ribbon which was melt-spun into a vacuum (the slower of the two rates of heat extraction) exhibits regions of both zones A and B. The ribbon of the more concentrated alloy, 5.0%, produced by spinning into an He environment was found to consist mainly of zone A. It is immediately apparent that melt-spinning into an He environment produces ribbon with a more uniform and attractive (zone A) microstructure. In the case of the alloy containing 3.5 at.%Co, the zone A is shown in Fig. 6 and is found to be composed of an extremely refined cellular microstructure, the cells being based on α -Al, and the intercellular precipitates being Al_9Co_2 , in agreement with the observations of Garrett and Sanders. In the case of the melt-spun ribbon cast into vacuum, the zone B microstructure consists of large primary particles of Al_9Co_2 with α -Al in the extensive interdendritic regions, as shown in Fig. 7. The morphology of the intermetallic particles is rather different from those observed by Garrett and Sanders and it should be noted that the microstructure surrounding the particles is also different in the two cases. For the alloy containing 5.0 at.%Co, the zone A microstructure involves a **coupled growth** mixture of Al and Al_9Co_2 (Fig. 8). Only very occasionally was a large intermetallic particle observed which exhibited the same morphology as that referred to by Garrett and Sanders, one such being shown in Fig. 9. These particles have been identified as Al_9Co_2 by use of selected area diffraction although it was found that a number of reflections were present which should have been kinematically forbidden according to the special restrictions associated with the particular space group ($P2_1/c$) and positions of atoms within the cell. This discrepancy is being investigated further.

In the main, the observations of the microstructures which form in melt-spun ribbons (MSR) of the Al-Co alloys studied here are very similar to those observed in the Al-Ni alloys. Thus, at relatively low concentrations ($\approx 3.5\text{Co}$), zone A consists of a very refined cellular microstructure, whereas zone B appears to consist of large primary particles of Al_9Co_2 surrounded by interdendritic Al. As the Co content is increased to $\approx 5.0\%$, it appears that the alloy can be undercooled into the region of coupled growth which is expected to exhibit an asymmetry in a similar fashion to that of the case of Al-Ni. These various microstructures are essentially the same as those observed in the Al-Ni alloys studied and their occurrence can be explained using the same model described above.

The main difference between the microstructures observed in the two alloy systems involves the large stellated particles seen rather frequently by Garrett and Sanders and very infrequently in the present work. The presence of these particles cannot be accounted for on the basis of the model presented here. Garrett and Sanders have concluded that these particles nucleate directly from the liquid, and are therefore a form of zone B. There are three problems associated with their interpretation. Firstly, these authors show a TEM micrograph taken from the wheel-side of the ribbon, which should possess a zone A morphology; some of the large intermetallic particles appear to be present in this micrograph. Secondly, these particles appear to be surrounded by the extremely refined cellular microstructure characteristic of zone A. If the particles had nucleated directly in the liquid and grown to these relatively large sizes, it is probable that the latent heat of fusion liberated would have caused recalescence inhibiting the formation of zone A. Thirdly, the zone B morphology has been studied in the present work and the intermetallic Al_9Co_2 is seen to exhibit a rather different morphology than the stellated intermetallic particles. For these reasons, it is unlikely that

these large particles are nucleated directly in the liquid. It is more likely that they are present in the liquid at the beginning of the melt-spinning process. Thus, when the prealloyed stock is melted in the quartz crucible, after becoming molten, it will take some finite period for the large primary intermetallic dendrites to be completely dissolved. It is possible, then, for the casting of the melt-spun ribbons to be commenced before the alloy is completely liquid. In this case, the stellated particles would correspond to the partially remelted dendrites of Al_3Co_2 . The presence of a region adjacent to these particles which is denuded in Co may be understood simply in terms of a small amount of regrowth of the particles during the melt-spinning process. Finally, the observation of the adjacent zone A morphology implies insignificant recalescence and therefore little growth of the particles. It is of interest to understand why rapid growth does not occur once undercooling begins if these particles are already present in the liquid. The implication is that the growth rate of the intermetallic compounds is relatively low. Some evidence for this is afforded by observations of LSM samples of Al-Ni. Thus, it can be seen in the optical micrograph shown in Fig. 10 that in the regions of the melt-pool adjacent to the substrate, pieces of unmelted primary dendrites of Al_3Ni are trapped in the rapidly solidified volume. One such particle is shown in Fig. 11, and it can be seen that it is surrounded by a region depleted in Ni, presumably corresponding to some growth of the particle. However, most of the solidified material has formed the microeutectic mixture associated with zone A. The size of the large intermetallic dendrite is approximately the same as that of those found in the substrate, indicating that little growth has occurred. It can be concluded that, although the intermetallic phase was already present in the liquid, sufficient undercooling was achieved so that zone A microstructures could form. The growth rate of the pre-existing particle must have been low so that recalescence effects were negligible.



It is concluded, then, that the microstructural responses of hyper-eutectic alloys in the Al-Co system show a marked similarity to those observed with Al-Ni alloys. The various microstructures formed can be interpreted on the basis of the model described above, involving undercooling of the liquid below (zone A) or above (zone B) the extended hyper-eutectic Al liquidus. In this way, zone A is interpreted as involving primary nucleation of α -Al whereas zone B corresponds to the primary nucleation of the appropriate intermetallic compound. In zone A, once solidification of the Al begins, the rate of extraction of heat must be sufficient to inhibit the effects of recalescence caused by the liberation of latent heat of fusion associated with the growing crystalline phases. If recalescence causes the local liquid temperature at the solid/liquid interface to increase above the extended liquidus, then the solidification mode changes and nucleation of primary intermetallic phases will occur, i.e. zone B.

2.3 Al-Be

The Al-Be system exhibits many of the same characteristics as those associated with the two alloys described above. However, there are two significant differences. Firstly, the eutectic mixture involves solid solutions (both with extremely limited solubilities) based on Al and Be, whereas the systems described above involved intermetallic compounds which are apparently difficult to nucleate. Secondly, the equilibrium Be liquidus exhibits a point of inflection so that some metastable reactions may be expected as a result of rapid solidification⁽⁶⁾ (see Fig. 12). For these reasons alloys taken from this system were reduced to rapidly solidified ribbons by melt-spinning.

Al-Be alloys with nominal compositions of 4.4, 5.8 and 20.0% (in at.%) were prepared by induction melting under an atmosphere of argon and chillcast into

carbon molds. Melt-spun ribbon was produced by induction heating and ejecting the molten alloys onto a 15 cm (diameter) Cu wheel having a surface velocity of 35 m/s. The three alloys, having between 100 and 200°C of superheat, were ejected from a graphite crucible into an He environment. In addition, ribbon of the Al-20.0Be alloy was produced by melting in a silica-glass crucible under vacuum. He gas was introduced as the melt was ejected from the crucible. The average thickness of the ribbons was less than 40 μm . Ribbons for heat treatment were encapsulated in silica-glass under a partial pressure of argon. Heat treatment was performed in a box furnace with a controlling thermocouple next to the encapsulated specimen. The specimen temperature was controlled to $\pm 5^\circ\text{C}$.

2.3.1 Microstructure of As-Cast Material

The microstructure of as-cast hyper-eutectic alloys consists of rather coarse pro-eutectic dendrites of Be with the interdendritic material being an eutectic mixture of α -Al and Be; an example is shown schematically in Fig. 13 for the case of Al-20.0Be. This microstructure may be interpreted on the basis of the equilibrium phase diagram shown in Fig. 12. An alloy of composition Al-4.4Be was heat-treated for 1 hour at a temperature of 640°C, just below that at which the eutectic reaction occurs, to maximize the amount of Be in solid solution, then quenched and aged subsequently at 300°C for 30 mins. The resulting microstructure is shown in Fig. 14a. Small particles exhibiting weak contrast are visible (barely) although no discernable intensity maxima which could be attributed to the presence of these precipitates were evident in diffraction patterns. These small particles are thought to be Be, their precipitation being caused by the rapid decrease with temperature in the solid solubility of this element in Al. The lack of diffracted intensity from the particles is consistent with their small size and the low scattering cross-section of Be. However, they may be imaged more readily using weak-beam dark-field (WBDF) microscopy⁽⁷⁾ which, in this case, relies on the strain fields associated with the lattice mismatch between matrix and precipitate and such an image is shown in Fig. 14b.

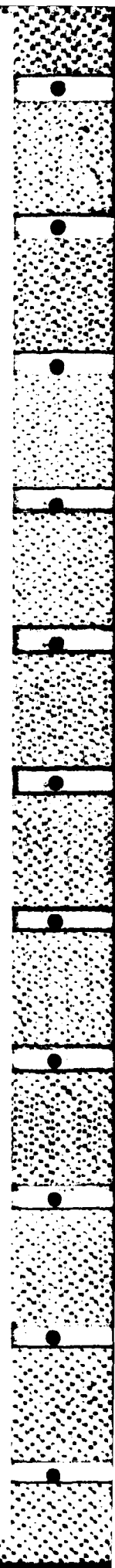
2.3.2 Microstructures of Melt-spun Ribbons

As mentioned above, the alloys 4.4, 5.8 and 20.0 Be were reduced to ribbons by melt-spinning. The microstructure of the most dilute alloy, 4.4 Be, is shown in Fig. 15 and consists of a cellular structure, based on α -Al, with some precipitation visible at the intercellular regions. These various features of the microstructure are revealed more clearly in the bright-field and WBDF transmission electron micrographs shown in Fig. 16 (a and b). The intercellular precipitation consists of a refined dispersion of small particles which have been identified as Be using selected area diffraction and dark-field imaging. One of these dark-field micrographs recorded using the $1\bar{2}10$ reflection of Be (as indicated) is shown in Fig. 17 (a and b). It may be noticed that only a few of the particles are in contrast in the dark-field micrograph (Fig. 17b). Although this observation may imply an absence of an orientation relationship, it has been determined elsewhere⁽⁸⁾ that up to six such relationships exists. Therefore, only those particles exhibiting one of the six relationships will be visible in Fig. 17b. In addition to these microstructural features, there are some heterogeneities within the cells which may be distinguished (Fig. 16). These defects appear to be either faulted or perfect prismatic dislocation loops and this is confirmed by the detailed analysis given in Fig. 18 for the fringed defects, and Fig. 19 for the perfect loops. The nature of each of the two types of loops have been determined by noting the sense of the change of image position on reversal of the sign of the diffracting vector⁽⁹⁾, after ensuring that the orientations of the non-edge loops were in a 'safe' region⁽¹⁰⁾. The results of the experiment are shown in Fig. 18 (c,d) and 19 (c,d) and in both cases are consistent with the loops being vacancy in nature. It seems reasonable to assume that a supersaturation of vacancies is retained during the initially rapid rate of cooling associated with melt-spinning, and that these excess defects cluster to form loops during the slower rate of cooling which occurs at the end of the process.

It is of interest to determine whether a supersaturation of Be, greater than the maximum solid solubility indicated in the phase diagram, had been produced in the matrix regions of these rapidly cooled ribbons. This has not been possible to do in a quantitative manner because of the difficulties associated with the detection of Be on a fine scale (i.e. the need to use electron energy loss spectroscopy). However, in way of a comparison with conventionally processed material, samples were heat-treated for 30 mins at 300°C to cause precipitation of the Be which may have been supersaturated during the rapid cooling. The results of this heat-treatment are shown in the WBDF micrograph of Fig. 20. Clearly visible is a refined distribution of small particles, which are assumed to be Be. There appears to be a greater volume fraction of precipitates formed in this case compared to that of the solution-treated and similarly aged alloys (Fig. 14), although it must be emphasized that this has not been quantitatively established.

The microstructure typical of that of the Al-5.8Be ribbon is shown in Fig. 21. In the main, there is a refined distribution of small particles with diameters ≈ 50 Å and interparticle spacing of ≈ 200 Å within a matrix of α -Al. Again, selected area diffraction and dark-field imaging have been used to reveal that these particles are Be, an example of one of the dark-field images being shown in Fig. 22. In addition to these small particles, there are a few larger precipitates (≈ 200 -300 Å in diameter), also of Be. There is some evidence of a zone, denuded of the smaller particles, surrounding each of these larger precipitates.

There is, then, an interesting variation in the microstructure of these two melt-spun alloys which is not easily explained on the basis of the equilibrium phase diagram. Thus, predictions on the basis of equilibrium conditions would suggest the formation of pro-eutectic dendrites of Be, similar to that shown in Fig. 13. In fact, the microstructure changes from one involving a cellular



morphology with a refined dispersion of precipitates in the intercellular regions to another exhibiting a moderately uniform and refined precipitation throughout the cells, and presumably these are a consequence of the rapid extraction of heat associated with melt-spinning. Recently, it has been shown that an important parameter affecting phase formation and microstructural development in rapidly solidified alloys is the degree of undercooling achieved prior to nucleation^(11,12). In the case of melt-spinning of Al-Ni alloys it was found that a liquid undercooling of ≈ 150 -200 K may be achieved during melt-spinning⁽¹³⁾. The microstructure of the most dilute alloy in the present study is consistent with undercooling of the liquid prior to nucleation below the extended α -Al liquidus so that α -Al might then be the first solid to form. However, it is not clear why increasing the solute concentration by such a small amount in the present case would yield anything but a similar microstructure and it is concluded that the formation of these structures may not be explained satisfactorily on this basis.

It is important to consider other possible metastable phase reactions that might occur when hyper-eutectic liquids are undercooled. Perepezko and Boettinger⁽⁶⁾ have suggested that for an equilibrium system with an eutectic reaction, involving limited solubility and a liquidus exhibiting a point of inflection, it is possible for a miscibility gap to form in the liquid which has been undercooled. In fact, metastable immiscibility for undercooled liquids has been demonstrated by Nakagawa⁽¹⁴⁾ in the Cu-Fe and Cu-Co alloy systems, where the equilibrium transformations involve a peritectic reaction. A schematic metastable phase diagram suggested previously⁽⁶⁾ is shown in Fig. 23. (For the sake of clarity, reactions occurring on the metastable diagram will be denoted in the following text in bold print.) As can be seen, for dilute compositions a **monotectic** reaction would be predicted for undercooled liquids. This prediction can then be used to explain the variation in microstructures observed in melt-

spun Al-4.4Be and Al-5.8Be alloys. Thus, it appears that the alloy containing 5.8Be is at or close to the monotectic reaction itself since its microstructure consists of a refined and uniform distribution of Be particles. In this case, the more dilute alloy (4.4 Be) corresponds to an **hypo-monotectic** composition. Using a simple extrapolation of the α -Al liquidus to ≈ 5.8 Be, yields a monotectic temperature of $\approx 625^\circ\text{C}$. The undercoolings expected to occur during melt-spinning would cause both alloys to be cooled to a temperature below the monotectic. For the dilute alloy, a cellular structure based on α -Al is expected to form with the liquid in the intercellular regions undergoing the monotectic reaction when its composition corresponds to coupled growth. The products of such a reaction may be initially tubes of L_2 (the liquid product of the monotectic reaction), and therefore rods of Be, or present in the form of small discrete particles. The type of microstructure which forms depends on several factors and these have been discussed by Grugel and Hellawell⁽¹⁵⁾. In particular, as the growth velocity increases, there is a tendency for the tubes of L_2 to be 'pinched-off' to form discrete particles. This factor is important in the present case since interface velocities are expected to be high in undercooled liquids. Therefore, the present observations are considered to be consistent with the products of a monotectic reaction.

If indeed a metastable monotectic reaction exists for the case of undercooled liquids, it should be possible to melt-spin more concentrated **hyper-monotectic** alloys and show the presence of the **pro-monotectic** reaction. It is important that the alloy composition be chosen such that undercooling into the region of miscibility occurs. It is necessary, therefore, to estimate the height of the miscibility gap by calculating the approximate value of Δ , which describes the temperature difference between the maximum in the region of liquid immiscibility and the equilibrium liquidus at that composition (assumed⁽⁶⁾ to be given by $X_{Al} = 0.5$, where X_{Al} is the atom fraction of Al). This may be

calculated following the method described by Perepezko and Boettinger⁽⁶⁾.

Thus, Δ is given by

$$\Delta = \frac{L_B + 0.5 R T_C}{2RT_L} \cdot [-dT_L/dX]_{X_{Al} = 0.5} \quad (1)$$

where L_B is the latent heat of fusion for the formation of Be, R is the gas constant, T_C is the consolute temperature of the miscibility gap, and T_L is the liquidus temperature. When the relevant data for the Al-Be system, ($L_B = 2919 \text{ cal.K}^{-1} \cdot \text{mole}^{-1}$ ⁽¹⁶⁾) is substituted into equation (1), it is found that $\Delta = 60\text{K}$. Using this value, other data from the equilibrium phase diagram, and assuming⁽⁶⁾ the consolute miscibility temperature occurs at $X_{Al} = 0.5$, it is possible to sketch a metastable phase diagram for the system Al-Be. This is shown in Fig. 24.

From a consideration of this diagram (Fig. 24) for melt-spinning of Al-20.0Be, it is expected that phase separation will occur within the miscibility gap ($L_1 + L_2$) as soon as the temperature is lowered below that of the spinodal point. In the particular case considered here, L_1 will form a continuous liquid while L_2 will be present initially as a series of discrete droplets. From an analogy with the behavior of immiscible liquids studied elsewhere⁽¹⁷⁾, it is expected that these small discrete particles will tend to coalesce. The extent to which such coalescence occurs will depend on the cooling rate since fast rates of heat extraction will inhibit this coarsening behavior. The microstructure of alloys of hyper-monotectic composition are expected then to be sensitive to cooling rate and to demonstrate this effect, melt-spun ribbons of Al-20.0Be were processed using two different heat extraction rates. A general view of the microstructure of melt-spun ribbon of Al-20.0Be processed by using a silica-glass crucible and introducing He at the beginning of the melt-spinning run (the slower of the two rates of heat-extraction) is shown in Fig. 25. At higher magnification, it can be seen that the microstructure consists of a bimodal

distribution of particles, Fig. 26 (a and b). While the matrix phase is based on α -Al, the smaller particles resemble those shown in Fig. 21; indeed SAD studies reveal that these particles are Be. The larger precipitates, on the scale of ≈ 0.1 - $0.15 \mu\text{m}$ in size, may also be identified uniquely as Be by using micro-diffraction techniques. Thus, a SAD pattern recorded from one of the large particles with the electron beam aligned parallel to $[1\bar{2}10]$ is shown in Fig. 27. The diffraction maxima may be indexed on the basis of Be. It is concluded that this microstructure consists of a bimodal distribution of Be particles. When one of the larger particles is examined in detail, Fig. 28, contrast features similar to very small precipitates may be distinguished. If this same large particle is imaged in dark-field with the Be $10\bar{1}0$ diffraction vector excited, these very small precipitates are clearly visible (Fig. 28). They are about $\approx 30 \text{ \AA}$ in size and in this projection exhibit approximately square cross-sections. It was not possible to observe any extra intensity maxima in the diffraction patterns corresponding to this phase. The microstructure of ribbons processed at the more rapid rate of heat extraction (using a graphite crucible and an atmosphere of He) is shown in Fig. 29 (a and b). As can be seen, there is a smaller number of large particles and a significantly increased number of small particles.

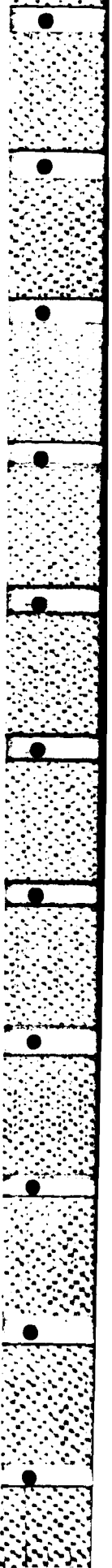
These various observations of the microstructure of melt-spun Al-20.0Be may be interpreted readily on the basis of the metastable monotectic reaction. Thus, as the temperature of the rapidly cooled liquid is lowered below the spinodal point for this composition, phase separation occurs, i.e. $L \rightarrow L_1 + L_2$. On further cooling the proportion of L_2 increases until the monotectic temperature is reached. At this point, the remaining liquid L_1 transforms cooperatively to α -Al and L_2 . Eventually, the liquid L_2 solidifies by an eutectic reaction involving α -Al and Be. On this basis, the origin of the bimodal distribution of particles observed in Fig. 26 may be understood by speculating that the larger particles

are the result of the **pro-monotectic** reaction, whereas the smaller precipitates are formed during the **monotectic** reaction itself. It may be expected that in the ribbon produced at slower rates of heat extraction, the **pro-monotectic** particles will be large since, as mentioned above, coalescence of droplets may occur. It may be noted (Fig. 26) that the larger particles tend to possess irregular shapes and this is certainly consistent with the notion of droplet coalescence. More convincing evidence for droplet coalescence is shown in Fig. 30. In the case of the ribbon produced at higher rates of heat extraction (Fig. 29), the extent to which coalescence may occur is expected to be limited kinetically. In this way, it is possible to understand the presence of a decreased number of larger particles and an increased number of smaller particles.

It is tempting to account for the observation of extremely small precipitates contained within the large Be particles on the basis of the reaction (which would be expected to occur as the **pro-monotectic** L_2 solidifies). In this case, the very small precipitates would be α -Al but this has not been determined experimentally. For example, no extra diffraction information from these precipitates could be obtained; however, their volume fraction is extremely small and, therefore, this result is not surprising. The following indirect evidence may be offered to support the assumption concerning their identity. Thus, it may be noted that their shapes approximate to square cross-sections in the projection given in Fig. 28. This implies some sharing of symmetry elements⁽¹⁸⁾, and when both the point groups of each phase (Al and Be) and possible lattice matching are considered the following element of the orientation relationship may be suggested:



In this case, a common $2/m$ symmetry axis is shared, which is consistent with the observed particle shape, and the interplanar spacings are 1.98 \AA and 4.05 \AA (Al). If this orientation relationship is correct, then the $10\bar{1}0_{\text{Be}}$ and 200_{Al} diffracting vectors will both be contained within the objective aperture so that during dark-field imaging such as in Fig. 28, the Al particles will be clearly visible. This is at least consistent with the present argument. Alternatively, these very small phases may be BeO, since the interplanar spacing of the $\{10\bar{1}\}$ in this material is 2.06 \AA . Using the same argument as above, if one set of these planes were parallel to the $\{10\bar{1}0\}$ in Be, both types of crystal would be visible in the dark-field image of Fig. 28. However, this is not considered to be as satisfactory an explanation as that involving α -Al since there is no common symmetry element shared when these particular planes of BeO and Be are parallel to one another.



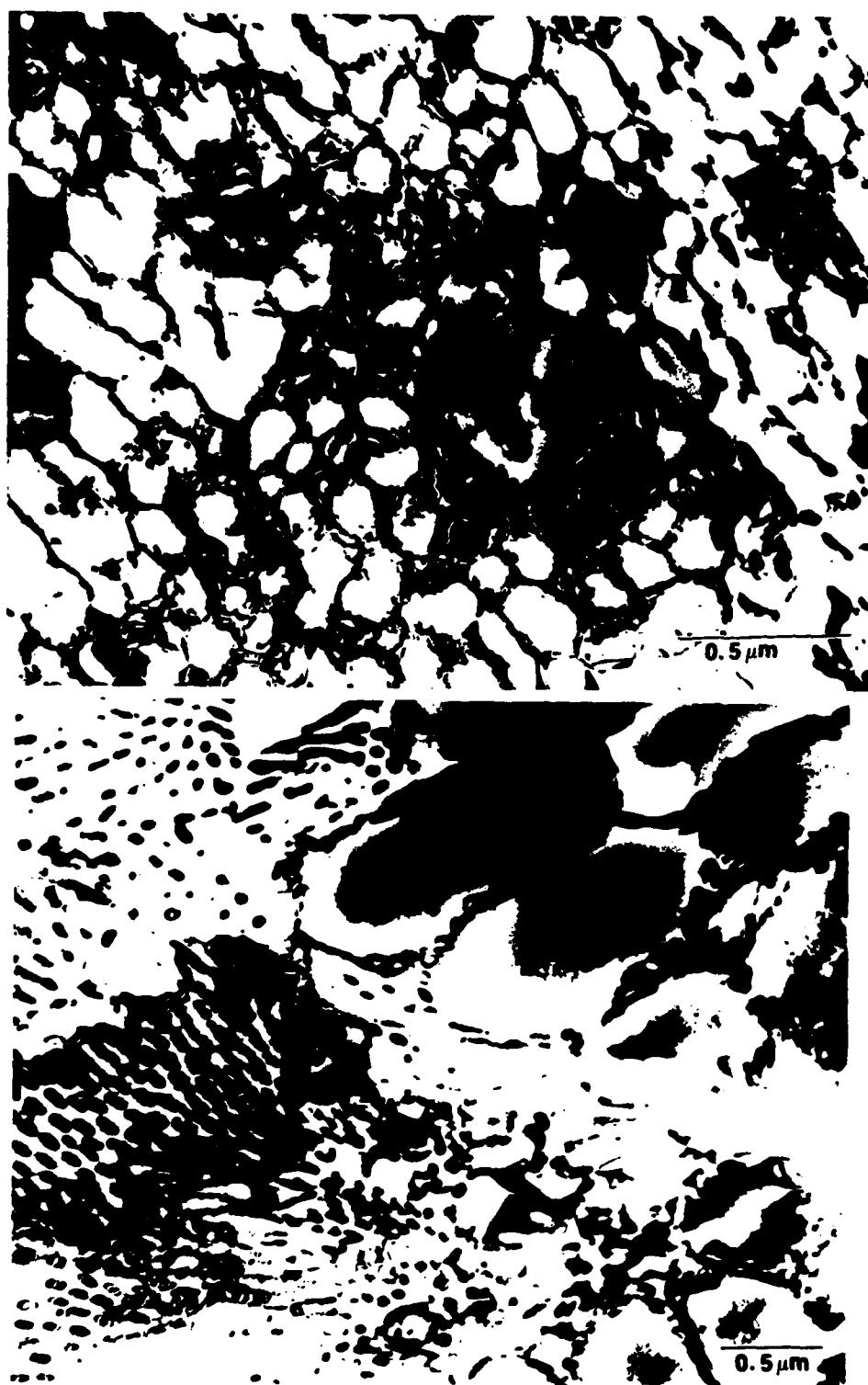


Fig. 1 TEM micrographs of laser surface melted aluminum-nickel alloys:
a) 3.5 at.%Ni zone A consisting of a cellular primary α -Al structure
b) 3.5 wt.%Ni zone A exhibiting some microeutectic mixture and a cellular region.

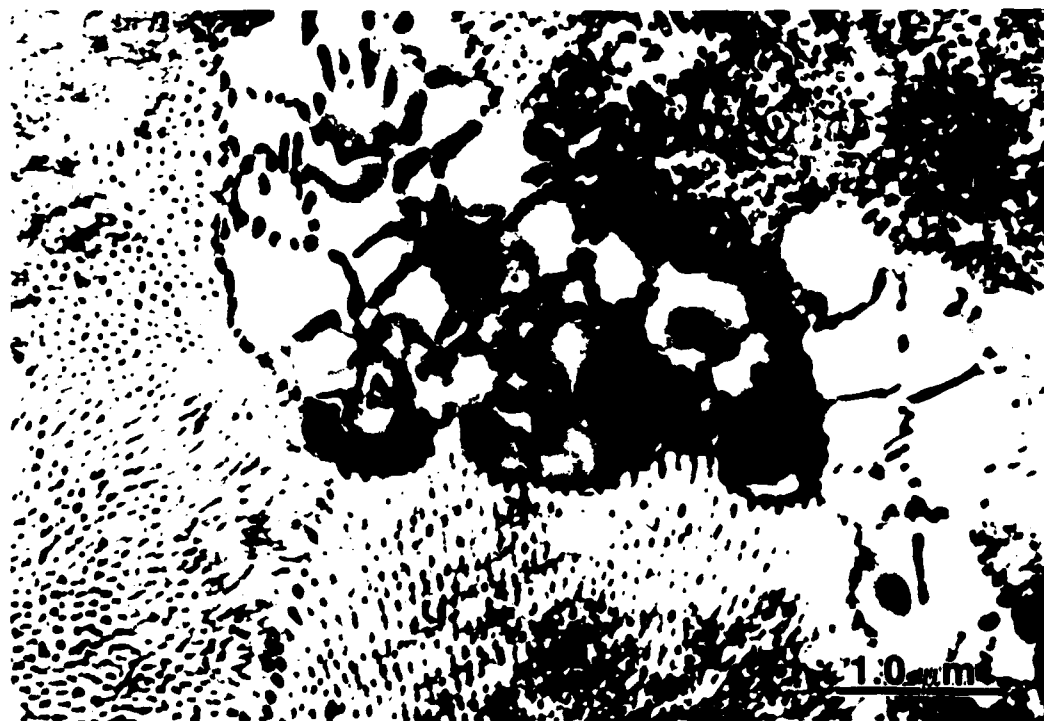


Fig. 1 c) 8.0 at.%Ni zone A showing the predominantly microeutectic structure
d) 8.0 at.%Ni zone A showing both microeutectic and cellular region.



Fig. 1 e) 8.0 at.%Ni zone B region showing large primary dendrites of Al₃Ni intermetallic compound.

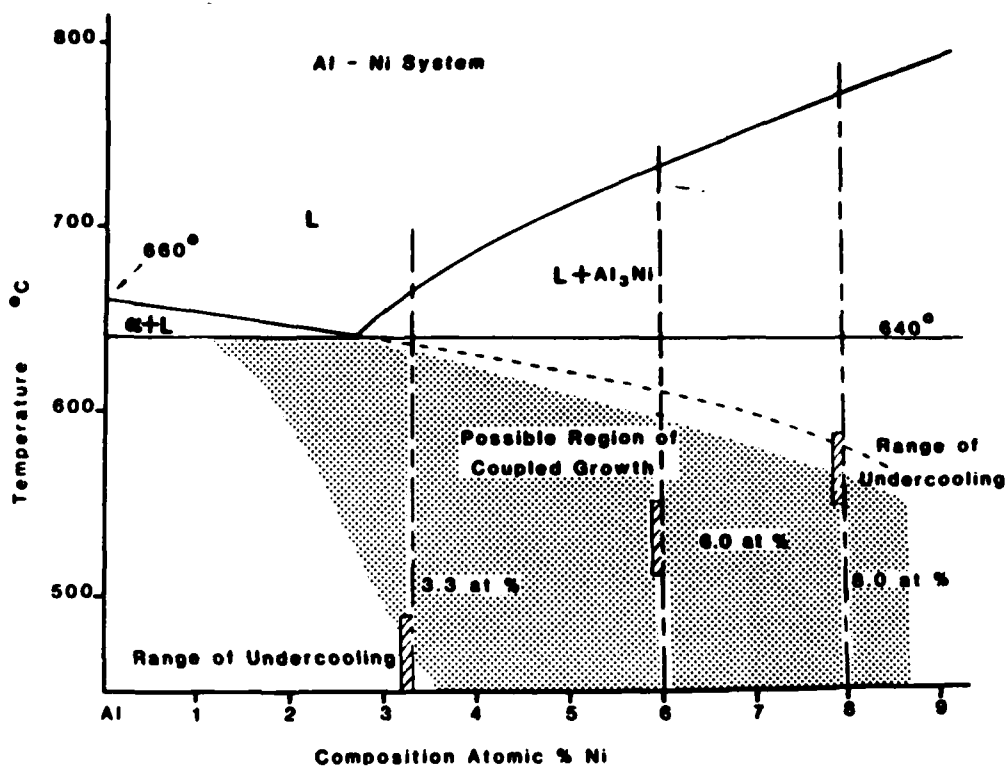


Fig. 2 Phase diagram of the Al-rich part of the Al-Ni binary system. Also shown are the extended --Al liquidus and asymmetric coupled growth region.

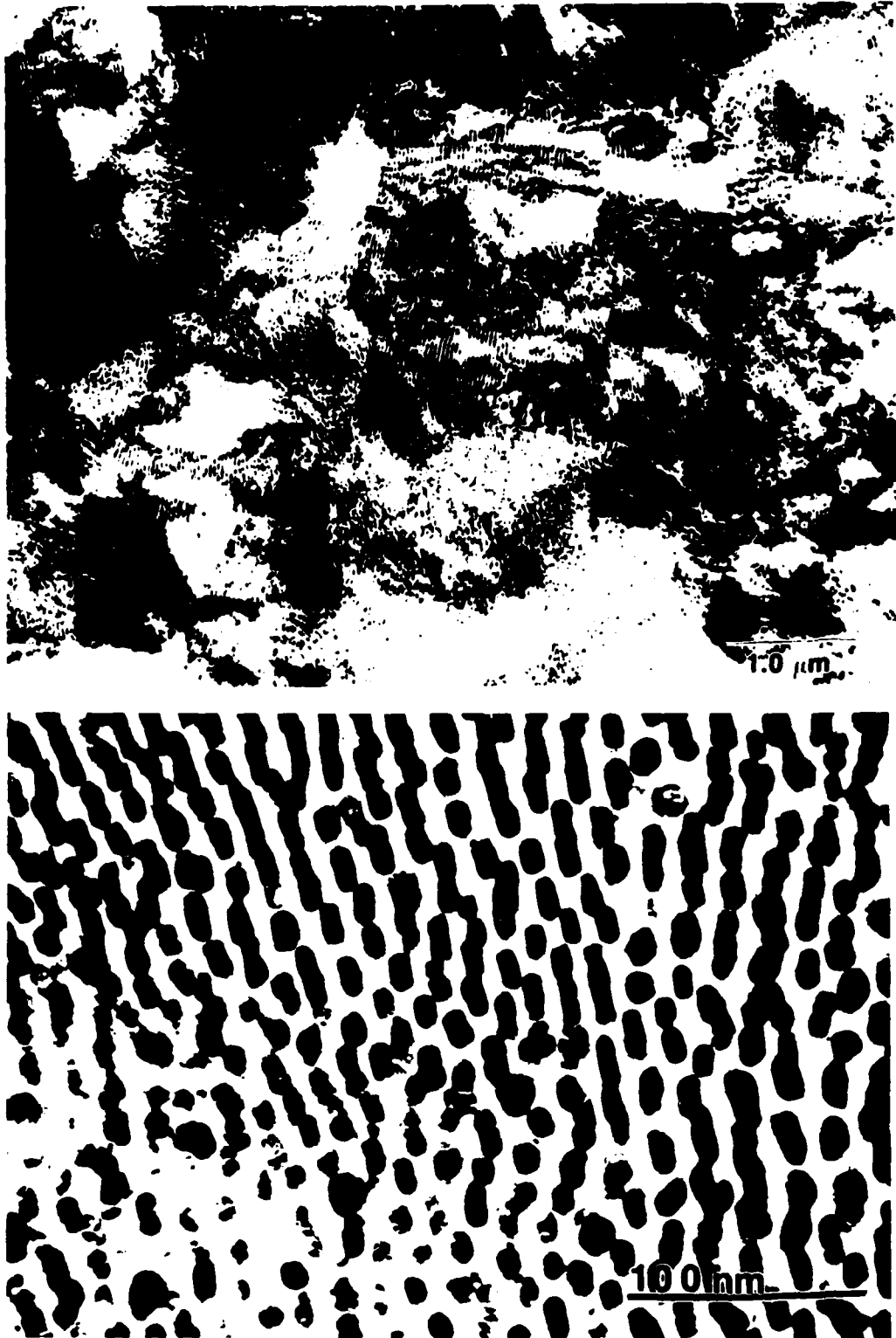


Fig. 3 TEM micrograph of laser surface melted Al-6.0at.%Ni consisting only of the microeutectic morphology. a) Micrograph of a large region. b) Micrograph showing fine structure micro-eutectic.

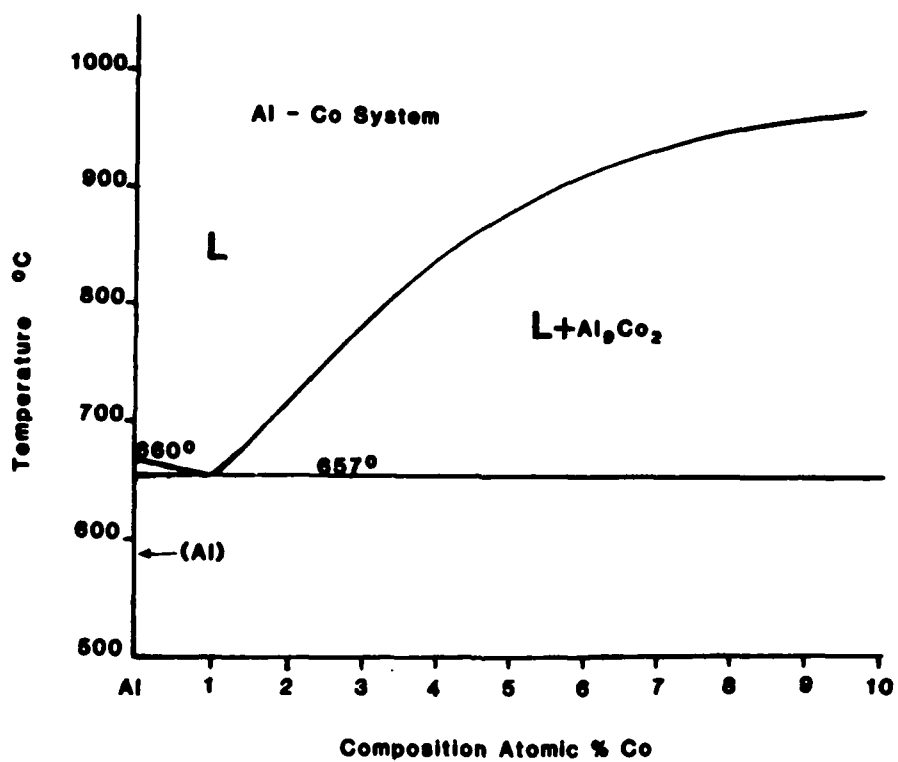


Fig. 4 Phase diagram of the Al-rich part of the Al-Co binary system.

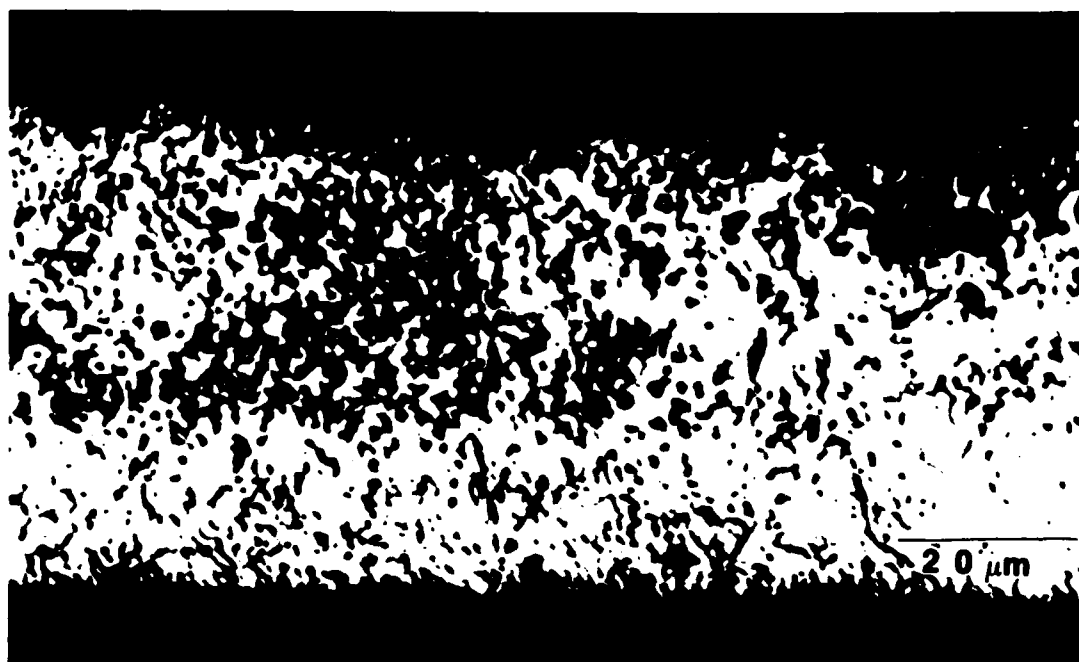
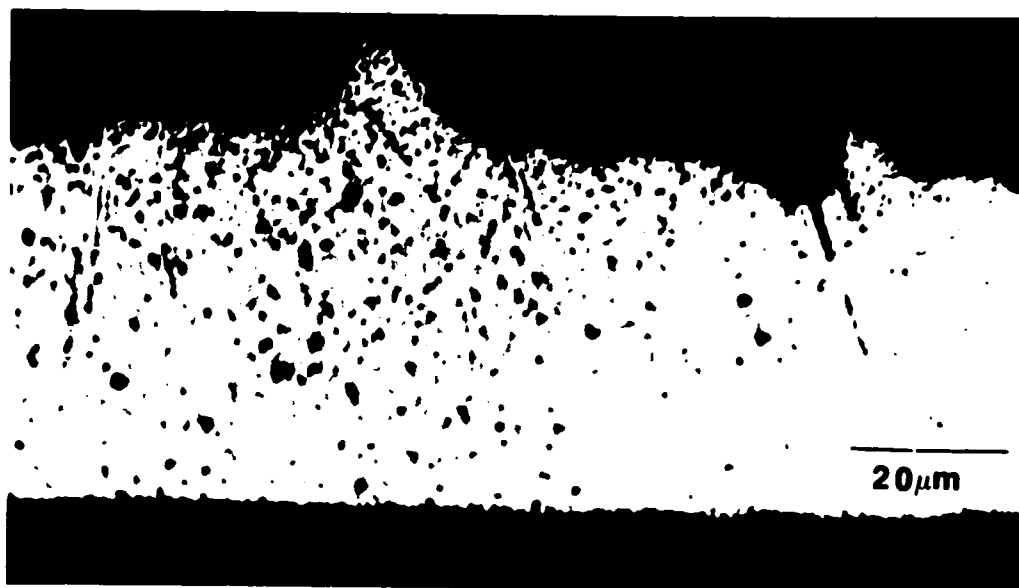


Fig. 5 Opticals of Al-3.5at.%Co melt spun ribbon:
a) spun in helium
b) spun in vacuum

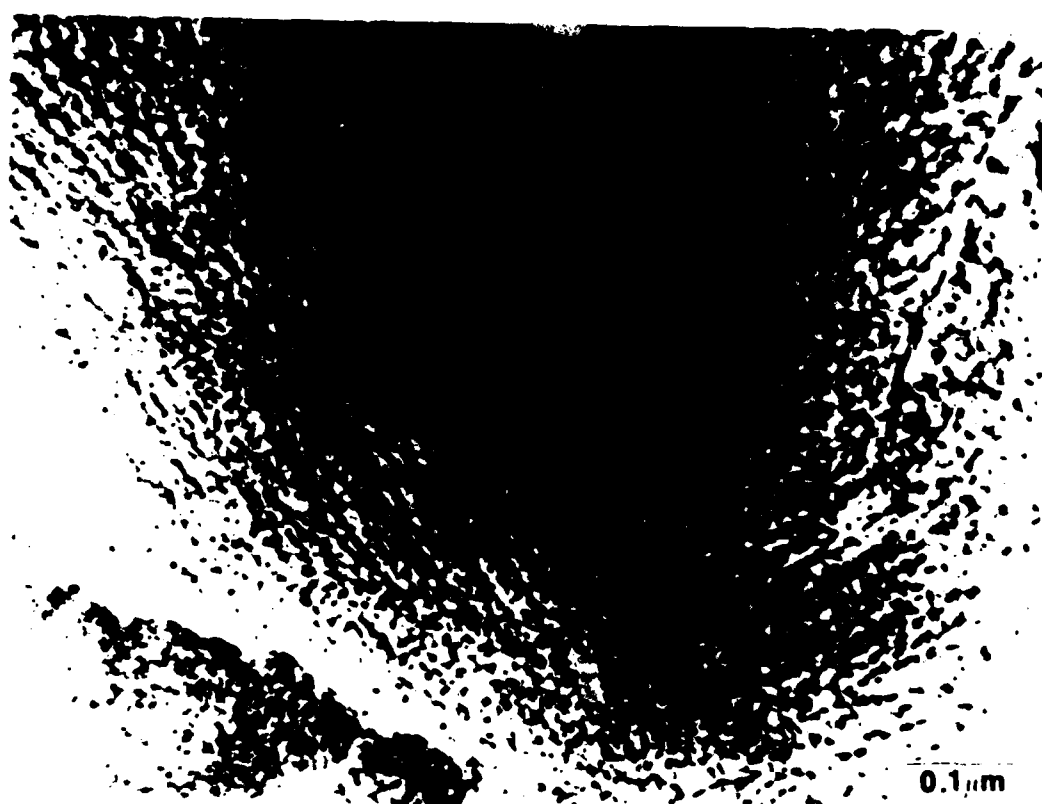


Fig. 6 TEM micrograph of Al-3.5at.%Co melt spun ribbon.

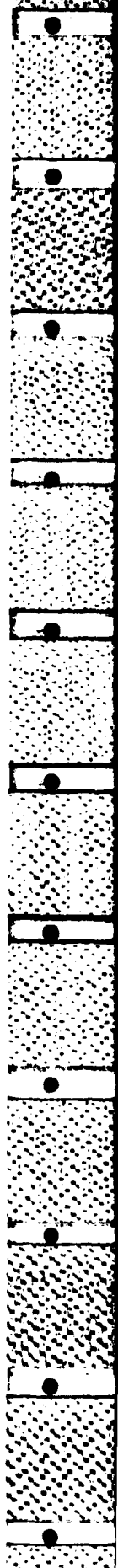




Fig. 7 TEM micrograph of Al-3.5at.%Co melt spun ribbon spun in vacuum showing zone B microstructure.

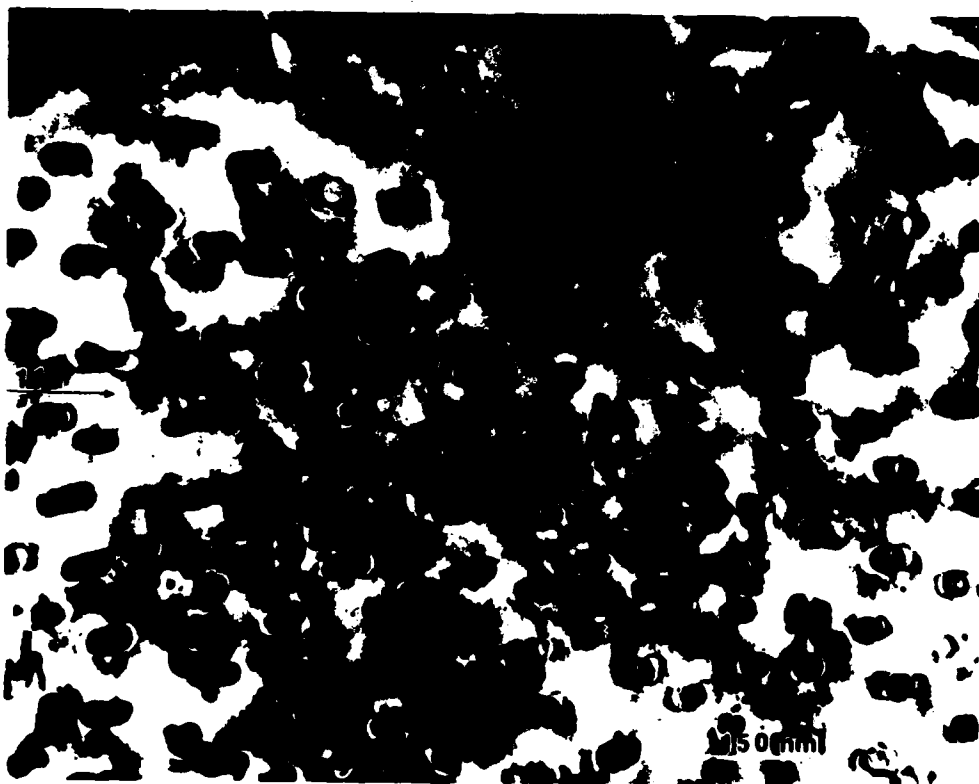


Fig. 8 TEM micrograph of melt spun ribbon of Al-5.0at.%Co showing region of coupled growth.



Fig. 9 TEM micrograph of melt spun ribbon of Al-5.0at%Co. A large stellated particle of Al_9Co_2 is present in the micrograph.

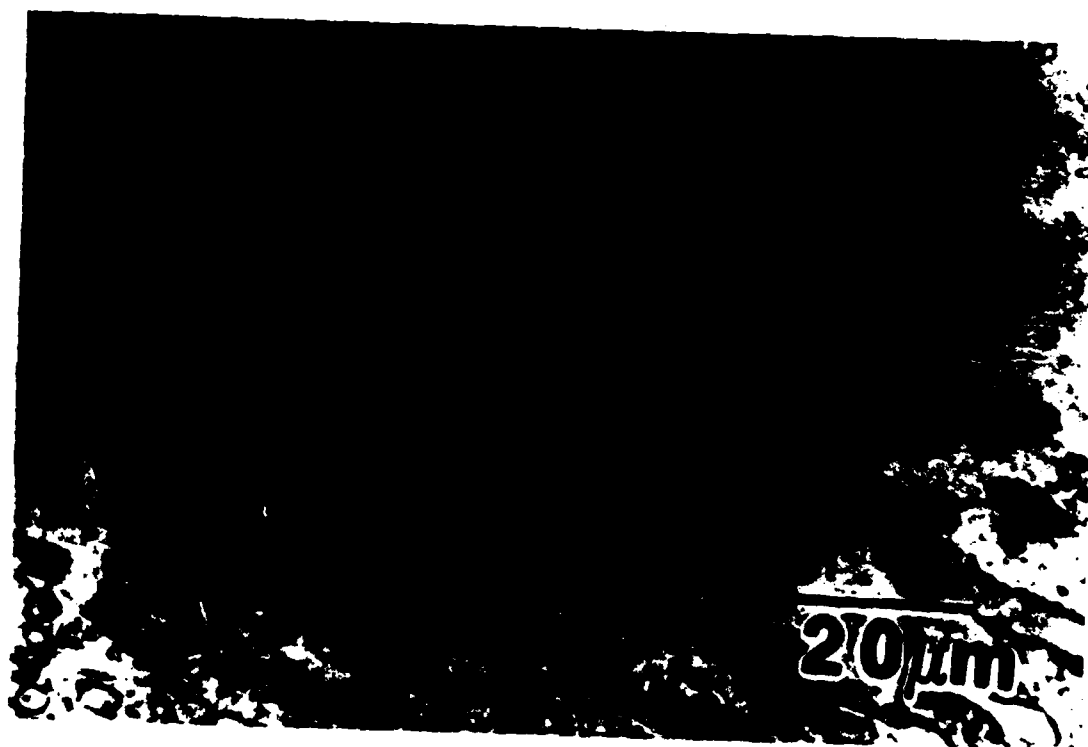


Fig. 10 Optical micrograph of a transverse section of a laser surface melted Al-8.0at.%Ni from a region which was not completely melted.



Fig. 11 TEM micrograph of an unmelted Al₃Ni intermetallic particle surrounded by the microeutectic mixture corresponding to zone A.

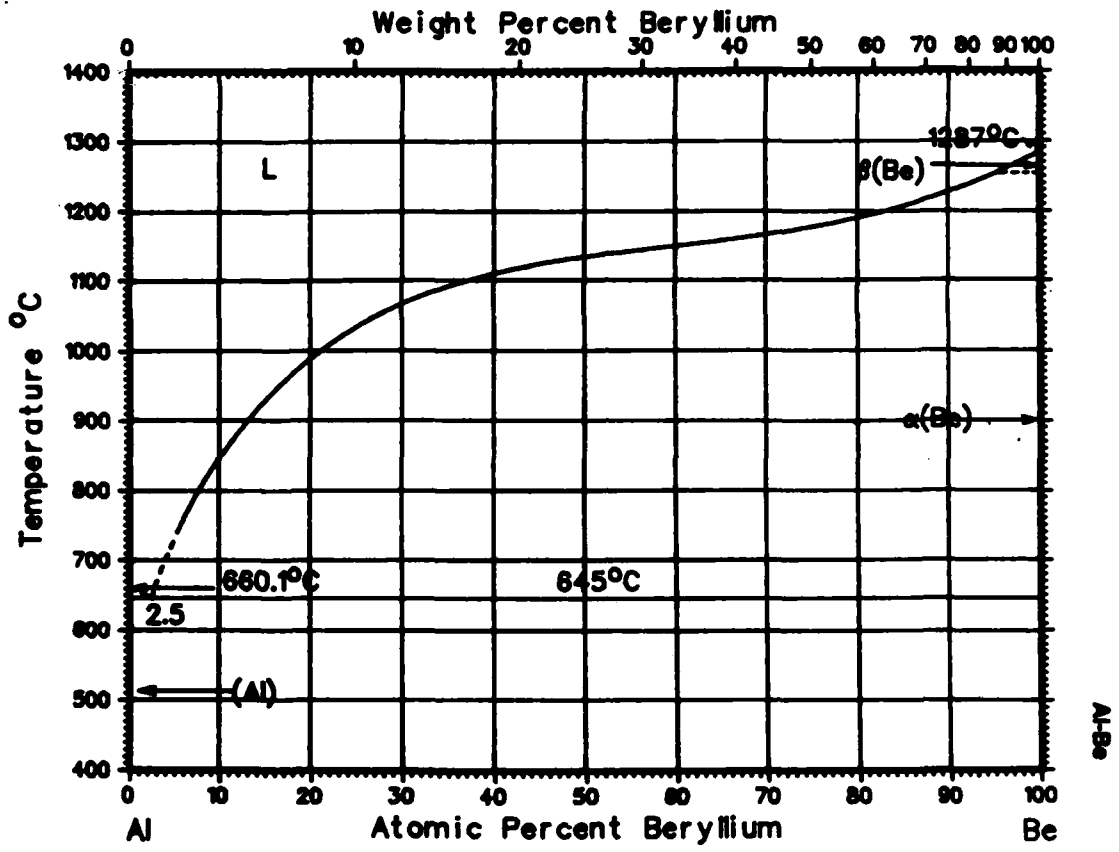


Fig. 12 Al-Be equilibrium phase diagram.

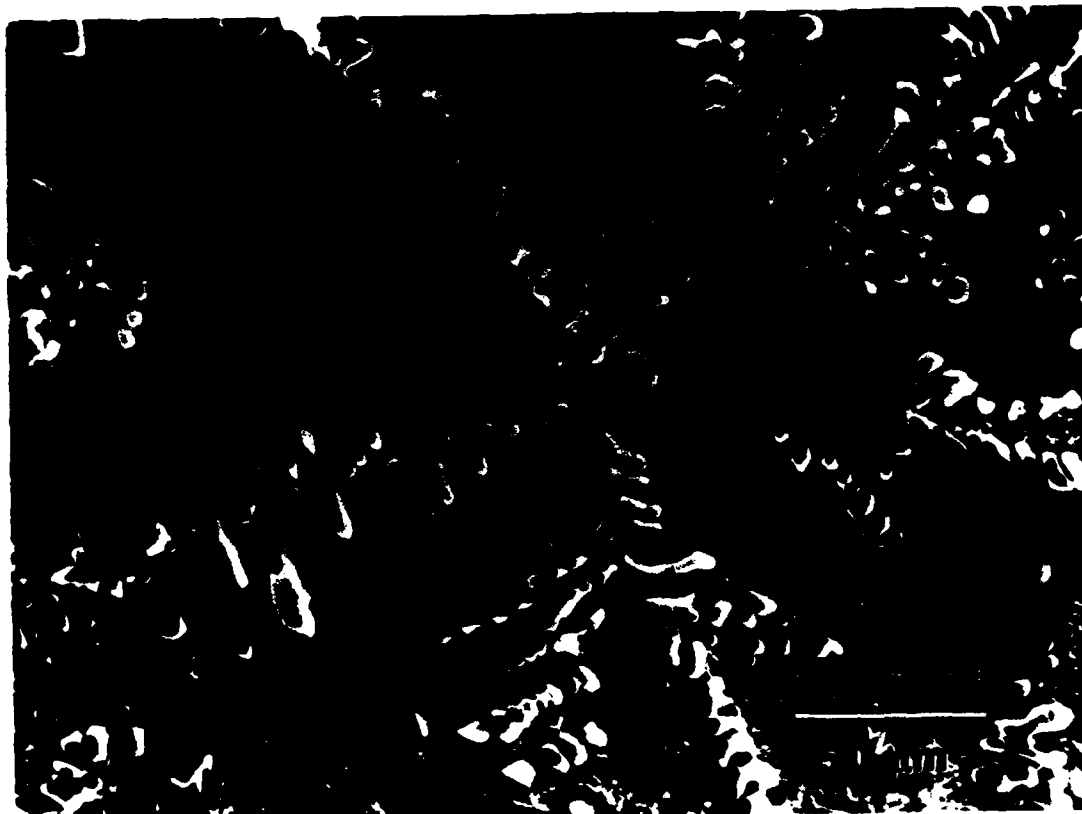


Fig. 13 Secondary electron micrograph of the cast alloy Al-20.0Be. The microstructure consists of large dendrites of Be in an eutectic mixture of Al and Be. The sample was prepared electrochemically by etching in a solution of methanol-20% nitric acid.

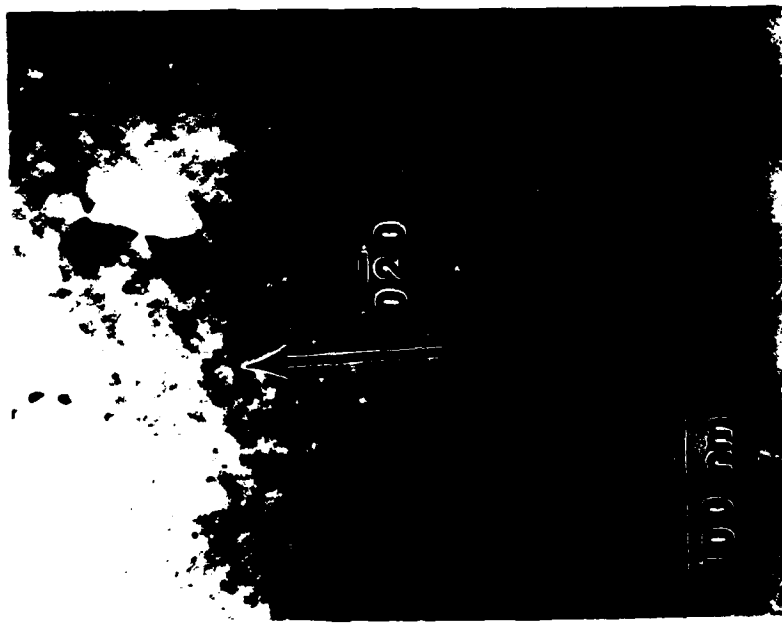
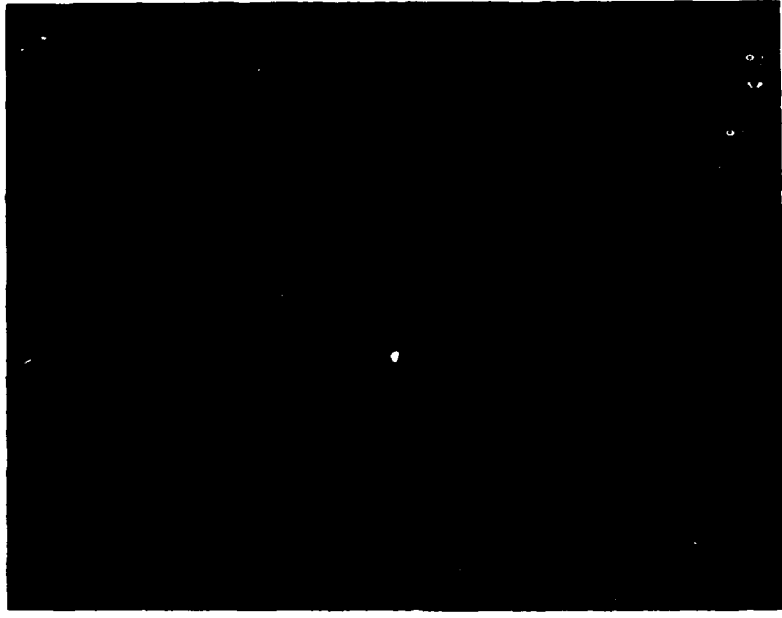
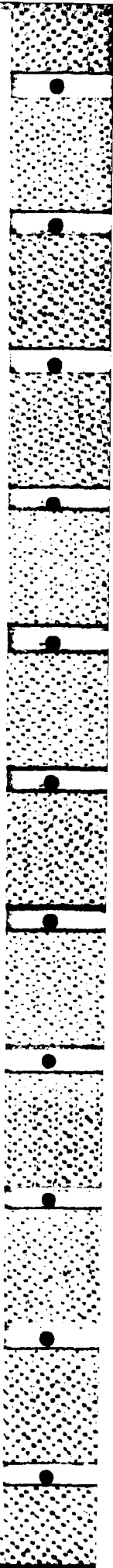


Fig. 14 (a) Bright field electron micrograph of the Al-4.48e alloy which was solution treated and aged, see text. (b) Corresponding weak beam dark field (g/3g) image. The small particles observed were precipitated during the aging treatment and are believed to be Be.



Fig. 15 Bright field electron micrograph of the melt-spun Al-4.4Be alloy. The area observed is near the wheel side. The microstructure consists of primary Al cells with an intercellular precipitate.



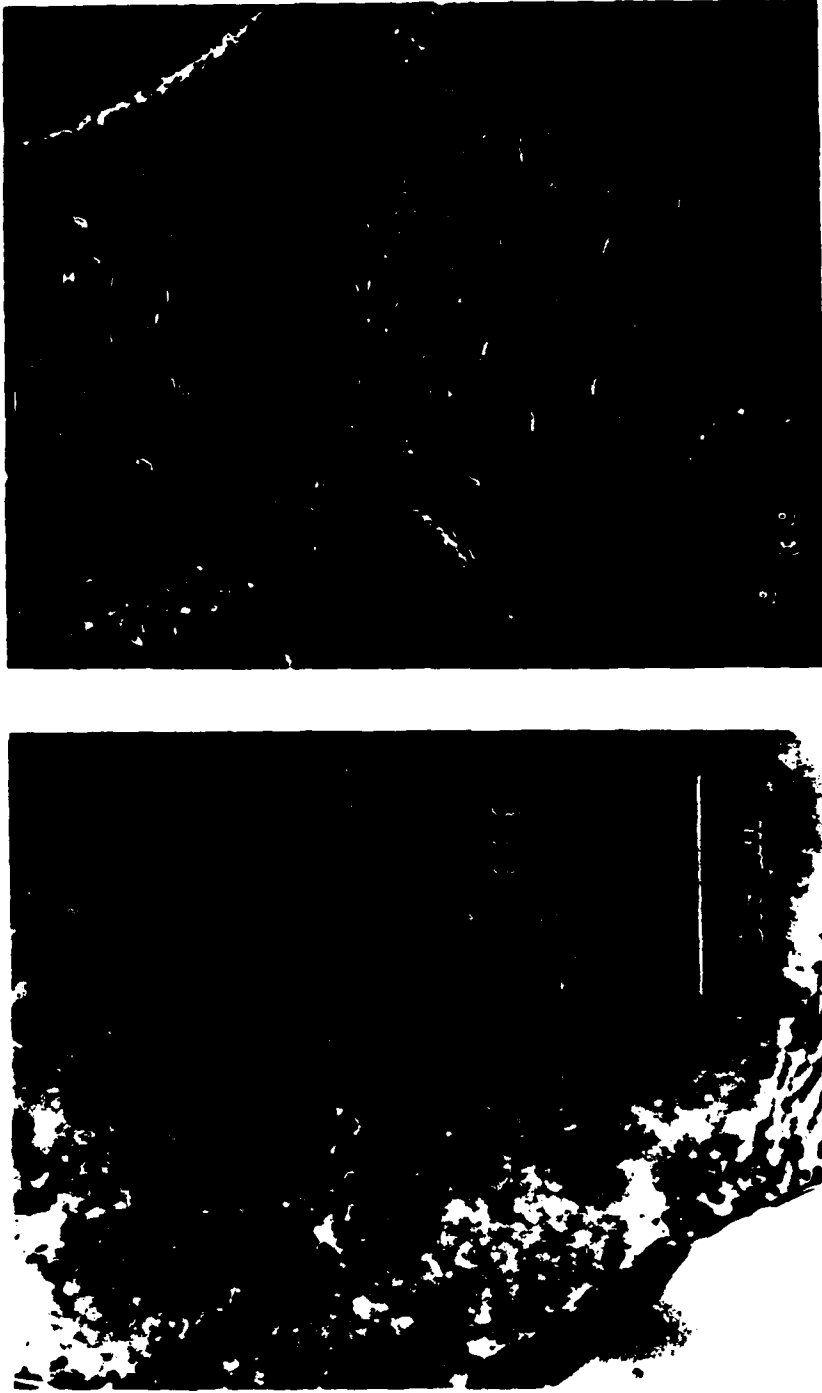


Fig. 16 (a) Bright field electron micrograph of the melt-spun Al-4.4 Be alloy. The grain observed consists of three subcells with intercellular precipitates. (b) Corresponding weak beam dark field (g/3g) image. Two types of defects, faulted and perfect dislocation loops, are observed in the intracellular regions.

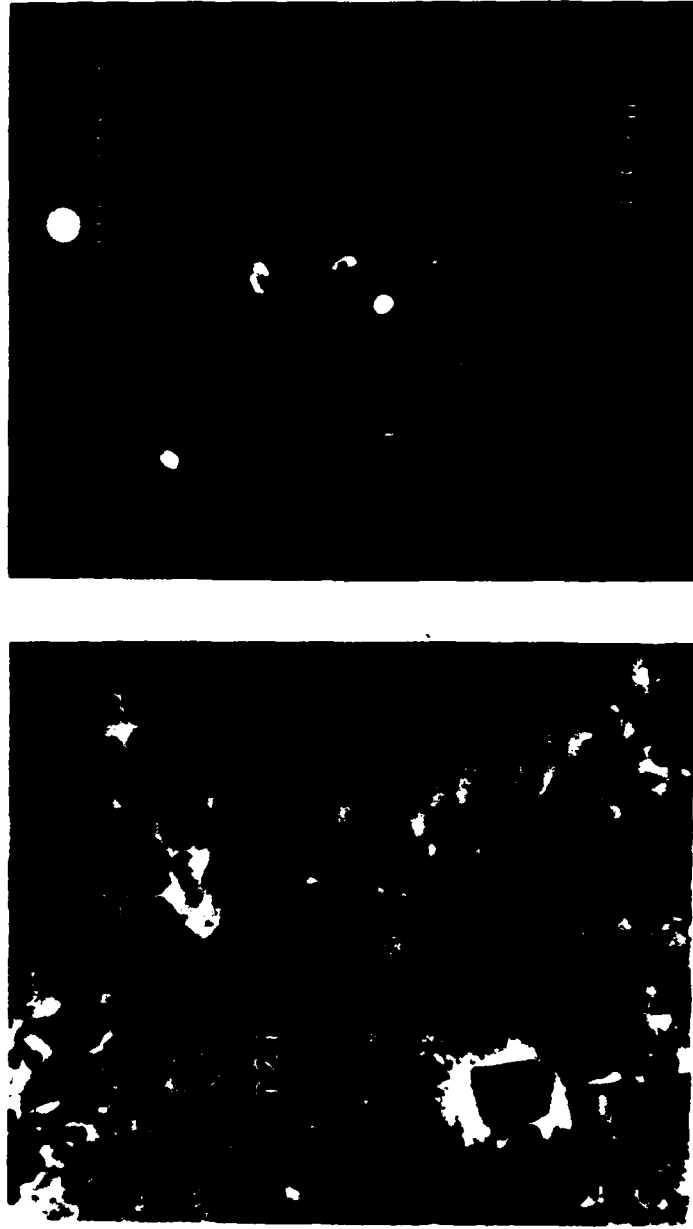


Fig. 17 (a) Bright field electron micrograph of an intercellular boundary in the Al-4.4Be alloys. (b) Corresponding dark field image using a 1210Be reflection, as shown.

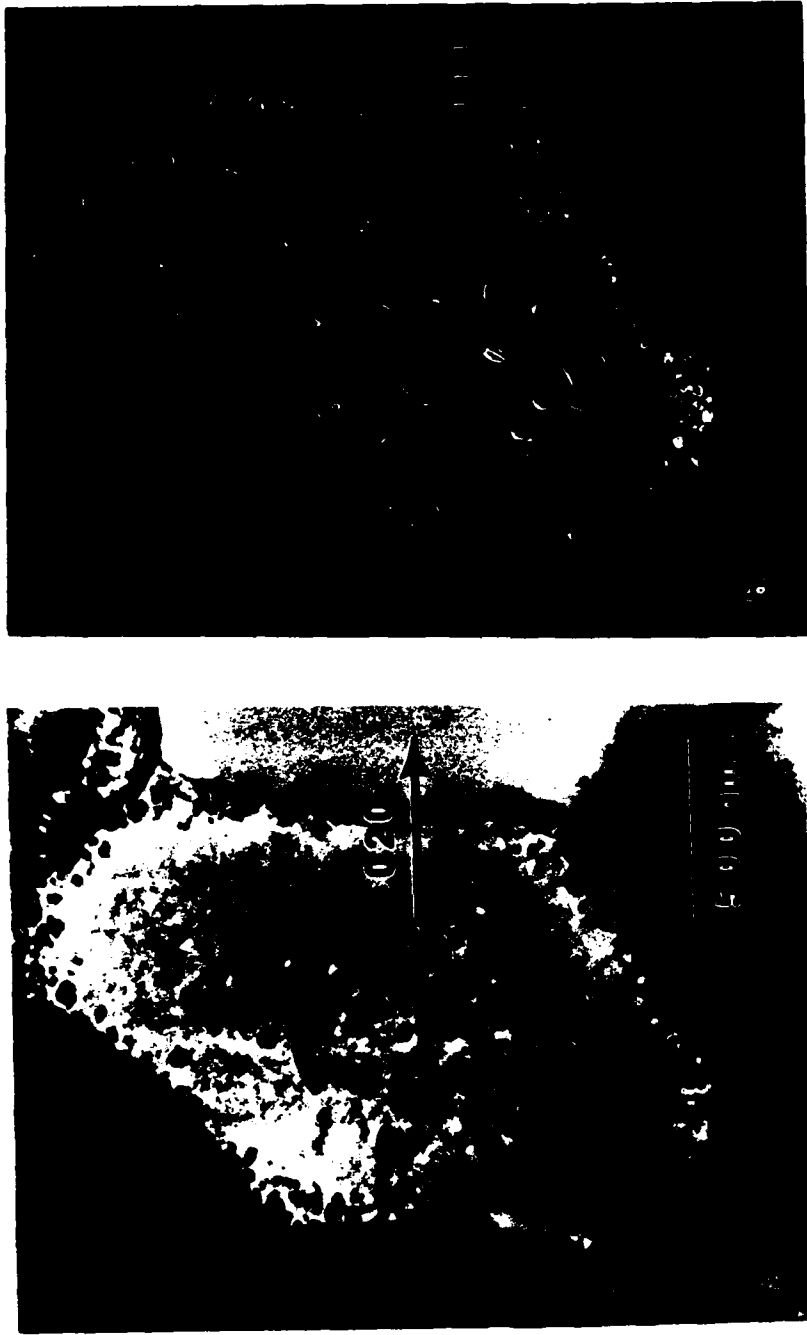
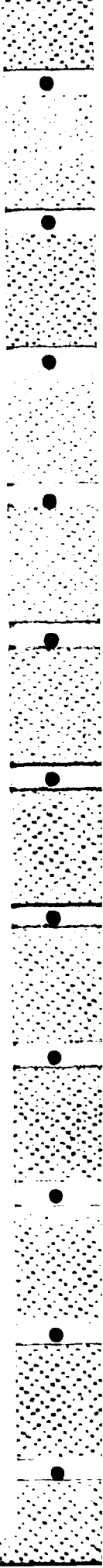


Fig. 18 (a) Bright field electron micrograph of area containing intracellular fringed defects. Electron beam direction (B) parallel to [103]. (b) WBDF image ($g/3g$, $B = [101]$) showing that defects marked A-D lie on(111). (c) and (d) WBDF images ($g/3g$, $B = [103]$) showing the effect of reversing the sign of the diffraction vector ($g = \pm 020$). The defects show outside contrast for $g = 020$, and are therefore vacancy in nature.



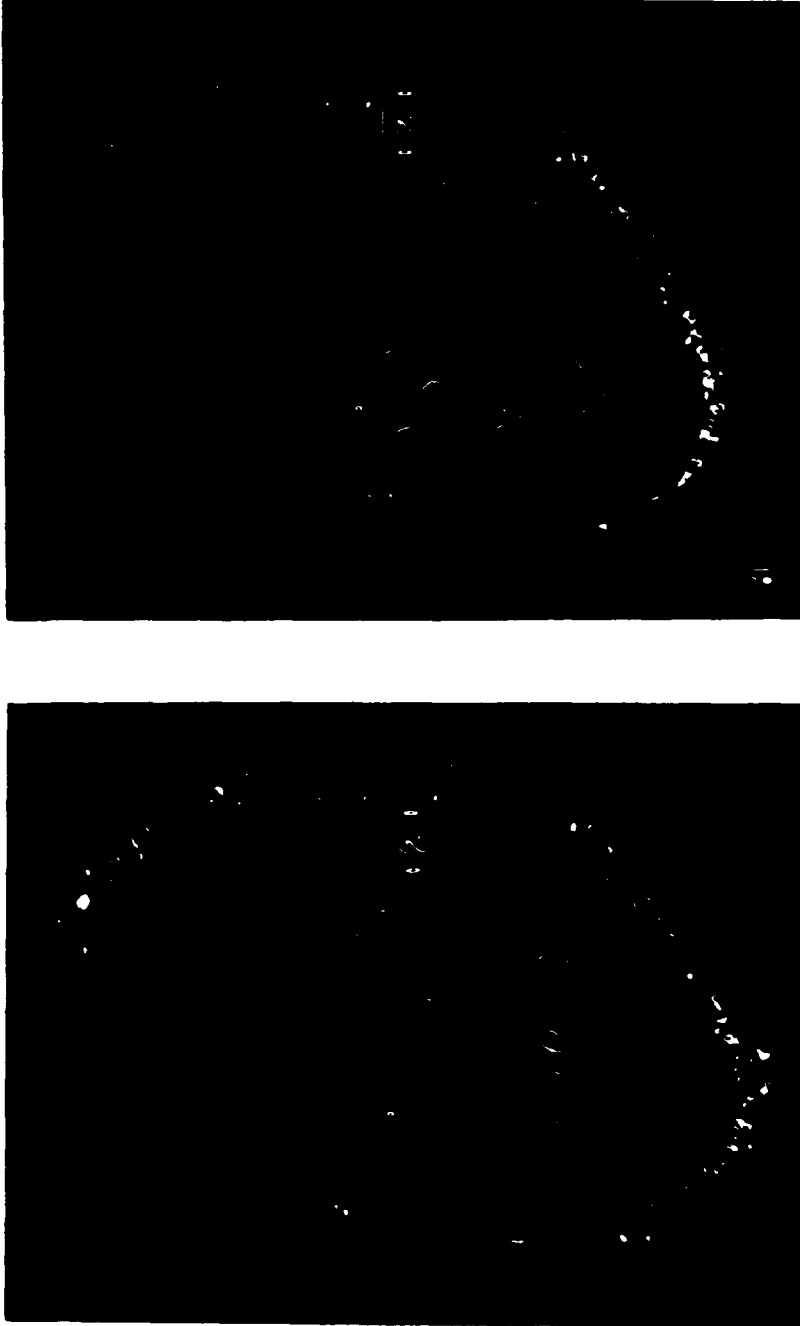
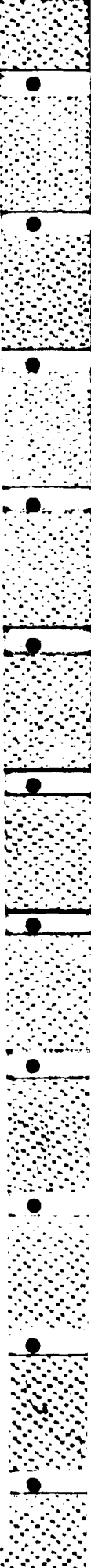


Fig. 18 (a) Bright field electron micrograph of area containing intracellular fringed defects. Electron beam direction \underline{B} parallel to $[103]$. (b) WBDF image ($\underline{g}/3\bar{g}$, $\underline{B} = [101]$) showing that defects marked A-D lie on $(11\bar{1})$. (c) and (d) WBDF images ($\underline{g}/3\bar{g}$, $\underline{B} = [103]$) showing the effect of reversing the sign of the diffraction vector ($\underline{g} = \pm 020$). The defects show outside contrast for $\underline{g} = 020$, and are therefore vacancy in nature.



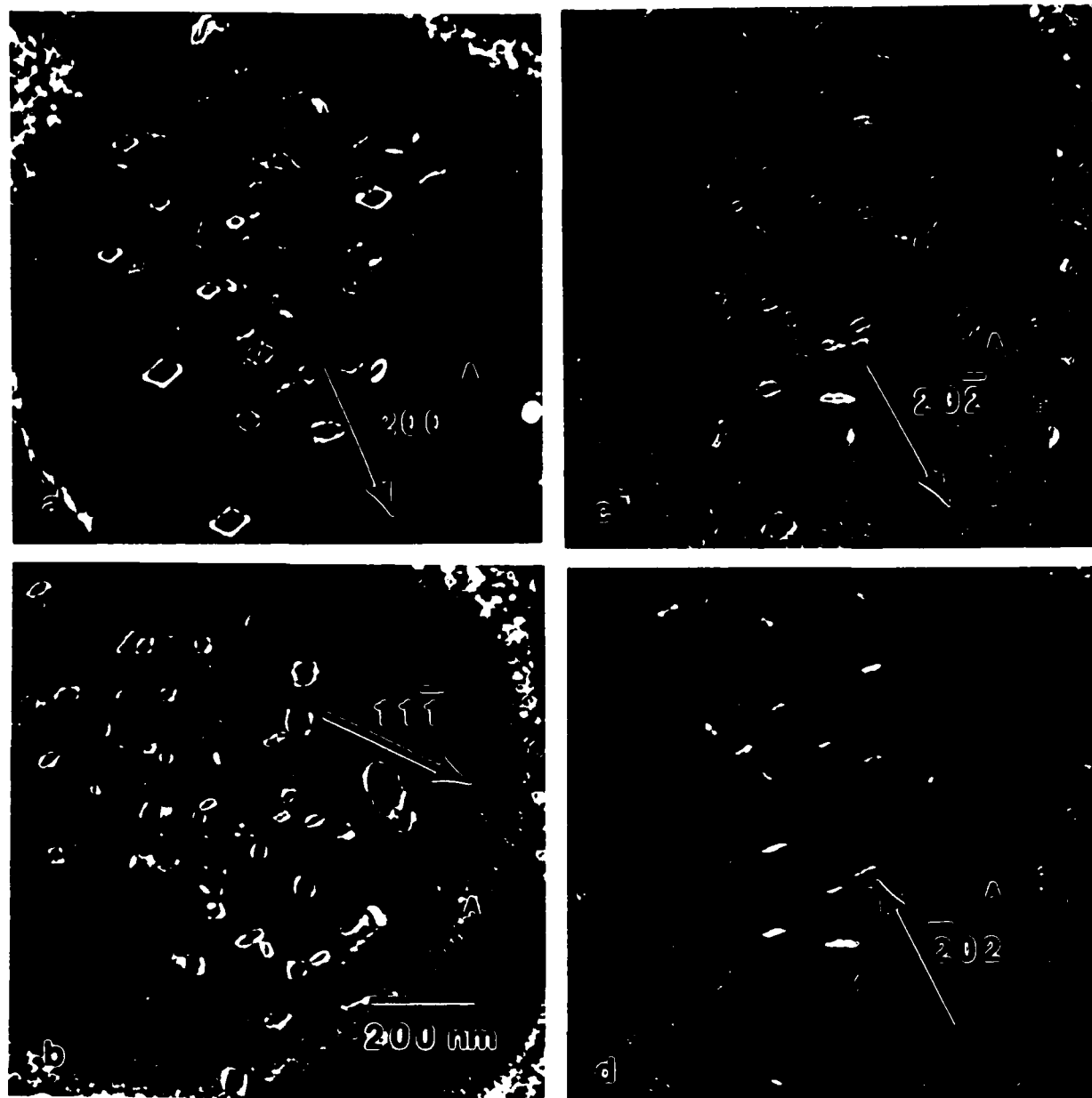


Fig. 19 Analysis of the perfect defects. (a) and (b) are WBDF images ($g/3g$, $B = [001]$ and $g/3g$, $B = [101]$) which show that the defect marked A (visible in c and d) is out of contrast for the reflecting vectors indicated; therefore $\underline{b} = \pm a/2 [011]$. (c) and (d) are WBDF images ($g/2g$, $B = [111]$) showing the effect of reversing the sign of g . The defect marked A exhibits outside contrast for $g = 20\bar{2}$, so that $\underline{b} = a/2 [0\bar{1}\bar{1}]$. The defect is then vacancy in nature.



Fig. 20 Weak beam dark field electron micrograph of the Al-4.4Be ribbon which was heat treated for 30 min. at 300°C. Direct comparison with figure 14b suggests that extended solutions of Be may be obtained by rapid solidification.

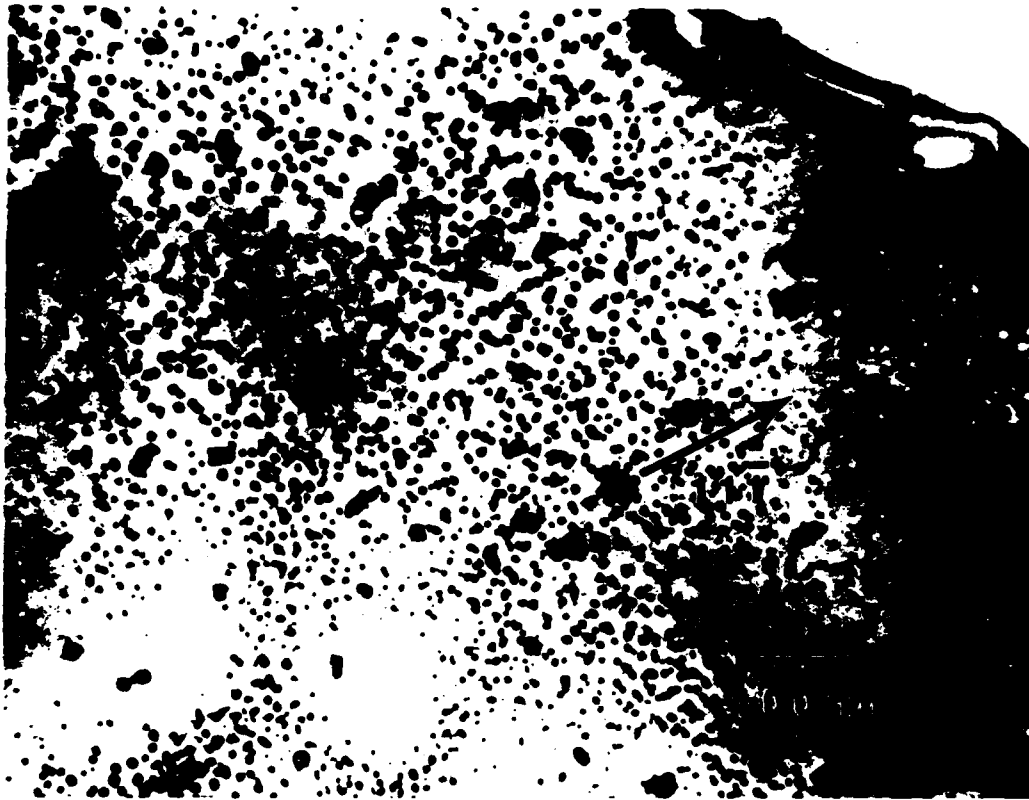


Fig. 21 Bright field electron micrograph of the melt-spun Al-5.8Be ribbon.

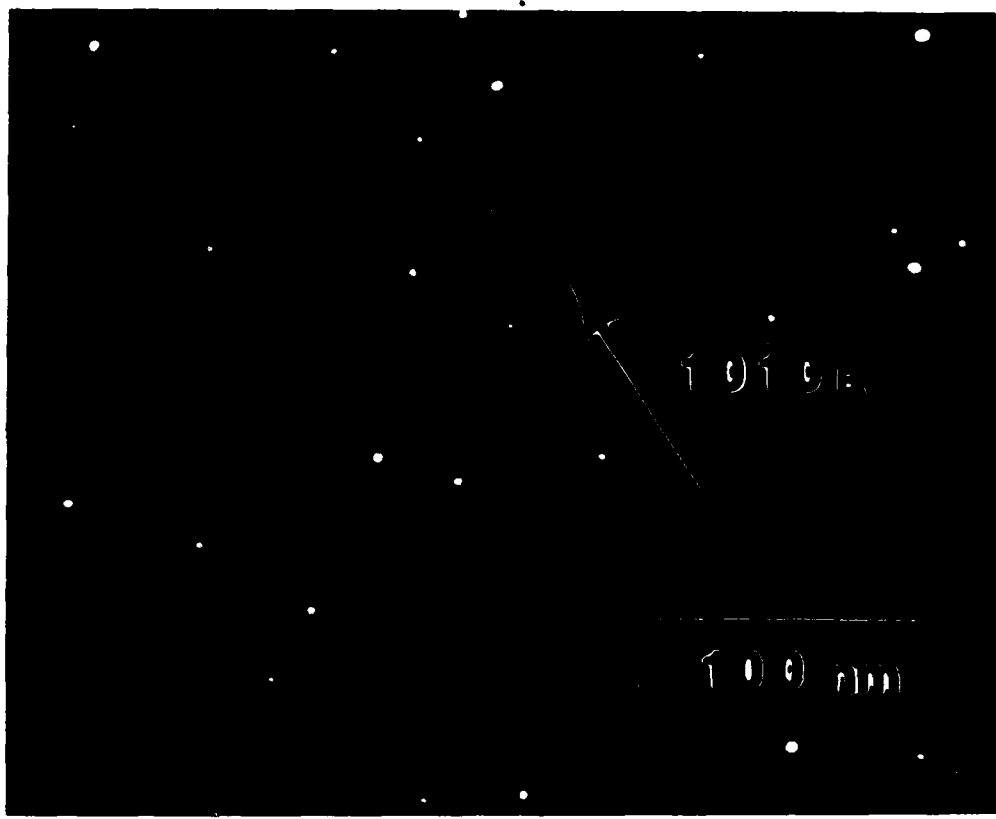


Fig. 22 Dark field electron micrograph ($g = 10\bar{1}0Be$) of the melt-spun Al-5.8Be ribbon.

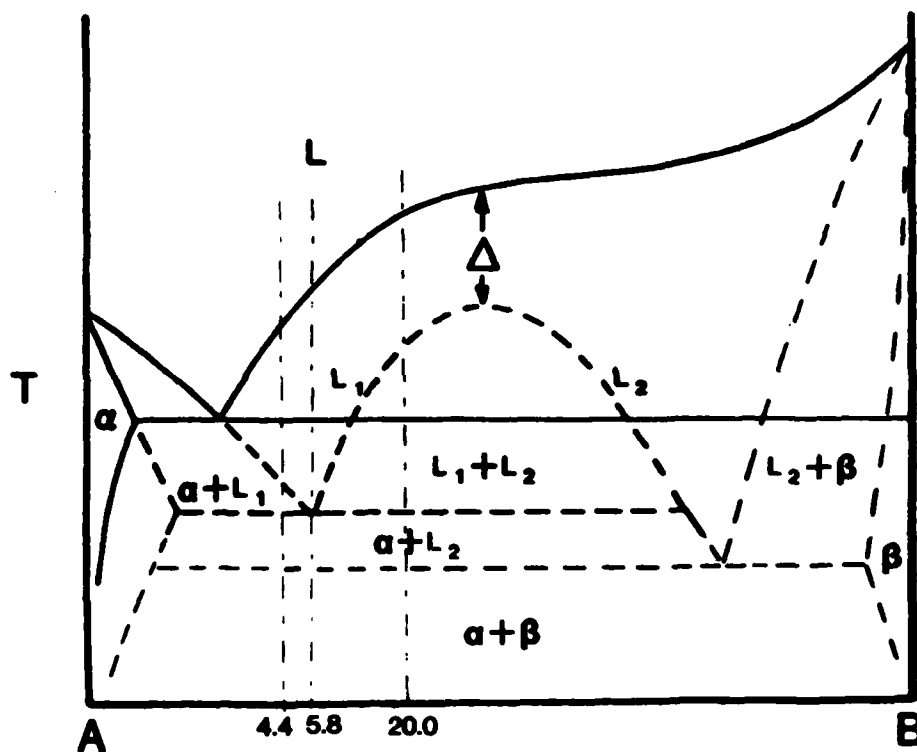


Fig. 23 Schematic phase diagram showing the presence of a submerged metastable liquid miscibility gap and the resultant monotectic reaction.

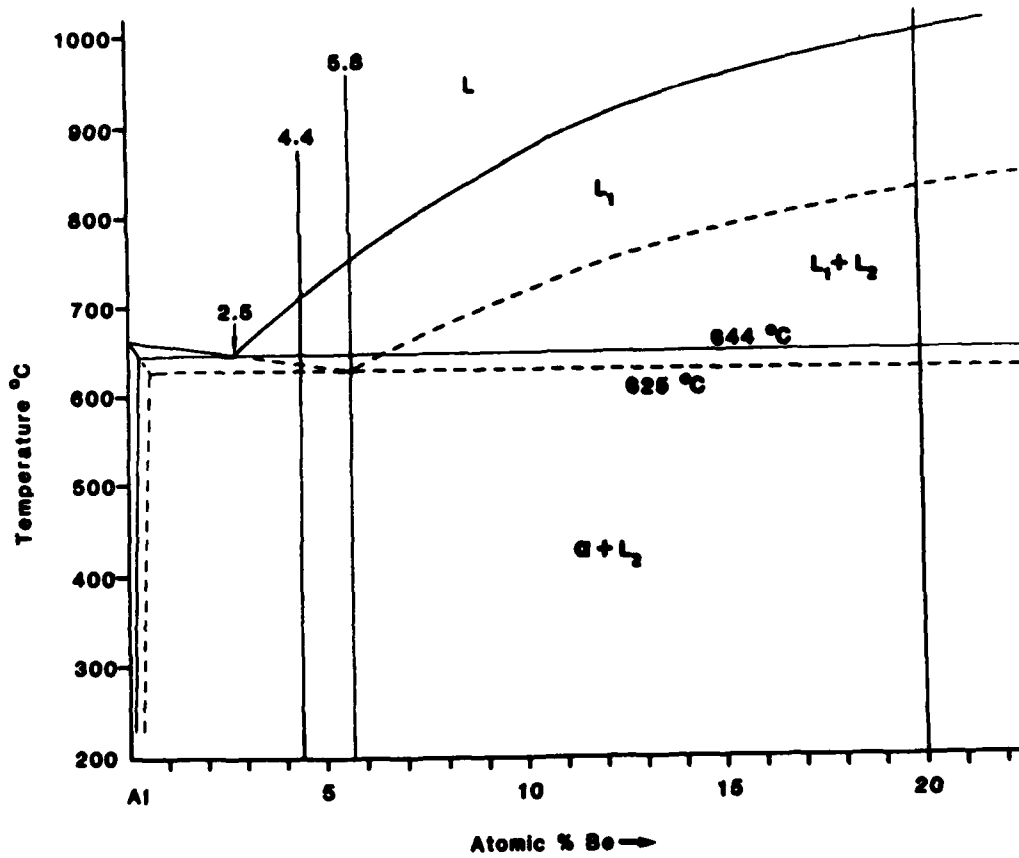


Fig. 24 The Al rich side of the Al-Be diagram with the suggested metastable monotectic reaction represented by the dashed lines.

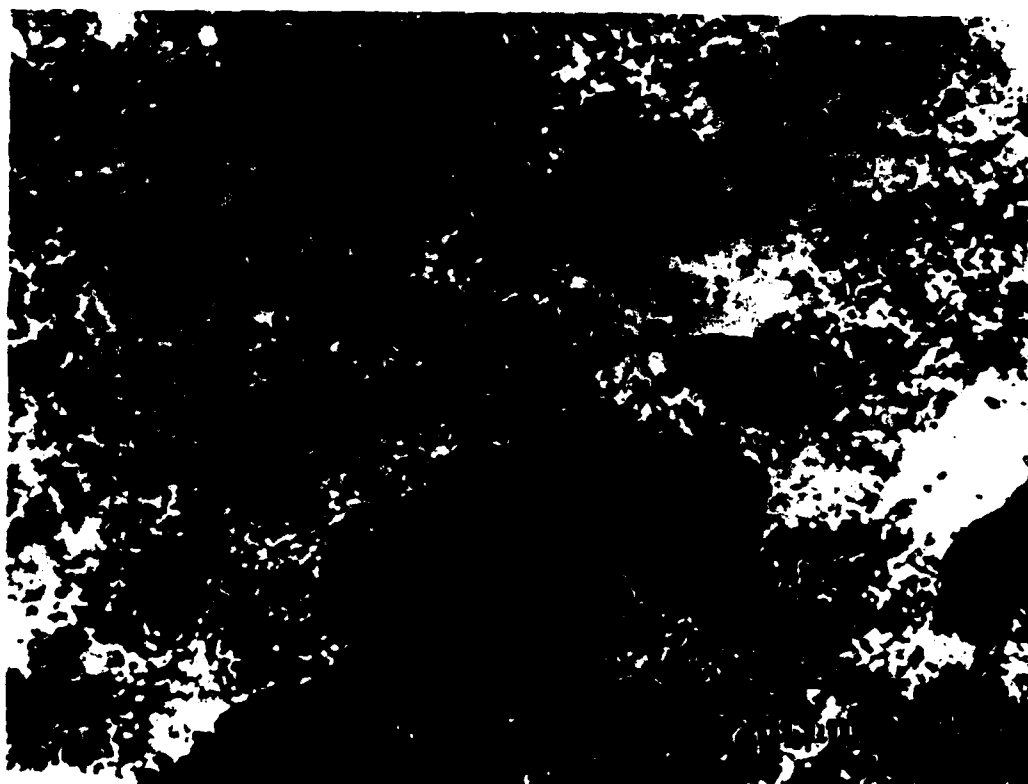


Fig. 25 Bright field electron micrograph of the melt-spun Al-20.0Be ribbon produced at the slower heat extraction rate.

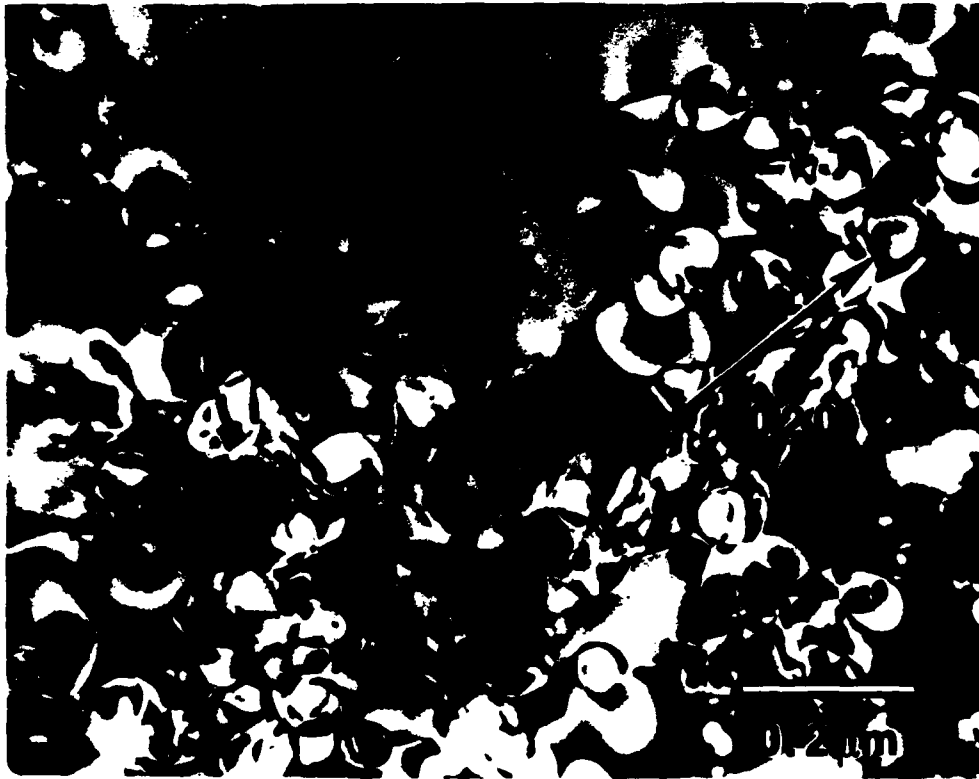
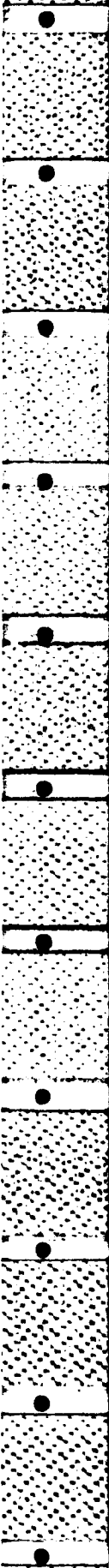


Fig. 26 (a and b) Bright field electron micrographs of the Al-20.08e alloy shown in Fig. 25. The large irregular shaped particles represent the prior promonotectic L₂ liquid. The finer precipitates are produced during the monotectic reaction.



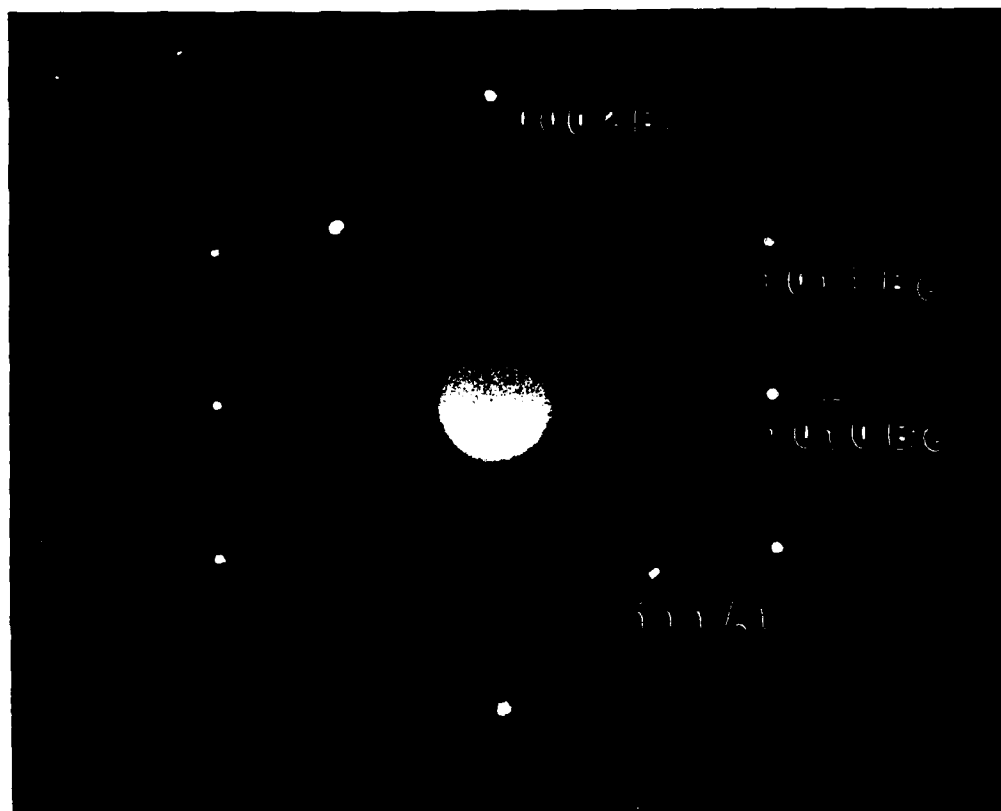


Fig. 27 A selected area diffraction pattern with the electron beam parallel to the $[1\bar{2}10]$ direction in the promonotectic L_2 . The pattern may be uniquely indexed on the basis of Be, as shown.

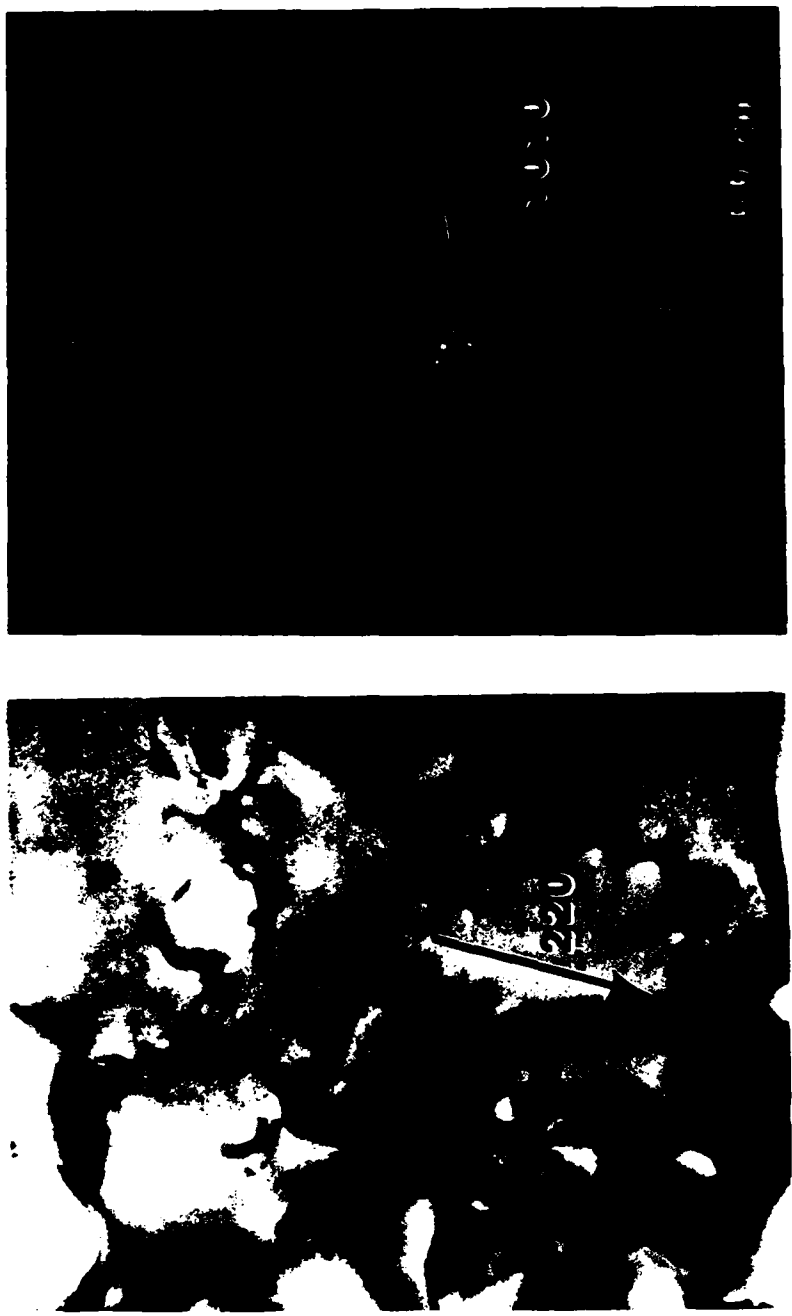
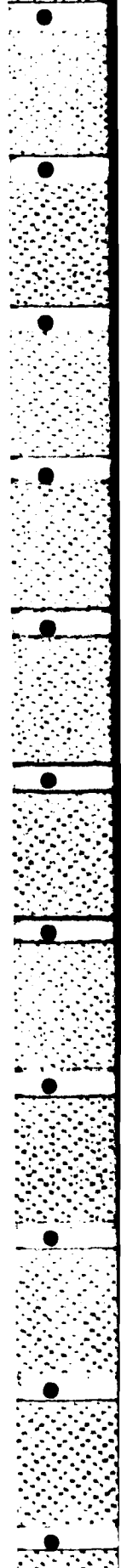


Fig. 28 (a) Bright field electron micrograph of a promonotectic Be particle.
(b) Corresponding dark field image ($g = 10\bar{1}0$ Be) showing the presence of a second reaction product within the Be particle.



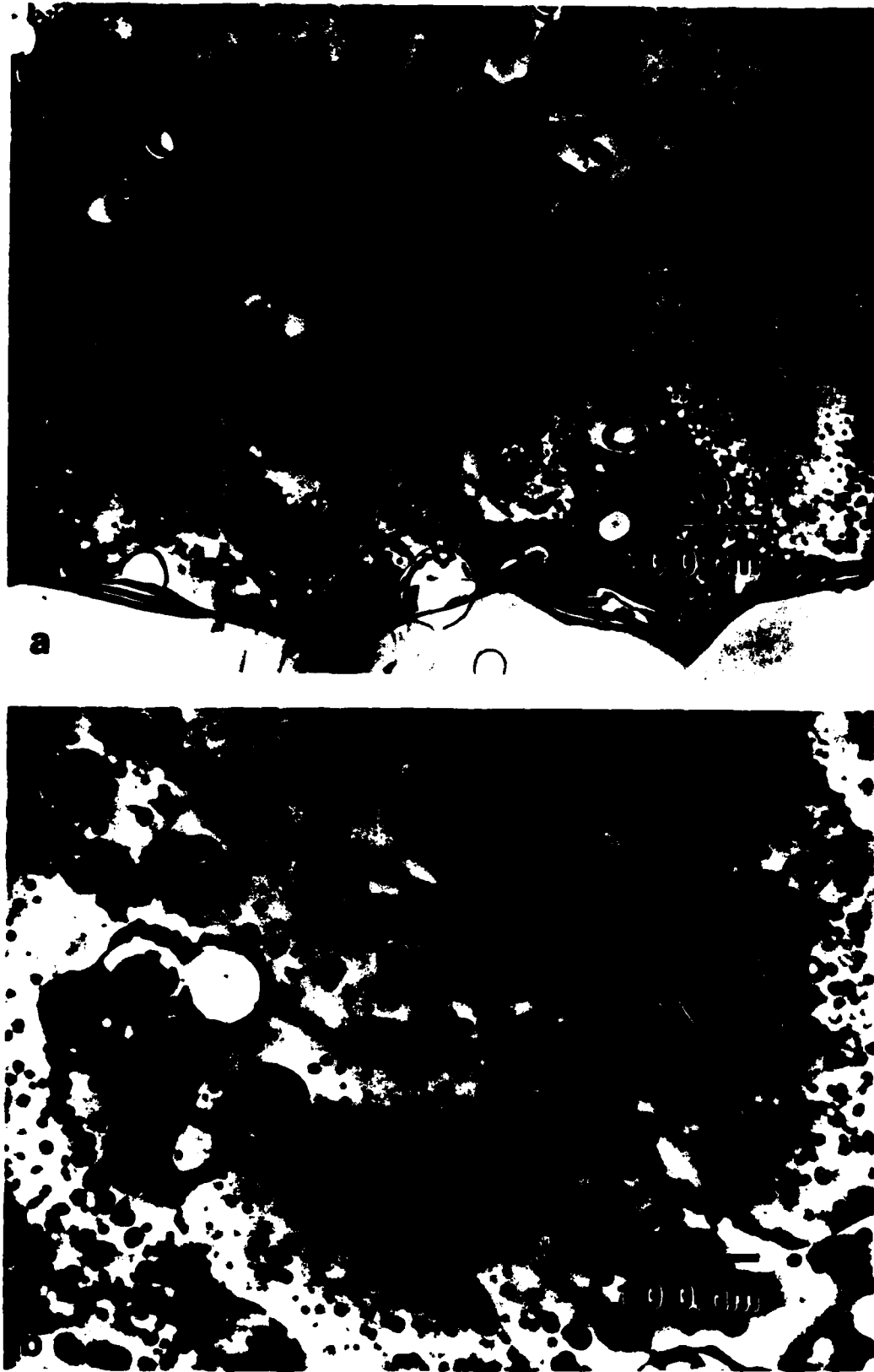


Fig. 29 (a and b) Bright field electron micrographs showing the melt-spun Al-20.0Be alloy produced at the higher heat extraction rate.



Fig. 30 Bright field electron micrograph showing the coalescence of the pro-monotectic L_2 phase in the Al_{20.0}Be alloy produced at the slower heat extraction rate.

3. PROCESSING OF ZONE A MICROSTRUCTURES

As pointed out in the introduction, it was shown during the first year's work that the optimum strengthening effect in rapidly solidified alloys based on Al-8Fe* is associated with the presence of a zone A microstructure which possesses an extremely refined precipitation of a metastable intermetallic compound at the intercellular regions. So that bulk pieces may be produced with optimized mechanical properties, it is necessary to develop methods for the fabrication of particulate whose entire microstructure may be described as zone A. In this section, results of experiments aimed at the production of particulate exhibiting such morphologies are described and discussed.

3.1 Rapidly Solidified Powders

The microstructures of rapidly solidified powders of Al-8Fe and Al-8Fe-2Mo which were produced by centrifugal atomization locally and at Pratt and Whitney (Government Products Division), respectively, are shown in Fig. 31. It is clear from these optical micrographs that both types of powder exhibit zone A and zone B morphologies. In fact, this is a common observation in rapidly solidified powders of various composition made in a variety of ways. These observations can be explained on the basis of the model, described above, for the formation of the two types of morphology. Thus, it is expected that for a liquid droplet being convectively cooled by He gas, such as in the RSR process, a fairly high degree of undercooling will be achieved prior to nucleation. In this way, a zone A microstructure may form. However, as the nuclei grow, latent heat of fusion will be liberated. For droplets with diameters $> 2-3 \mu\text{m}$, the rate of heat extraction, governed by the heat transfer coefficient, is not sufficiently rapid to prevent recalescence from occurring.

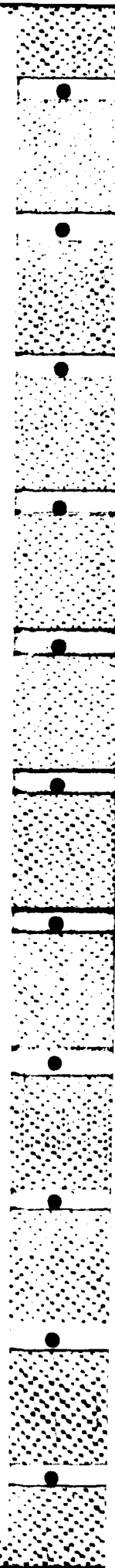
*In this section, all compositions are in weight %, unless otherwise stated.

As the temperature of the powder increases above the extended liquidus where nucleation and growth of primary α -Al becomes energetically unfavorable, zone morphologies will form. For this reason, it is felt that when using powder fabrication techniques which result in mean particle diameters in the range 50-200 μm , it is unlikely that a significant yield of powders possessing zone A microstructures will be obtained.

3.2 Melt-Spun Ribbons

It has been found that, under certain conditions, melt-spinning of hyper-eutectic Al alloys results in the formation of ribbons possessing microstructures which consist entirely of zone A. These conditions are as follows. The melt-spinning chamber is evacuated to $\approx 10^{-5}$ torr before filling to ≈ 1 atm. of He. The melt is placed in a graphite crucible which is also evacuated before Ar gas is admitted into the crucible. Once a superheat of ≈ 50 - 100°C is established, the pressure of the Ar gas is increased to force the liquid stream onto the Cu wheel which is rotating at a surface speed of $\approx 35 \text{ ms}^{-1}$. An optical micrograph of the polished and etched cross-section of a ribbon of Al-8Fe-2Mo processed in this manner is shown in Fig. 32a. As can be seen, the microstructure exhibits featureless contrast, typical of zone A. In way of confirmation of this, a transmission electron micrograph of this structure is shown in Fig. 32b and this is again typical of zone A for this alloy.

It is of interest to compare the microstructures of ribbons produced by melt-spinning into He, as described above, and those produced by spinning into an evacuated chamber. Scanning electron micrographs of both types of ribbon are shown in Fig. 33 (a,b,c,d). As can be seen, the surfaces in contact with the Cu wheel for the two types of ribbon are fairly similar in appearance, whereas those exposed to He (Fig. 33a) and vacuum (Fig. 33c) are somewhat



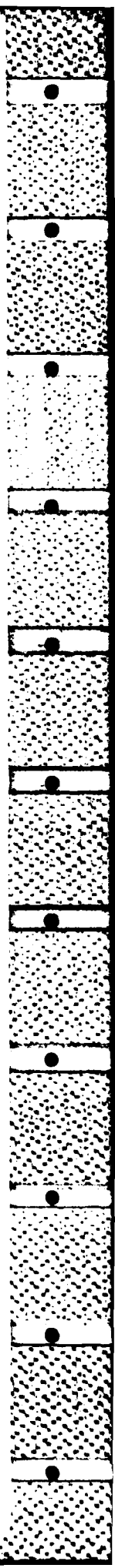
different. Thus, in the case of He, the surface is rather smooth while for the vacuum spun ribbon the surface has a rougher appearance. The similarity in the appearance of the ribbon surface in contact with the wheel implies that the presence of the He gas had little or no effect on the wetting of the substrate by the molten stream. Thus, the initial rate of heat extraction in the two cases (He and vacuum) is expected to be approximately equal. However, the presence of the He has a marked effect on the topography of the surface of ribbons not in contact with the quenching substrate, such that the observations are consistent with a more rapid and uniform solidification rate.

When the microstructures of the different ribbons are examined using TEM, three types of morphology are observed. For both types of ribbon (He and vacuum cast), the microstructures of material found near to the surface in contact with the quenching substrate are found to be rather similar. Comparisons are given in Fig. 34(a-f), including selected area diffraction patterns. In the case of He cast ribbons, Fig. 34(a), an extremely refined cellular structure is observed, and in some instances there is a small amount of intergranular precipitation of Al_6Fe (Fig. 34b). Similar types of microstructures are produced in vacuum cast ribbons, Fig. 34(d,e) although not on such a refined scale, as can be seen in the micrographs and by comparing the diffraction patterns (Fig. 34(c,f)). The similarity between these microstructures may be understood in terms of the more or less equally rapid rate of heat extraction experienced by both types of ribbon during the initial period of solidification whereas the less refined scale observed in the vacuum cast ribbon may be attributed to a small but significant amount of heating resulting from recalescence during the subsequent solidification process.

In the He cast ribbon, most of the material has a microstructure similar to that shown in Fig. 35a. This consists of a cellular microstructure based on α -Al with a refined distribution of a metastable intermetallic compound. A

SAD pattern recorded from this microstructure is shown in Fig. 35b. This microstructure was described in the first annual report and originally by Jones⁽¹⁾ and may be designated as zone A. In contrast to this, no such microstructures were observed for the case of the vacuum cast ribbon. In fact, much of this latter ribbon exhibited a morphology similar to that given in Fig. 36. This microstructure is much coarser than those shown above and consists of relatively large particles. A diffraction pattern taken from one of the larger particles is shown in Fig. 37, and this may be indexed on the basis of Al_6Fe ; the majority of the large particles are in fact found to be Al_6Fe . In addition to these particles, there are a smaller number of precipitates, such as at A in Fig. 36a, whose identity has not been determined at the present time. This coarse morphology (Fig. 36) is consistent with solidification occurring at a temperature above the extended α -Al liquidus, i.e. zone B, the temperature rise being attributed to the effects of recalescence.

The main reason for the difference between the microstructures of the two types of ribbon appears to involve the role of He in inhibiting the extent of recalescence during solidification. Thus, in both cases, the microstructures which form first are influenced by the extremely rapid rate of heat extraction which results when the liquid melt comes into contact with the wheel. As solidification continues, latent heat of fusion is liberated; some of this heat will be conducted away through the substrate, while some will tend to cause the temperatures of both the solid already formed and the remaining liquid to increase, i.e. recalesce. Thus, in the absence of any further significant means of extracting heat (i.e. for vacuum cast ribbon), the first solid to form may be heat-treated to some extent, as was observed (Fig. 34(d,e), and the temperature of the liquid may rise above that of the extended liquidus so that zone B may form (Fig. 36). In way of contrast, the somewhat



rapid rate of heat extraction associated with the presence of He as an additional quenching medium may reduce the effective temperature rise associated with recalescence. In this way, the liquid may remain undercooled below the temperature of the extended α -Al liquidus so that only zone A microstructures result, as in fact is observed (Fig. 35).

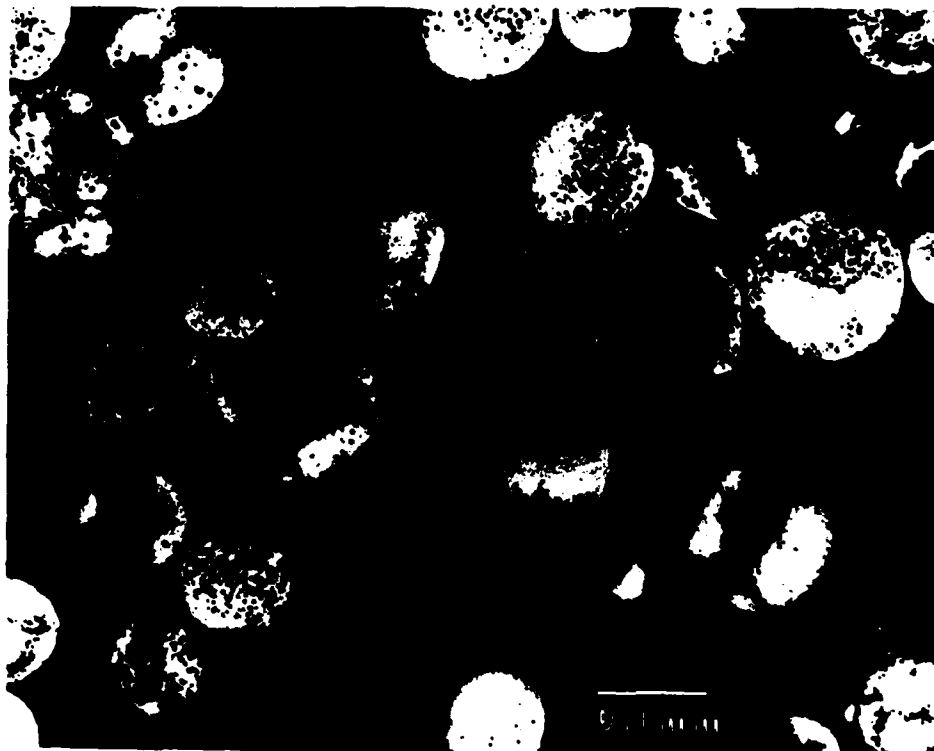
In summary, it seems that for the alloys of interest (i.e. those based on the binary Al-8Fe), melt-spinning into an atmosphere of He, providing the other processing parameters are set as described above, causes zone A microstructures to form. Since these ribbons may be extruded, either in the form of ribbons or after being reduced to particulate, at temperatures of \approx 350-375°C where the microstructures are expected to be stable, melt-spinning is evidently a very attractive process.

3.3 Laser Surface Melting

Laser surface melting has been used as a means of producing small volumes of rapidly solidified materials. It has been well established that rapid solidification will accompany surface melting when using a laser providing a deep penetration of the sample is avoided. In the present work, for almost all compositions examined, zone A microstructures were produced. An example of the zone A formed in Al-6.0Ni (at.%) and Al-8Fe-2Mo (wt.%) are shown in Figs. 3 and 38, respectively. In the most concentrated alloy studied in the Al-Ni system (8.0at.%) bands of zone B were observed in the melt-pool, as shown in Fig. 39, although again most of the rapidly solidified material exhibited a zone A morphology.

In section 2, a model for the formation of rapidly solidified microstructures was presented which involved undercooling below the extended α -Al liquidus and a rapid rate of heat extraction to inhibit recalescence. This interpretation of the microstructure of laser surface melted alloys implies

that a substantial degree of liquid undercooling can be achieved, while generally it has been considered that the temperature gradient is positive ahead of an advancing interface when regrowth occurs. Although, at first, it may appear that these two notions are inconsistent, this is in fact not the case since the undercooling that is achieved during regrowth has a kinetic origin. Thus, heat is extracted at a very rapid rate through the cold substrate (i.e. base metal) and this causes the temperature to drop at the solid/liquid interface. The interface will, of course, begin to propagate into the liquid at an increasing rate, but it is suggested that the rate of regrowth is insufficient to respond to the rate of heat extraction. In this way, a kinetic undercooling may be developed at the interface. The amount of undercooling developed will depend on the thermal conductivity of the metal involved, and since this is a significant quantity in Al alloys, the undercooling which may be achieved is thought to be large. For this reason, the microstructures of Al alloys obtained in LSM and MSR are expected to be rather similar. This has been found to be the case, as is evident when the microstructures presented in Figs. 38 and 3 for LSM of Al-8Fe-2Mo (wt.%) and Al-6.0Ni (at.%) are compared with those of the same alloys produced by MSR, shown in Figs. 35 and 40, respectively. These results are in contrast to those obtained for LSM and MSR of Ti-Si alloys. In this particular case, the thermal conductivity is relatively low and so the degree of kinetic undercooling will be necessarily limited. This is found to be the case, and the microstructures in these particular alloys obtained by LSM and MSR are not similar.

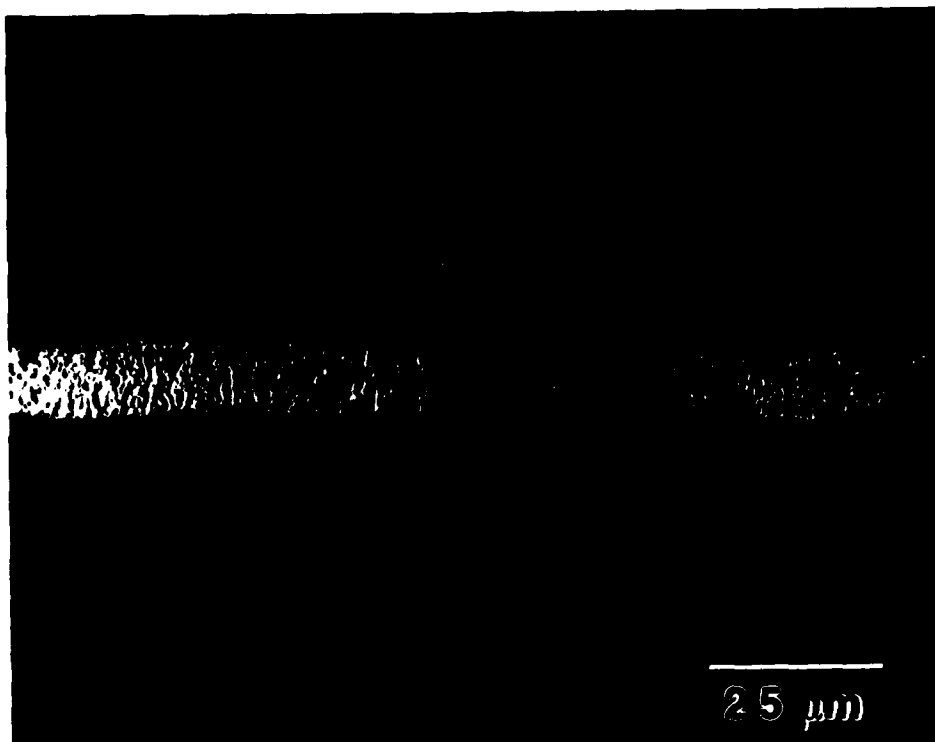


a



b

Fig. 31 Optical micrographs of centrifugally atomized powder a) Al-8Fe-2Mo made by Pratt & Whitney Aircraft's RSR process, b) Al-8Fe powder made by the University of Illinois. Both specimens etched with Keller's.



a



b

Fig. 32 Al-8Fe-2Mo ribbon made in He a) optical micrograph of a cross-section of ribbon etched with Keller's, b) transmission electron micrograph of ribbon showing the fine cell structure that is typical of zone A.

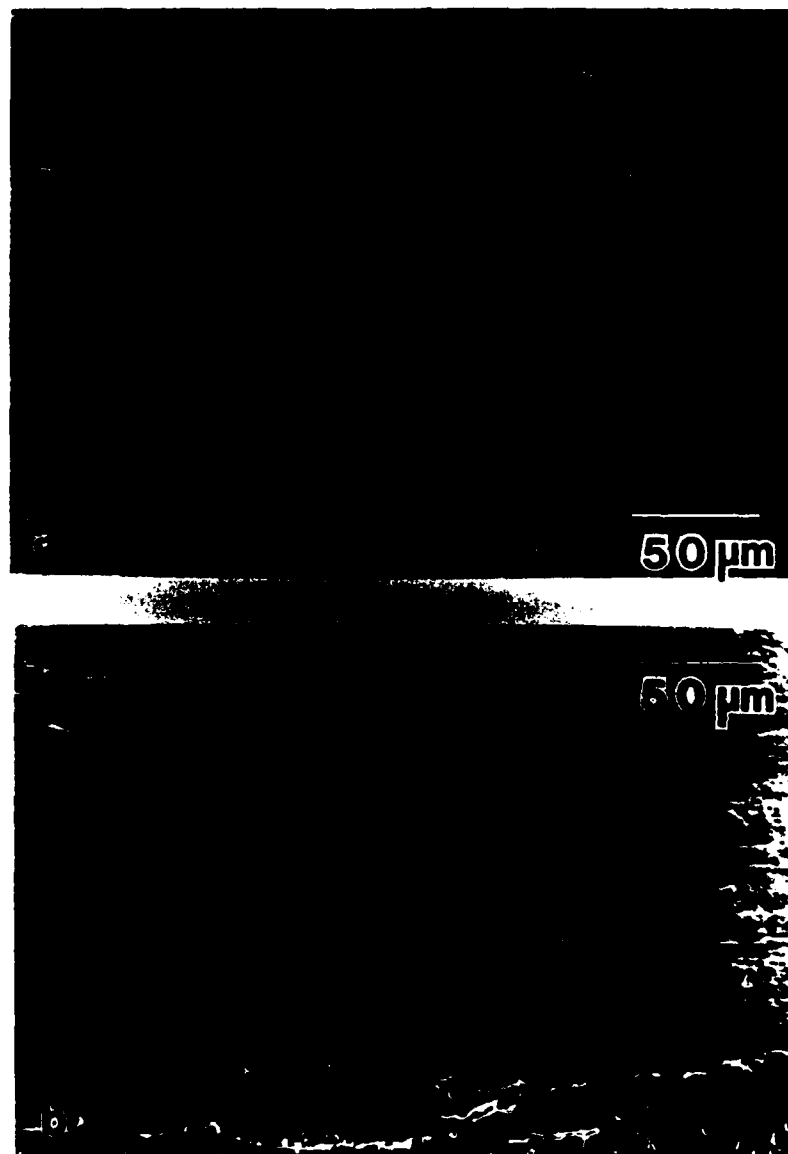


Fig. 33 Scanning electron micrographs of Al-8Fe-2Mo a,b) ribbon made in He and c,d) ribbon made in vacuum. a,c) are top surfaces and b,d) are bottom or wheel side surfaces of the particular types of ribbon.

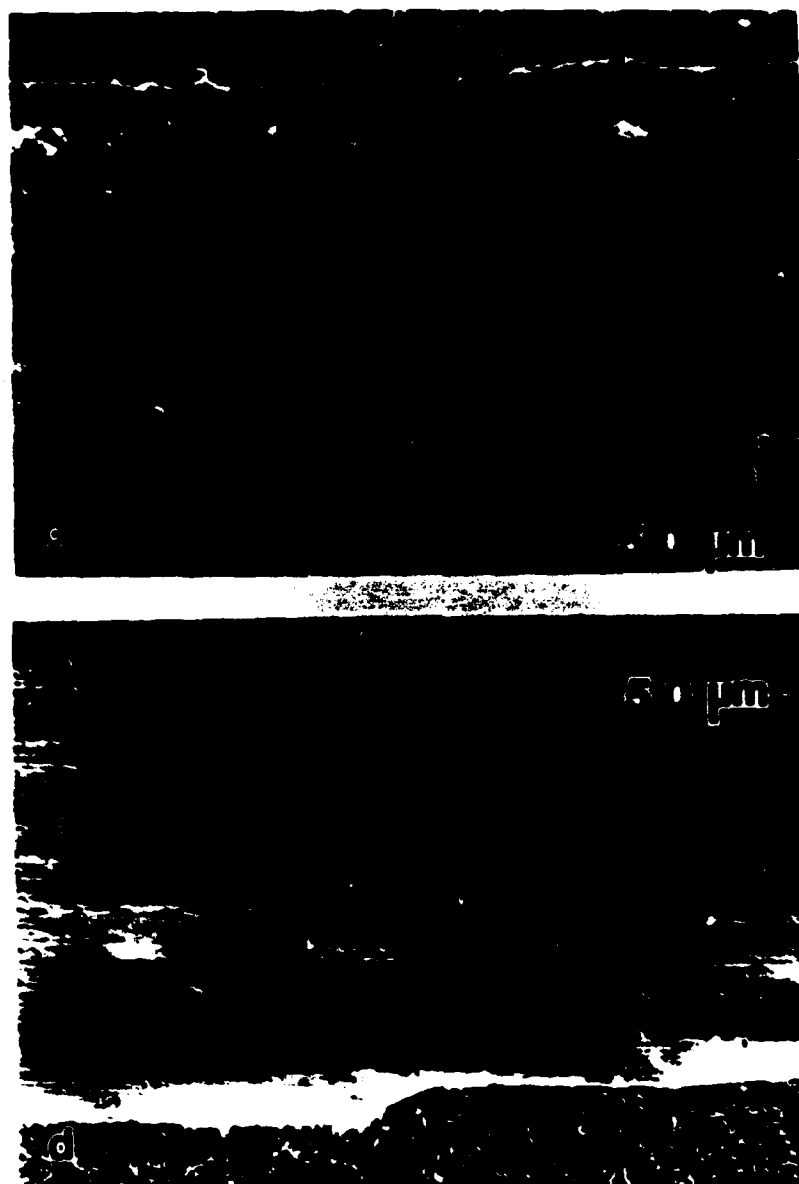


Fig. 33 Scanning electron micrographs of Al-8Fe-2Mo a,b) ribbon made in He and c,d) ribbon made in vacuum. a,c) are top surfaces and b,d) are bottom or wheel side surfaces of the particular types of ribbon.

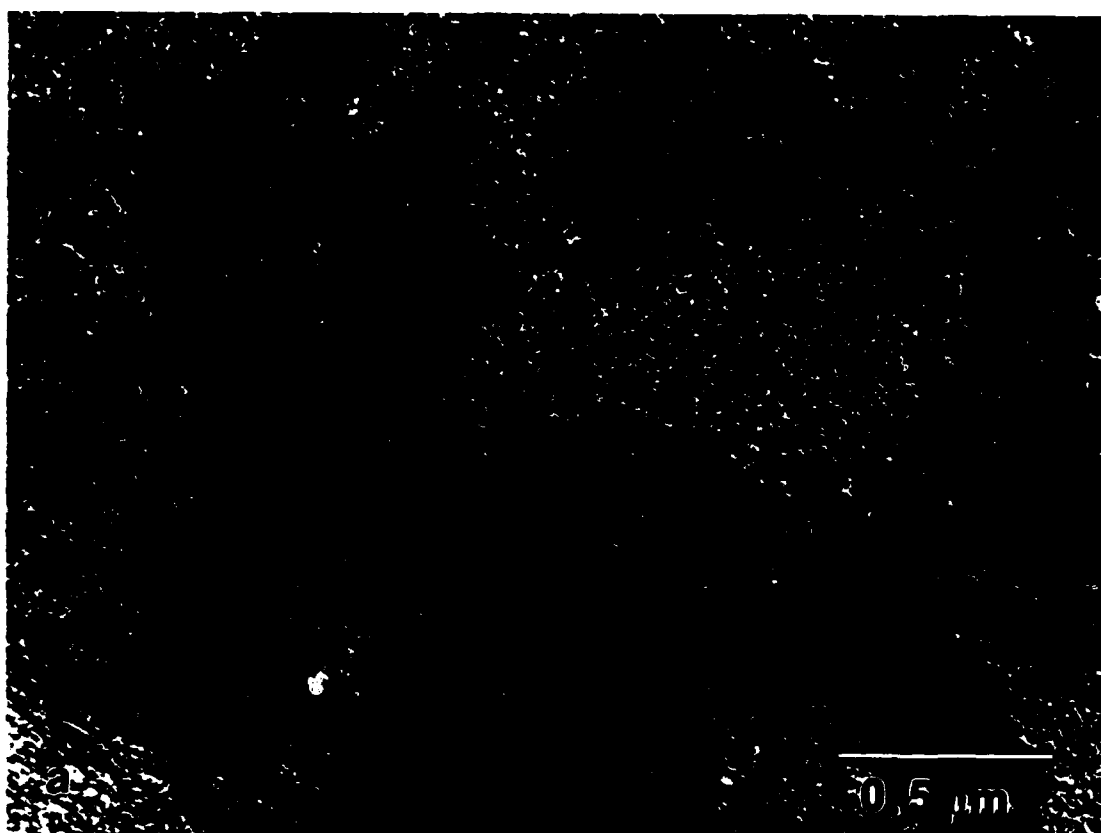


Fig. 34 a) Transmission electron micrograph of ribbon of Al-8Fe-2Mo made in He showing zone A type morphology.

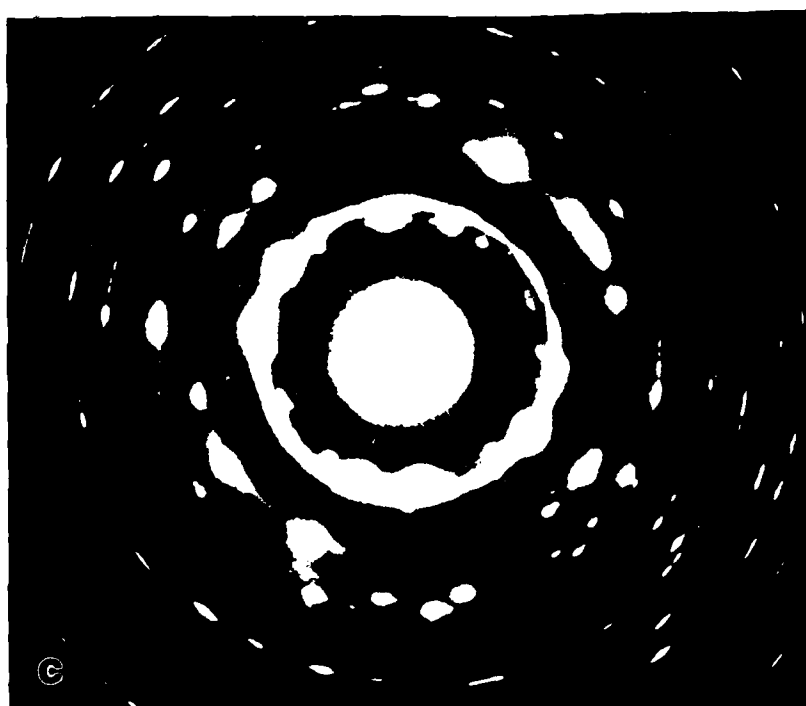
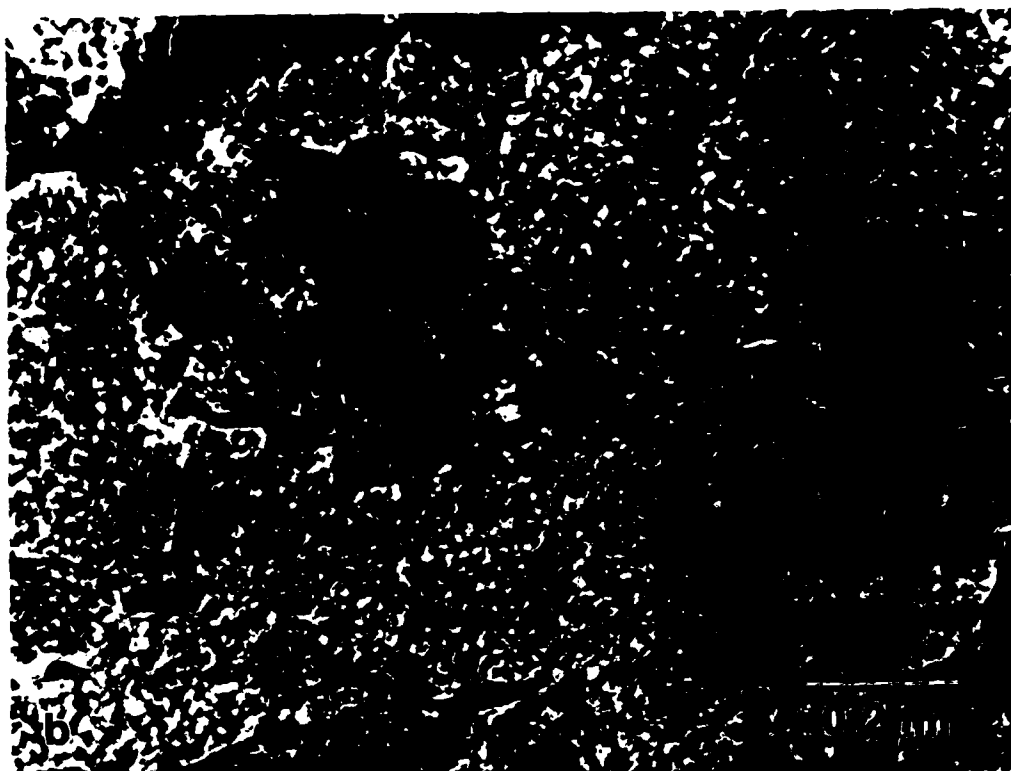


Fig. 34 b) Transmission electron micrograph of He ribbons of Al-8Fe-2Mo showing another typical morphology of zone A, c) SAD pattern of a grain interior showing α -Al spots along with continuous rings due to the very fine crystalline phase in the intercellular regions.

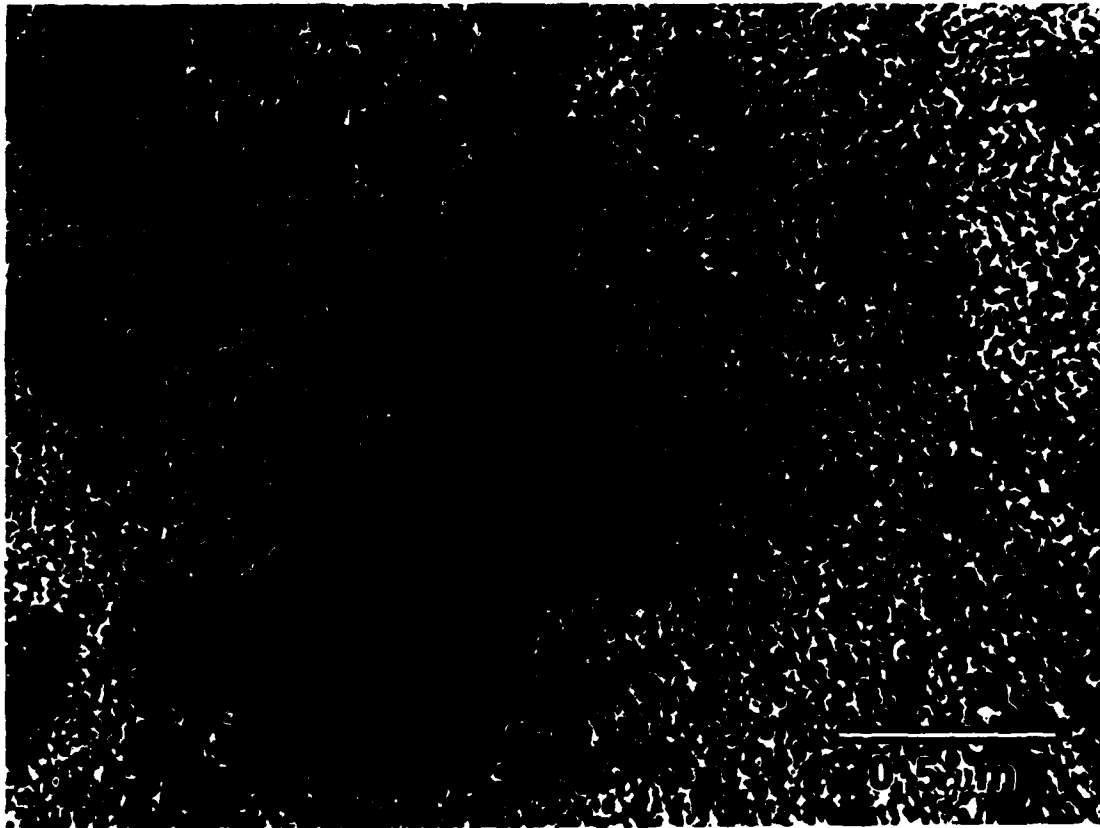


Fig. 34 d) Transmission electron micrograph of ribbon of Al-8Fe-2Mo made in vacuum which contains coarser particles than the ribbon made in He. Compare to Fig. 34a.



Fig. 34 e) Transmission electron micrograph of ribbon of Al-8Fe-2Mo made in vacuum which has coarser particles compared to those in the ribbon made in He. Compare this to Fig. 34b. f) SAD pattern which consists almost entirely of discrete maxima. The intercellular phase that gave rise to rings in 34c) has decomposed and coarsened so that only spots are seen.

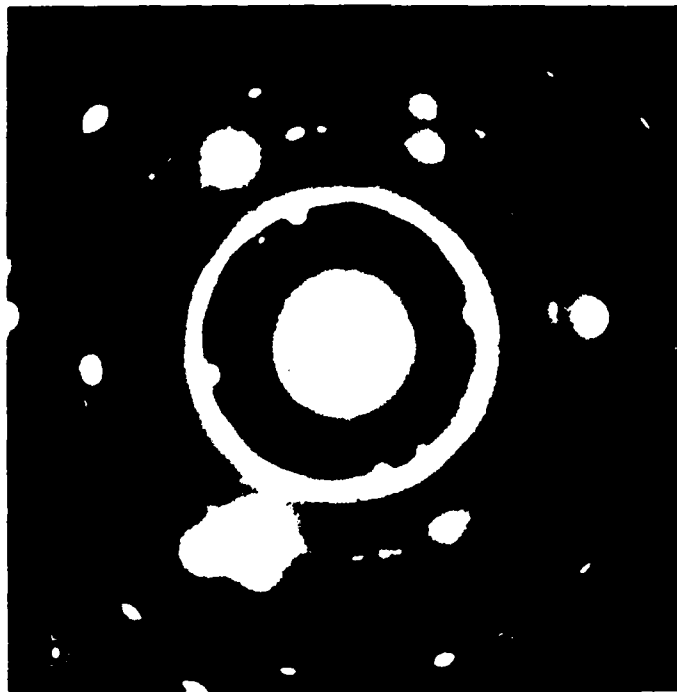
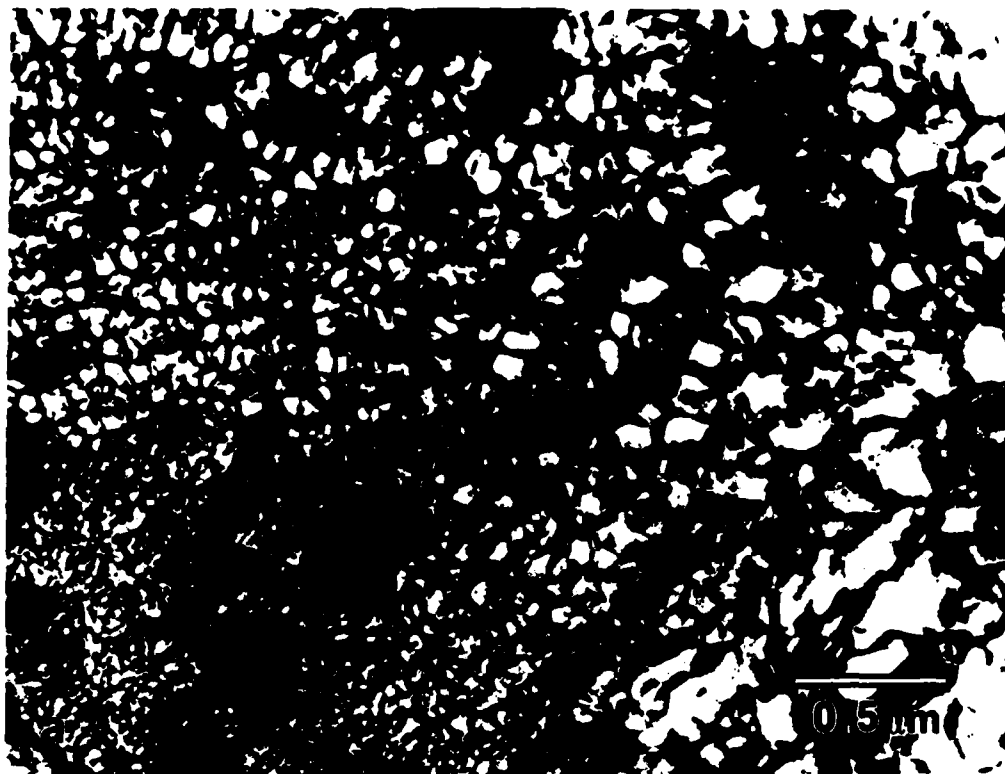


Fig. 35 a) Transmission electron micrograph of another zone A morphology in Al-8Fe-2Mo which is observed most commonly in the ribbon made in He.
b) SAD pattern of the above structure.



Fig. 36 a) Transmission electron micrograph of the top surface of ribbon of Al-8Fe-2Mo made in vacuum. b) SAD pattern of the above structure.

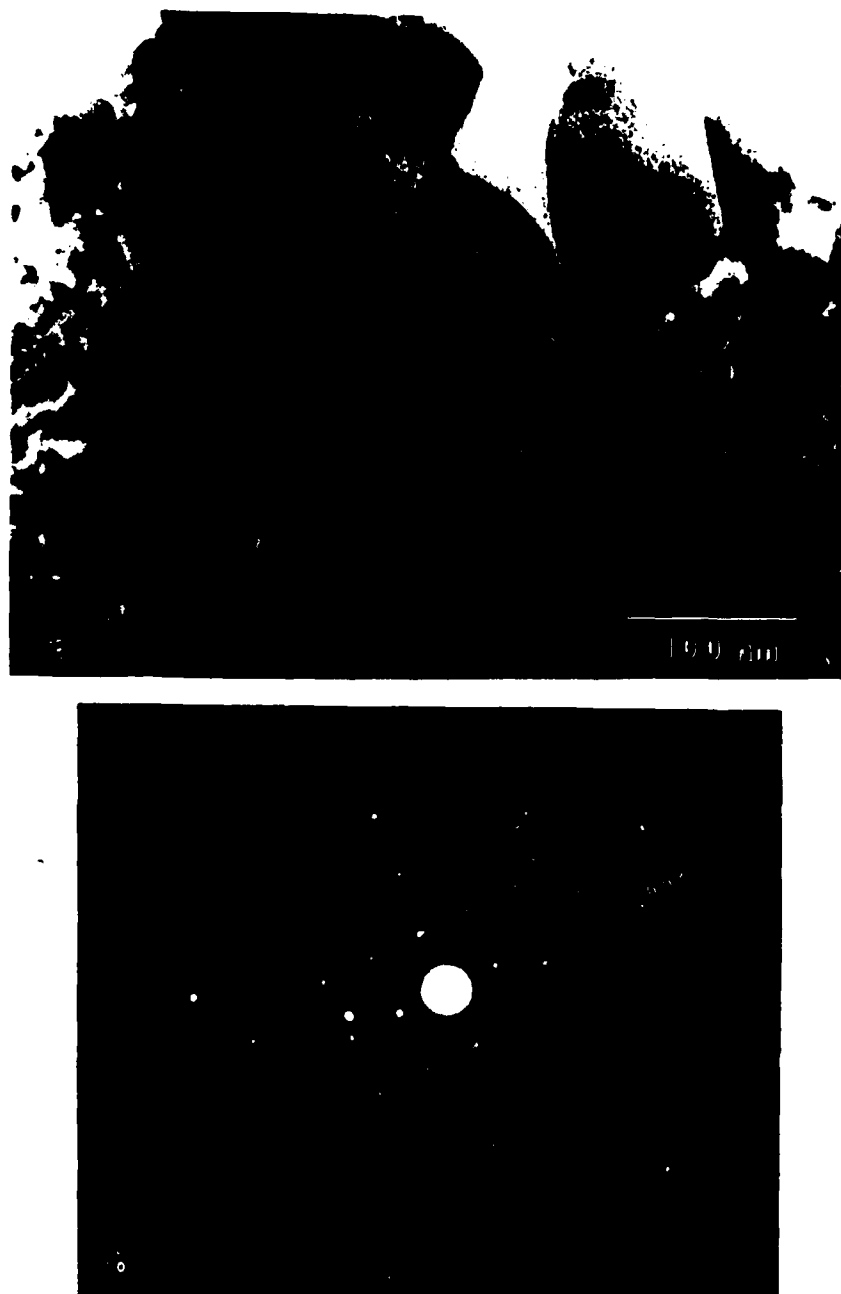


Fig. 37 Identification of one of the phases present in the ribbon of Al-8Fe-2Mo made in vacuum. a) Transmission electron micrograph of an Al_6Fe particle. b) [010] pole of the Al_6Fe particle.

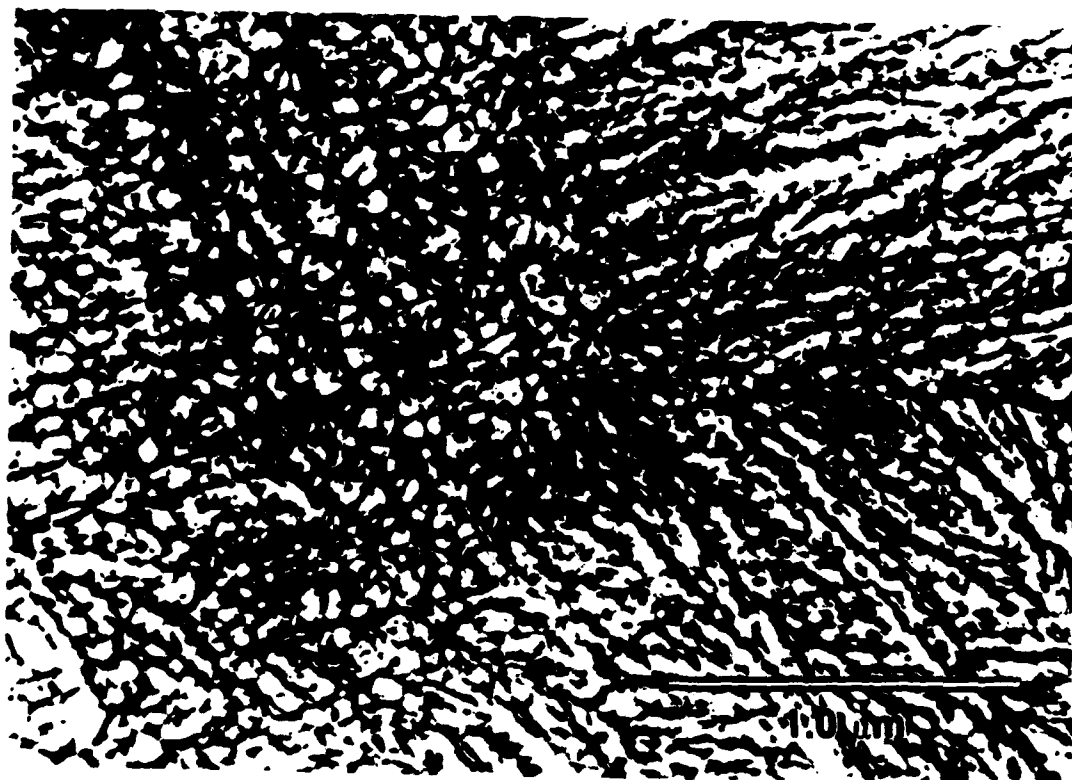
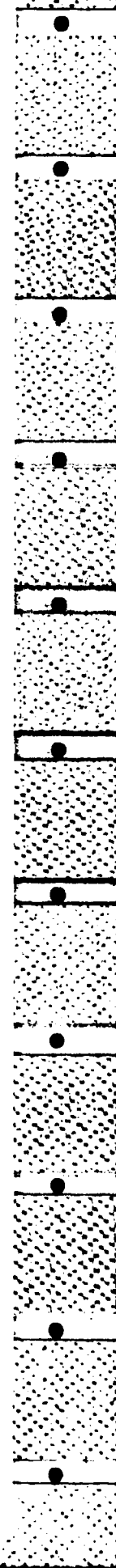


Fig. 38 Transmission electron micrograph showing the microstructure of laser surface melted Al-8Fe-2Mo. This microstructure is essentially identical to that produced by melt-spinning (Fig. 35).



Fig. 39 Optical micrograph of a laser surface melted region of Al-8.0Ni (at.%) showing regions of zones A and B.



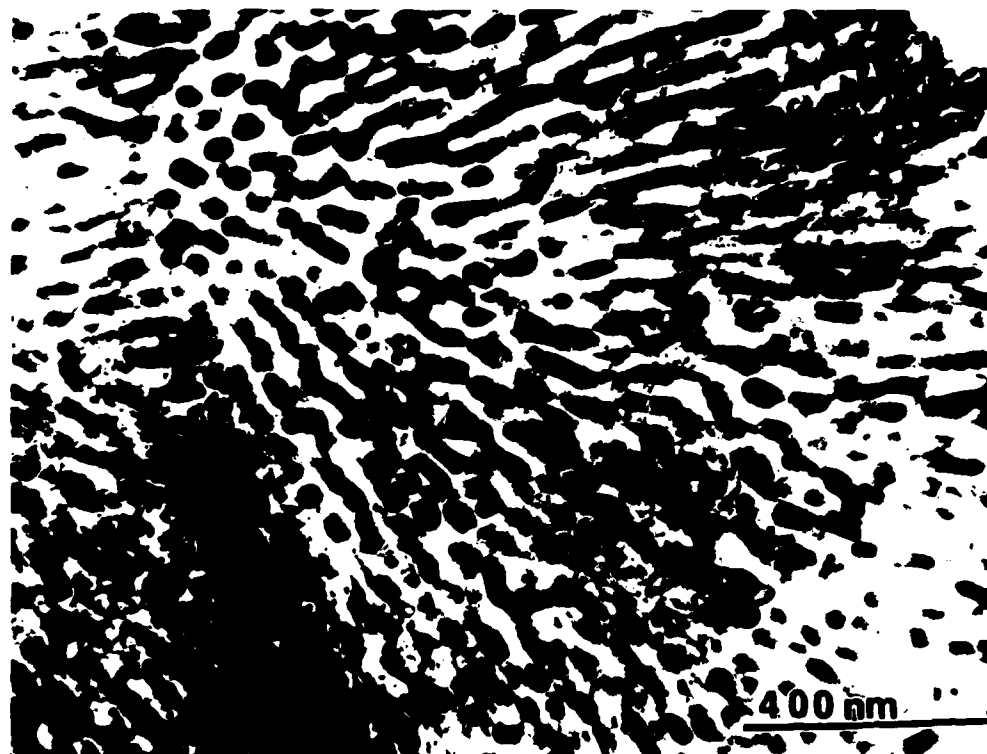


Fig. 40 Transmission electron micrograph of a melt-spun ribbon of Al-6.0Ni (at.%) which is essentially identical to that produced by laser surface melting (Fig. 3).

4. MICROSTRUCTURES OF RAPIDLY SOLIDIFIED ALLOYS BASED ON THE Al-Fe SYSTEM

During the first year's work, a comparison was made between the microstructures of Al-8Fe-2Mo and Al-7.9Fe-2.9Ce (compositions in wt.%) when rapidly solidified using LSM. These compositions were chosen such that, while they approximate to those of alloys of commercial interest, the atomic concentrations of the solute species are equal and the ratio of Fe to the other solute element is kept constant. It was found that although the microstructures were both based on an Al cellular morphology, the Mo containing alloy was characterized by a finer dispersion of a metastable intermetallic phase at the intercellular regions. The Ce alloy contained not only this metastable phase but also a second type of precipitate which was tentatively identified as an oxide. On annealing samples which had been melted using the laser, it was found that the Mo containing alloy was considerably more resistant to microstructural decomposition than the alloy with Ce additions. During the second year's work, the microstructures of these same alloys produced by melt-spinning into He were studied so that it might be established whether these samples responded in a similar fashion to those made by laser processing. In addition, attempts were made to substitute Mo with other elements. This was done for the following two reasons. Firstly, the increased stability discussed above appears to be due to the influence of Mo on the diffusivity in Al. The origin of this effect is not well understood but it is known that Mo itself diffuses very slowly in Al. Zr diffuses even more slowly than Mo, so an alloy containing Zr in the place of Mo was reduced to melt-spun ribbon to establish whether this would result in a greater degree of thermal stability. The rapidly solidified microstructure and that following heat-treatment at 400°C have been studied and the results are presented below. Also, it appears that the addition of V can be advantageous to Al alloys⁽¹⁹⁾, and so an alloy containing V in the place of Mo was also prepared and studied as described above; these results are presented below.

4.1 Melt-Spun Ribbons of Alloys Containing Mo or Ce

Melt-spun ribbons of the alloys Al-8Fe-2Mo and Al-7.9Fe-2.9Ce were prepared using the conditions described above for the optimum rate of heat extraction. Two types of microstructure are observed in the case of the Mo containing alloy, which have been shown above in Figs. 36 (a,b) and 35. The microstructure of the Ce containing alloy is shown in Fig. 41a and a SAD pattern is presented in Fig. 41b. As can be seen, the structure is found to be cellular, but not on as fine a scale as that in the Mo alloy. This is further demonstrated by considering the diffraction pattern in Fig. 41c. Here, the rings of diffracted intensity produced by the intercellular precipitates are markedly less diffuse and somewhat discontinuous when compared with those in Figs. 34c and 35, indicating a somewhat larger and less randomly oriented set of precipitates. These are essentially the same results as obtained with LSM, except that the microstructure of the Ce alloy is somewhat coarser in the case of MSR. Heat-treatment of the melt-spun ribbons, at 400°C for 4 hours, also gives the same results as those observed in the case of LSM, i.e. the Mo containing alloy exhibits a greater degree of resistance to decomposition than the Ce alloy. The results of such annealing on the melt-spun ribbon of the alloys containing either Mo or Ce are shown in Fig. 42. Apart from some possible growth of the Al_6Fe found at the intergranular regions, the microstructure of the Mo alloy appears to be unaltered, as can be seen from the image and diffraction pattern.

4.2 Microstructures of Al-8Fe-1.9Zr and Al-8.1Fe-1.1V

As stated above, the reason for substituting Zr for Mo involved the smaller value of diffusivity in Al exhibited by Zr compared to Mo. Thus, if the resistance to coarsening observed in Mo containing alloys is due to the slow diffusion of Mo, then an even greater resistance would be expected from

alloying with Zr. The microstructure and a SAD pattern of melt-spun ribbons of the Zr containing alloy are shown in Fig. 43 (a,b), and appears to be rather similar to that of the Mo alloy, c.f. Fig. 35. Following heat-treatment at 400°C for 4 hours, marked decomposition is observed, Fig. 44. This alloy does not exhibit any improved resistance to decomposition compared with the binary (Al-9.2Fe) (whose behavior was discussed in the first annual report). It is concluded that Zr does not act in the same way as Mo. A possible explanation for this effect involves the atomic size of Zr as represented by the closest distance of approach. It was noted last year that the difference in behavior between Mo and Ce may have been due to the fact that whereas the closest distances of approach of both Fe (2.482 Å) and Mo (2.7253 Å) are less than that of Al (2.8636 Å), the corresponding value for Ce (3.6488 Å) is much larger. It was postulated that the relatively small amount of Ce trapped in the Al cells, measured using energy dispersive x-ray spectroscopy (EDS) in combination with scanning transmission electron microscopy (STEM), was due in part to this difference of atomic sizes. Zr has a closest distance of approach of 3.1790 Å, which again is somewhat larger than that of Al. Therefore, the amount of Zr trapped in the cells might also be small and so the ability of Zr to reduce the diffusivity in these regions would be necessarily limited. In fact, the concentration of Zr in these regions has not yet been determined experimentally.

Finally, as mentioned above melt-spun ribbons of Al-8.1Fe-1.1V were produced. The microstructure of most of the material rapidly solidified in this way consists of the cellular morphology typical of zone A. An example is shown together with a SAD pattern in Fig. 45 (a,b). This microstructure shows no increased resistance to decomposition when heat-treated at 400°C when compared to the binary alloy.

An interesting microstructure has been produced by melt-spinning a quaternary alloy containing Al-6.8Fe-2Mo-1.1V and is shown in Fig. 46 (a,b) with a SAD pattern being presented in Fig. 46c. This morphology is rather different from those described above in that it appears that the cellular microstructure has been replaced by one involving a refined distribution of small precipitates within an Al matrix. The second phase appears to be of the same nature as that formed in the cellular microstructures, as can be seen from the SAD in Fig. 46c. It is tempting to speculate that this structure may be the result of coupled growth where the growth velocity of the intermetallic phase is somewhat slower than that of the Al. The origin of this microstructure is currently under investigation. When heat-treated at 400°C for 4 hours, there is no detectable change in the microstructure of the material, Fig. 47. Again the presence of the Mo appears to impart extremely significant resistance to thermal decomposition of the microstructure.

4.3 Consolidation and Properties

Because of the emphasis placed on understanding the development of microstructures in these rapidly solidified Al alloys, it is only recently that work has commenced on the production of bulk pieces of material from which mechanical test pieces may be machined. However, it should be noted that from the viewpoint of strength and ductility, the particulate produced in the form of ribbons exhibits not only very high hardnesses (\approx 250 DPH) but also remarkable ductility, since the ribbons can be repeatedly bent back on themselves. Therefore, providing the consolidation process does not cause the microstructure to decompose significantly, rather promising tensile properties should result.

Regarding consolidation, it appears that the microstructures of the Mo containing alloys are rather stable up to temperatures of \approx 400°C. Therefore,

it is reasonable to assume that extrusion at temperatures between 350-375°C may be employed to effect consolidation without causing significant changes in structure. Preliminary results, while resulting in partially compacted material because an unsatisfactory extrusion ratio of $\approx 8:1$ was used, revealed no change in the zone A microstructure of Al-8Fe-2Mo. In addition to extrusion, work is still in progress developing dynamic powder compaction techniques where the particulate experiences no prolonged thermal excursions. Details of this work are presented below in section 6.

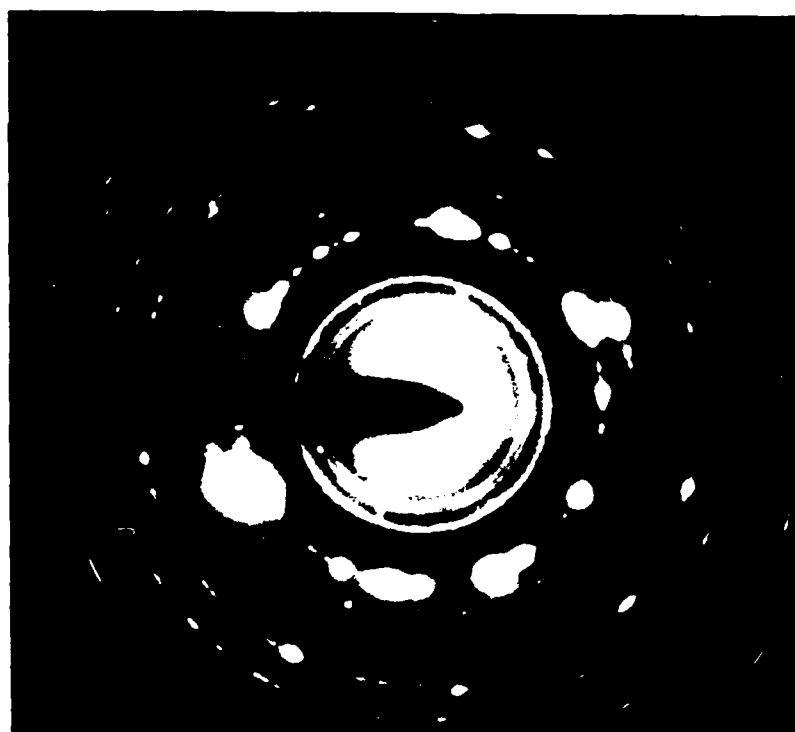
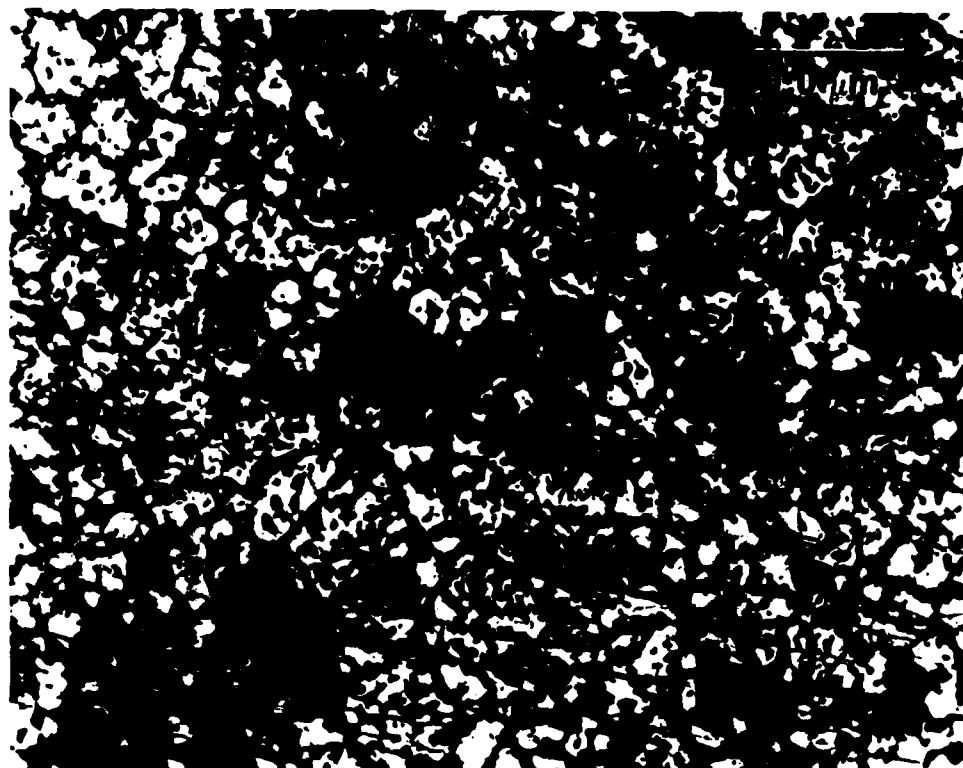
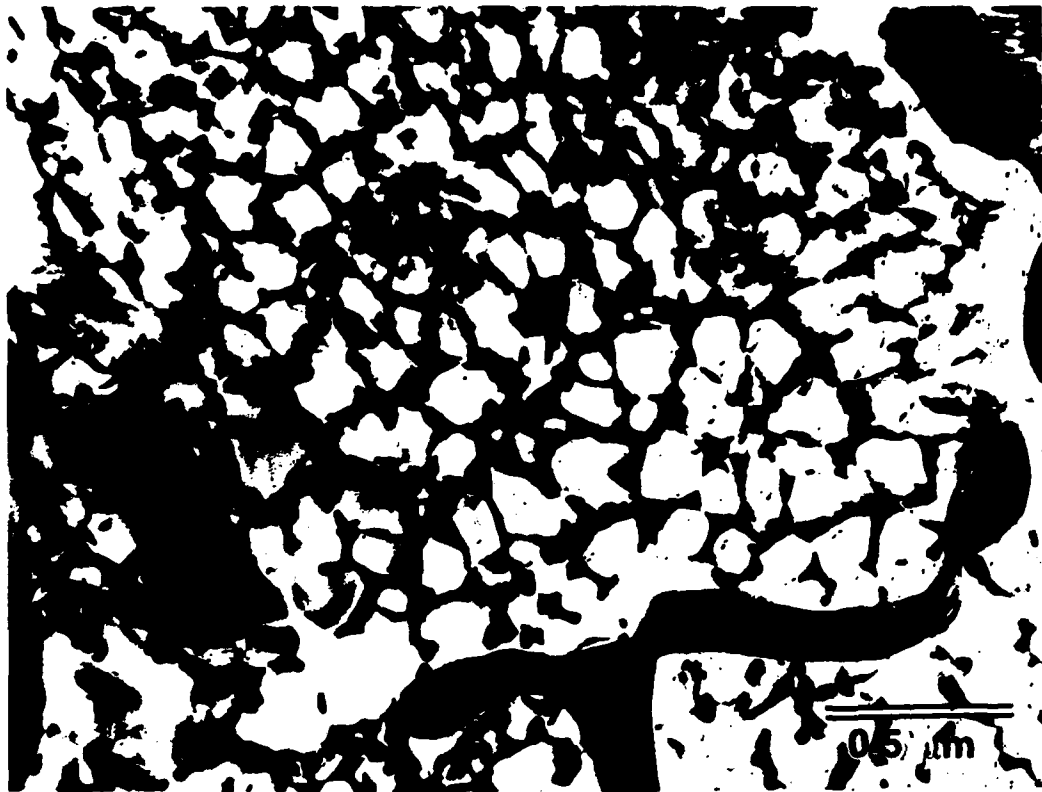
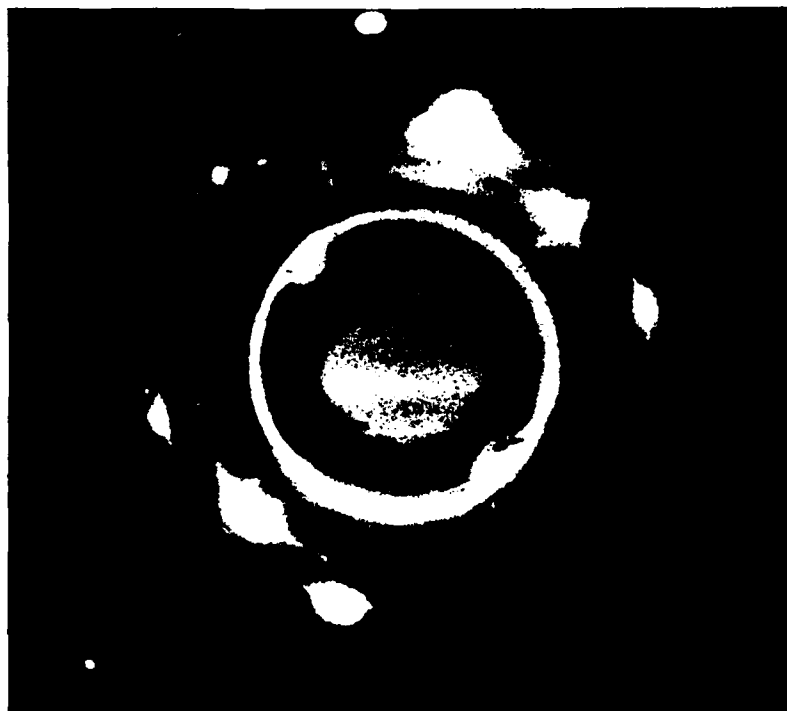


Fig. 41 a) Transmission electron micrograph of Al-7.9Fe-2.9Ce ribbon made in He. The morphology appears to be that of zone A. b) SAD pattern shows an additional set of rings made up of discrete maxima superimposed on the pattern due to the Ce-rich phase.

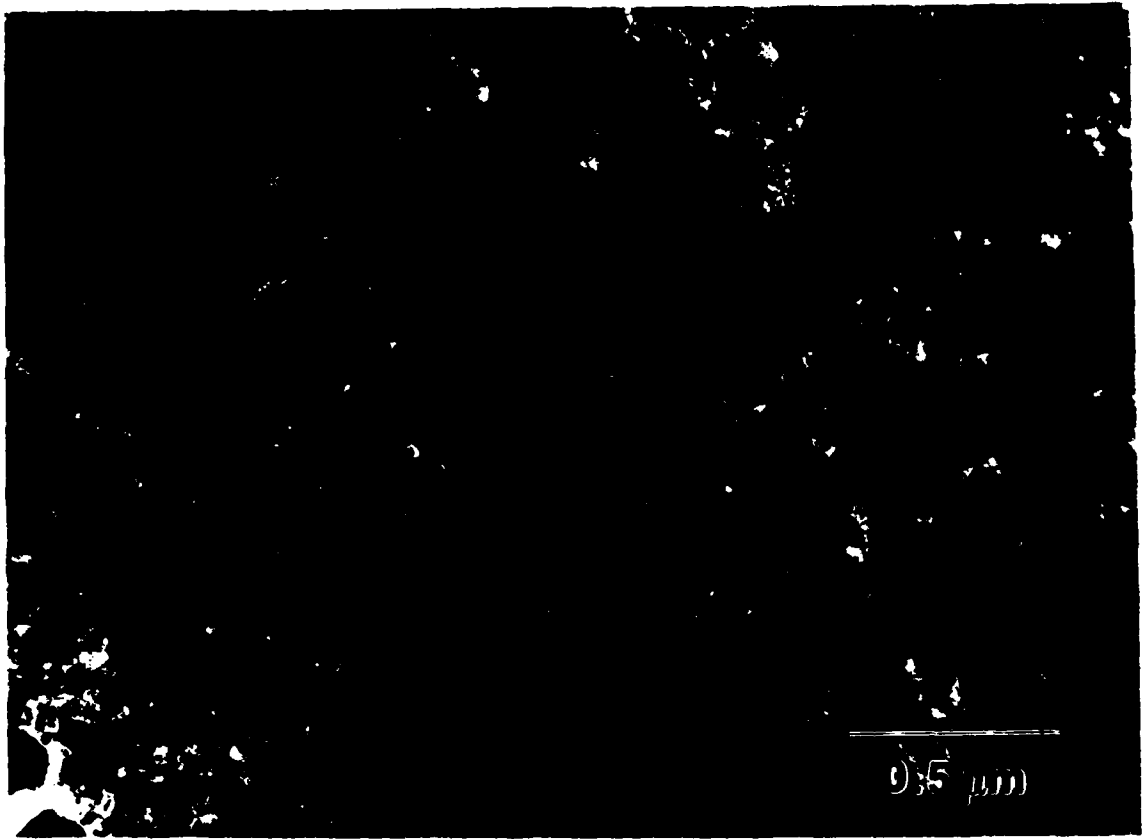


a

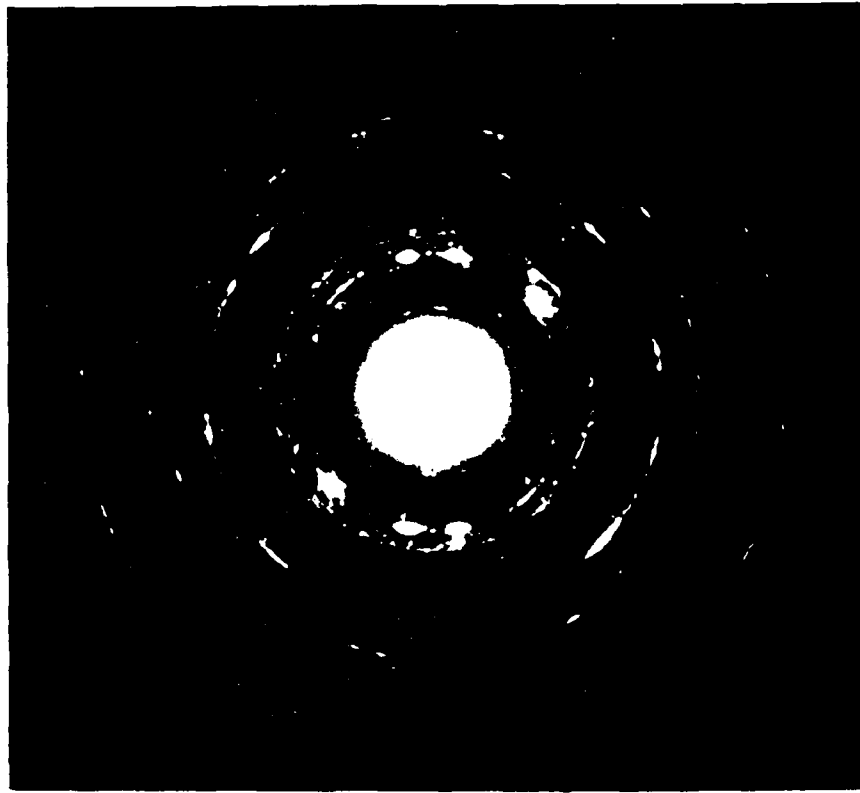


b

Fig. 42 Transmission electron micrograph a) and SAD pattern b) of Al-8Fe-2Mo ribbon that has been annealed for 4 hrs at 400°C. The SAD pattern still has strong rings coming from the intercellular regions indicating little decomposition. The phase growing at the grain boundaries is Al_6Fe .

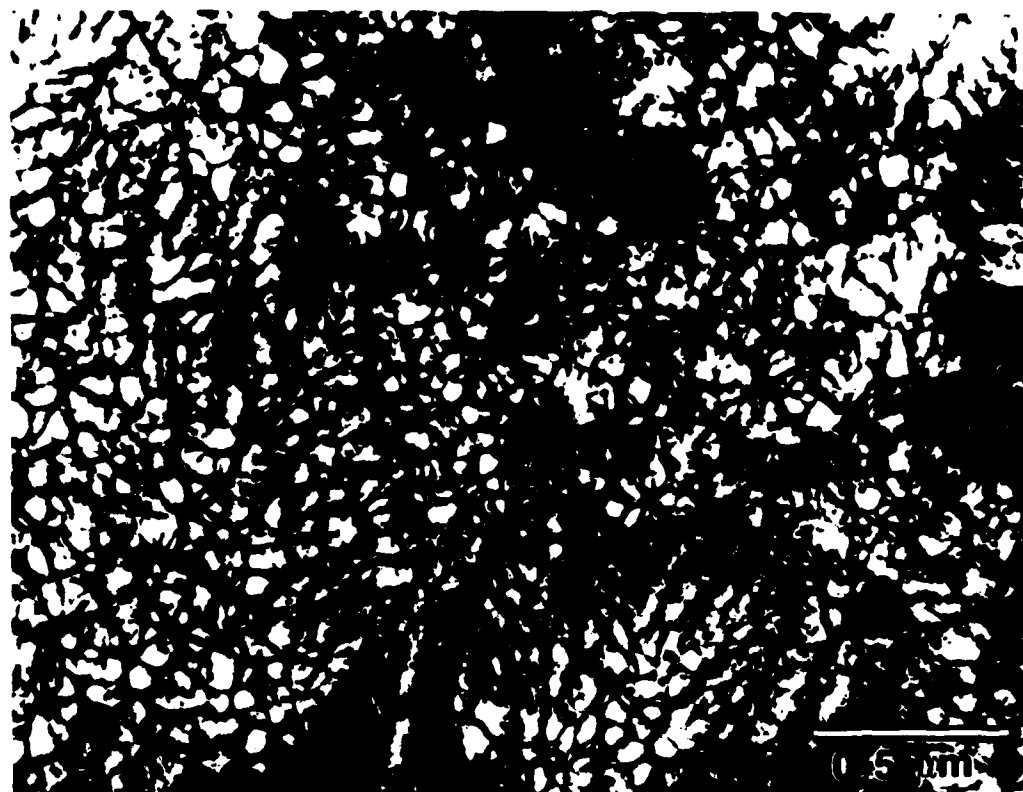


c



d

Fig. 42 Transmission electron micrograph c) and SAD pattern d) of Al-7.9Fe-2.9Ce ribbon that has been annealed for 4 hrs at 400°C. Note the decomposition and coarsening of the phase in the intercellular region compared to the Al-8Fe-2Mo ribbon.



a

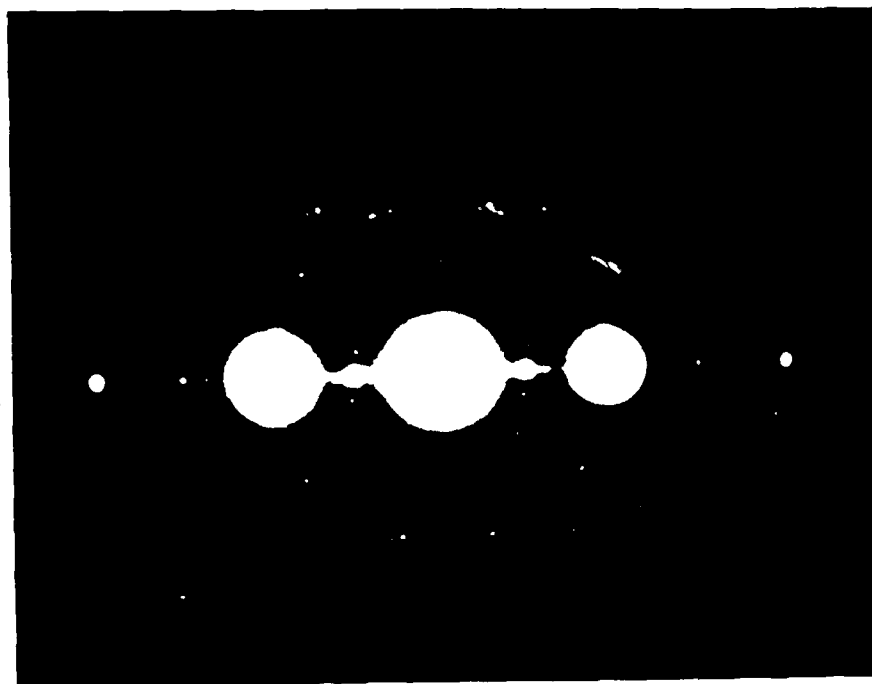


b

Fig. 43 Transmission electron micrograph a) and SAD pattern b) of Al-8Fe-1.9Zr ribbon made in the He. Both the bright field and SAD are typical of zone A.

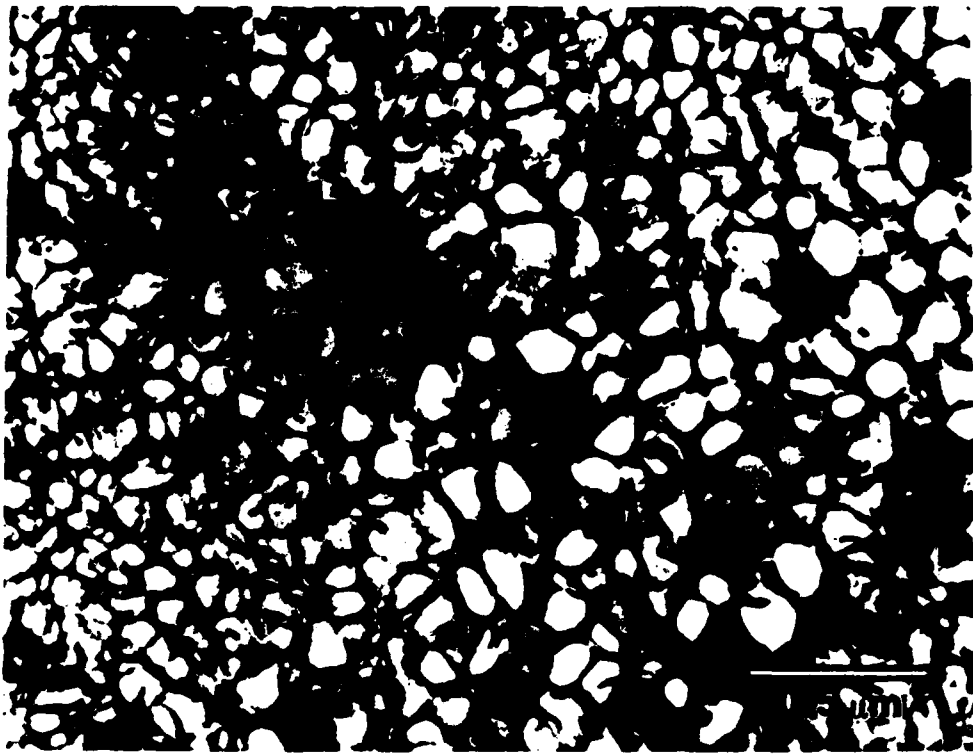


a



b

Fig. 44 Transmission electron micrograph a) and SAD pattern b) of 1-8Fe-1.9Zr ribbon made in He and annealed for 4 hrs. at 400°C. The Zr appears not to stabilize the zone A morphology.

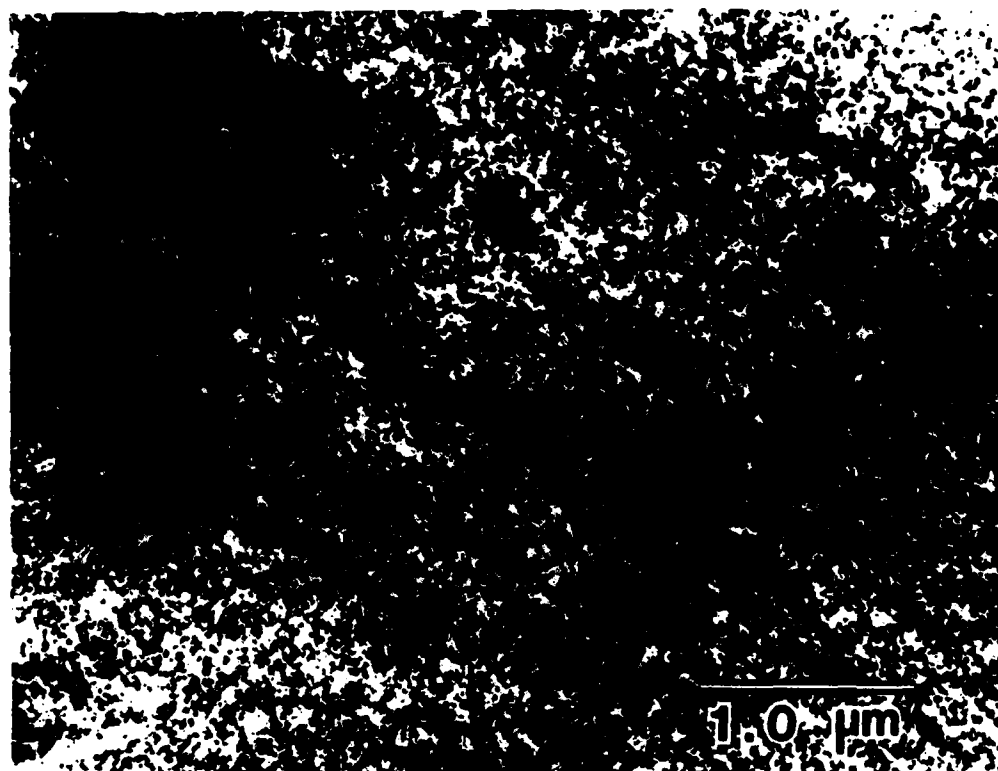


a



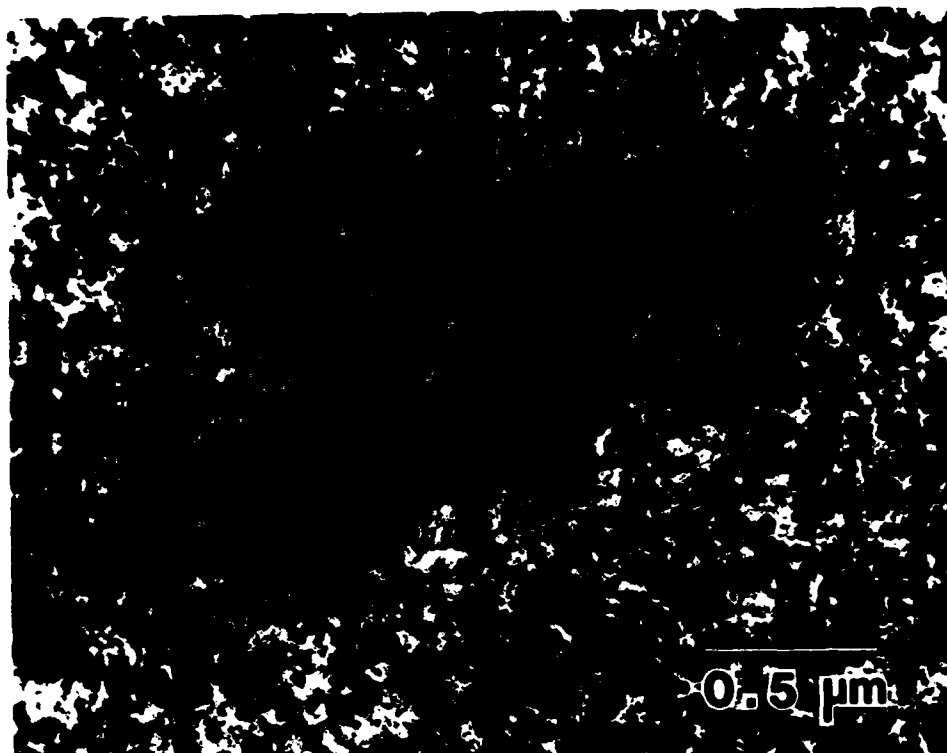
b

Fig. 45 Transmission electron micrograph a) and SAD b) pattern of Al-8.1Fe-1.1V ribbon made in He. The structure appears to be typical zone A.

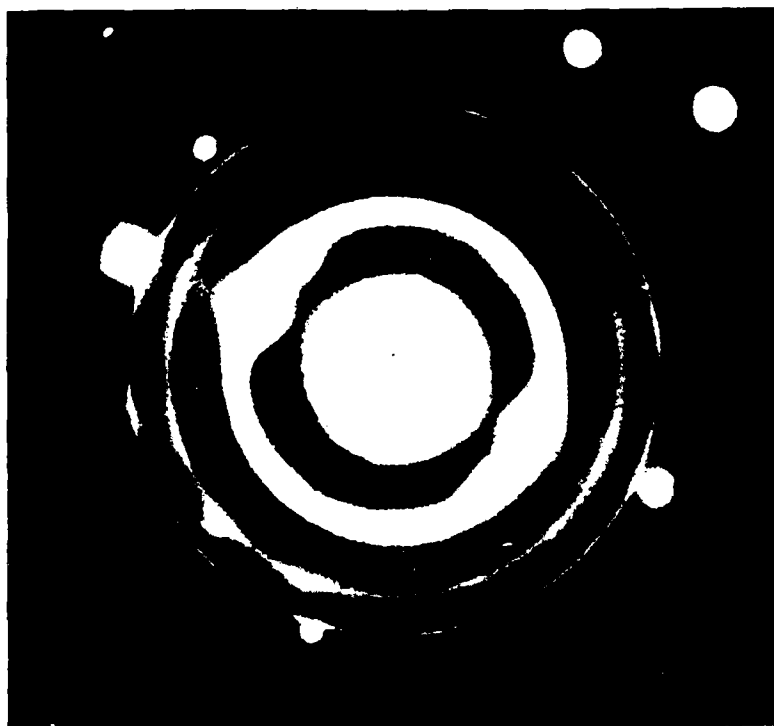


a

Fig. 46 a) A bright field micrograph of Al-6.8Fe-2.0Mo-1.1V ribbon made in He. The structure is markedly different from typical zone A microstructures.



b



c

Fig. 46 Transmission micrograph b) and SAD pattern c) of Al-6.8Fe-2.0Mo-1.1V ribbon made in He. The particles appear to be randomly oriented since they diffract to form spotty rings.

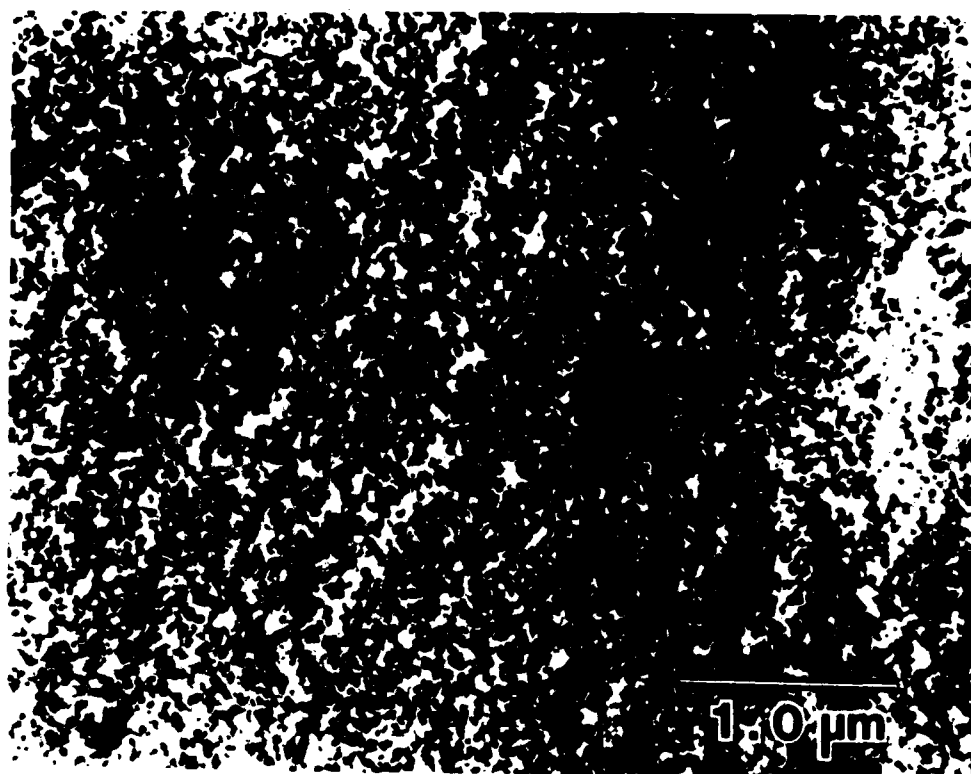


Fig. 47 Transmission electron micrograph of Al-6.8Fe-2.0Mo-1.1V ribbon made in He that has been annealed for 4 hrs at 400°C. Note the lack of both decomposition and coarsening of the particles.

5. METASTABLE PHASE FORMATION

During the course of the present program, a number of metastable phases have been formed as a result of rapid solidification. For example, one such phase is that which precipitates on an extremely fine scale in the intercellular regions of alloys based on Al-8Fe. This phase remains unidentified at this time, primarily because of the small size of the particles and the lack of an orientation relationship between precipitate and the matrix. Two other metastable phases have been observed to form in Al-Mn and Al-Mo alloys when rapidly solidified using melt-spinning. The work involved in identifying these phases is outlined below.

5.1 Al-Mn

During microstructural studies of rapidly quenched metals and alloys many new phases are found which are not present under equilibrium conditions. Indeed, investigators often discover metastable precipitates in rapidly solidified materials which generally decompose during subsequent heat treatment. Such phases may contain high concentrations of lattice defects which often are rearranged into lower energy configurations. Some of these arrangements, such as multiply-twinned configurations, may result in lowered surface energy in smaller particles.^(20,21)

In many cases⁽²²⁻²⁹⁾, the arrangement of defects in precipitates in rapidly quenched materials can lead to anomalous effects in the configuration of and diffraction data obtained from such particles. In the current study, precipitates which exhibit apparent icosahedral (I_h) symmetry have been observed in a rapidly solidified Al-15wt%Mn alloy.

TEM micrographs of typical precipitates are given in Fig. 48. The precipitates are oriented such that their 5-fold and 3-fold symmetry axes (as determined by electron diffraction) are approximately normal to the foil in Figs. 48a and 48b, respectively. As can be seen in Fig. 48, the precipitates

appear as large stellated particles, with the icosahedral symmetry of the diffraction data reflected in the particle shape. X-ray energy dispersive analysis shows the precipitates to be rich in Mn (see Fig. 49).

Selected area diffraction (SAD) patterns of the 5-fold, 3-fold, and 2-fold symmetry zone axes of the precipitates are given in Fig. 50. Also contained in Fig. 50 are the angles between these various rotational symmetry axes and those of an icosahedron. Comparison between the measured and calculated angles confirms the icosahedral symmetry of the precipitates. Based on this observed icosahedral symmetry in the diffraction data, a model has been hypothesized involving multiple twinning of a distorted cubic crystal. This is illustrated in Fig. 51. The faces of a regular icosahedron are considered to be (111) planes of twenty twin-related crystals. The twin planes are of the $\{11\bar{1}\}$ type, so that the individual crystals are tetrahedrally shaped. If the cubic crystal is given a slight rhombohedral distortion ($\alpha = 92.88^\circ$) the angles between the $\{11\bar{1}\}$ planes are equal to 72° and the twenty $\{11\bar{1}\}$ tetrahedra twinned in this manner will construct an icosahedron.

Because of the complexity of this model with respect to the prediction of diffraction patterns, a series of computer programs were written to perform the following tasks: construct a three dimensional reciprocal lattice based on a given set of lattice parameters and extinction conditions; multiply twin that lattice, each new crystal being twinned with respect to the previous one; plot a plane of the reciprocal lattice (normal to any given real space direction); and simulate double diffraction both within individual crystallites and between crystallites. Results from this program for the $[110]$ direction in the first twin are shown in Fig. 52, based upon a distorted diamond cubic crystal structure ($a = 0.36\text{nm}$) Fig. 52a shows the simulation of the diffraction pattern from the first twin. In Fig. 52b, the contributions

from all twenty twins are shown. Fig. 52c shows the effect of double diffraction on the simulated pattern and Fig. 52d shows the experimentally obtained pattern. Excellent agreement between the simulated and experimentally obtained patterns was found with any deviations between calculated and measured interplanar angles and spacings well within experimental error. Reflections in the experimental pattern which are not included in the simulation can be easily explained as resulting from triple diffraction. The highly dynamic nature of diffraction in these precipitates can be understood in terms of the fine size of the crystallites. Fig. 53 is a weak beam micrograph of the precipitate shown in Fig. 1a taken using a (111) reflection. From this micrograph, the crystallite size can be estimated to be $\sim 50 \text{ \AA}$.

Five-fold symmetry resulting from multiple twinning has been observed previously in fcc and diamond cubic materials which were evaporated onto a substrate⁽²³⁻²⁹⁾. In these studies, particles consisting of either five individual crystallites, forming a pentagonal decahedron, or twenty crystallites, forming an icosahedron, were observed. Diffraction analysis confirmed the twinned nature of these particles⁽²⁴⁻²⁹⁾ and surface energy calculations have shown these configuration to be stable for small particle sizes ($\lesssim 100 \text{ nm}$)^(20,21). However, in all cases these particles were found to consist of single units comprised of five or twenty individual crystallites, so that no long range anomalous symmetry, such as that found in this study, was observed. In the Al-Fe system, precipitates in the form of 10-pointed stars have been observed in chill cast material⁽¹¹⁾. This observation has also been explained in terms of multiple twinning, resulting in a five-fold axis, but not involving icosahedral symmetry. No supporting diffraction data for this model have been presented.

5.2 Al-Mo

In the report of the first year's work, observations of the formation of a metastable phase in Al-Mo alloys when melt-spun were described. This phase was tentatively identified as being Al_4Mo with a crystal structure given by the space group $Im\bar{3}m$, with a lattice parameter of 5.39 Å. A more detailed and thorough analysis has been performed since and this has revealed some errors in the first attempt. The more rigorous analysis is described below.

5.2.1 Structure of the Phase

The morphology of the phase is shown in Fig. 54. Convergent beam electron diffraction (CBED) was used to determine the point group of the structure. Convergent beam patterns (CBP's) corresponding to the electron beam being aligned accurately parallel to the $\langle 100 \rangle$ and $\langle 111 \rangle$ zone axes are presented in Fig. 55 (a and b) and Fig. 56 (a-c), respectively. The various symmetries that may be observed in these patterns are shown in Table 1. From

OBSERVED SYMMETRIES

<u>Zone Axis</u>	<u>Bright Field</u>	<u>Whole Pattern</u>	<u>Projection Symmetry</u>	<u>Deduced Diffraction Group</u>
100	-	4mm	4mm	$4mm1_R$ 4mm
111	3m	3m	6mm	$6Rmm_R$

Table 1

Convergent beam pattern symmetries and the deduced projection diffraction groups for the Al_4Mo metastable phase.

AD-A148 427

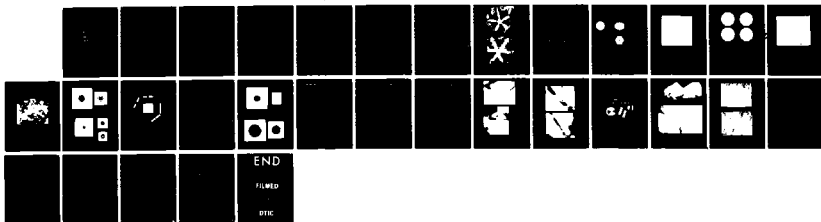
RAPID SOLIDIFICATION PROCESSING AND POWDER METALLURGY 2/2
OF AL ALLOYS(U) ILLINOIS UNIV AT URBANA DEPT OF
METALLURGY AND MINING ENGINEERING H L FRASER 29 OCT 84

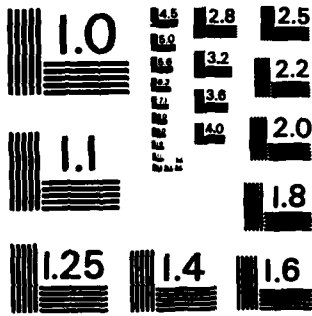
UNCLASSIFIED

AFOSR-TR-84-1818 AFOSR-82-0186

F/G 11/6

NL





MICROCOPY RESOLUTION TEST CHART
NATIONAL BUREAU OF STANDARDS - 1963 - A

these symmetry data the diffraction groups to which these patterns belong may be deduced⁽³¹⁾, and these are also shown in the table. It is possible to list the point groups that would give rise to the deduced diffraction groups⁽³¹⁾, and these are shown in Table 2. It is evident that the only consistent point

<u>Deduced Diffraction Group</u>	<u>Possible Point Groups</u>	
4mm1 _R 4mm	4/mmm 4mm	m3m
6 _R mm _R	3m	m3m

Table 2

Possible crystal point groups obtained from the deduced diffraction groups. Note m3m is the only consistent point group for all three zone axis.

group is m3m. The nature of the unit cell may be deduced by projecting the reflections in the higher order Laue zones back onto the zero order pattern. When this is done, a body-centered reciprocal lattice cell is constructed so that the real lattice cell must be of a face-centered type. The space group may be deduced from this information and a knowledge of the kinematically forbidden reflections. To establish whether particular reflections are forbidden, it is necessary to tilt the sample about given systematic rows of reflections away from poles of high symmetry where double diffraction effects are possible, and then determine the reflections which remain present when all possible double diffraction paths have been removed. An example of this is shown in Fig. 57, which shows the results of such tilting experiments from a $\langle 110 \rangle$ zone axis about four systematic rows. The results of this and other tilting experiments reveals that the forbidden reflections may be summarized

as those corresponding to the diamond cubic structure. For example, in the 100 systematic row of reflections, only multiples of 400 are allowed. This information taken with the nature of the cell and the point group determined above, yield a space group of $Fd\bar{3}m$ and a lattice parameter of 7.23 \AA .

5.2.2 Chemical Composition of the Phase

The chemical composition of the phase was determined by the use of EDS combined with STEM. To perform quantitative compositional analysis using these techniques, it is necessary to make measurements of the integrated intensities (usually some factor times the full-width at half-maximum, FWHM) of the x-ray peaks of the elements present in the phase of interest. These intensities (I_{Al} and I_{Mo} in the present example) are related to the compositions (C_{Al} and C_{Mo}) by a simple equation which is written as:

$$C_{Al}/C_{Mo} = K_{Al/Mo} \cdot I_{Al}/I_{Mo} \quad (2)$$

The factor $K_{Al/Mo}$ may be determined experimentally either by using pure elemental standards (i.e. thin foils of Al and Mo) or more simply by using a known compound standard consisting of the elements of interest. In the present study, both approaches have been followed. In the case of the pure elemental standards the value of $K_{Al/Mo}$ is determined by use of the following equation:

$$K_{Al/Mo} = I^{\circ}_{Mo}/I^{\circ}_{Al} \cdot N_{Al}/N_{Mo} \cdot \nu_{Al}/\nu_{Mo} \cdot t_{Al}/t_{Mo} \quad (3)$$

where I°_i refers to the integrated intensity of the x-ray peak from the i th standard element, N_i is the number of electrons used to generate the i th peak, ν_i is the atomic density of the i th element and t_i is the thickness of the foil of the i th element at the position where the standard spectrum was

generated. The atomic densities are well known quantities and the factors N_1 are made equal by adjusting the counting times used. From each standard, then, it is necessary to determine the integrated intensity and the specimen thickness at that point. In the case of the Mo standard, this latter quantity was done by means of convergent beam techniques which yield an accuracy of $\approx 3\%$. The specimen used in the case of Al was a simple sphere of thickness $\approx 2420 \text{ \AA}$, this being determined by direct measurement in the electron microscope. The data obtained from the pure elemental standards Al and Mo are listed in Table 3. Substitution of these values into equation (3) yields a value of $K_{\text{Al/Mo}} = 1.142$.

DATA FOR PURE ELEMENTAL STANDARDS

	<u>Counts</u>	
MoK	166906	$t = 710 \text{ \AA}$
IHC*	<u>6217</u>	
MoK	160689	
	<u>Counts</u>	
AlK	515295	$t = 2424 \text{ \AA}$
IHC*	<u>3277</u>	
AlK	512018	

Table 3

Total integrated counts at FWHM and experimentally measured thicknesses for elemental standards.

*IHC: in-hole count.

A typical spectrum obtained from the metastable phase is shown in Fig. 58. When the integrated intensities are deduced from several such spectra, after contributions to these spectra from unfocussed radiation being incident on the sample have been subtracted, and are substituted together with the value of $K_{Al/Mo}$ into equation (2), an average value for the composition for the phase is found to be Al-19.50 Mo (in at.%). This corresponds approximately to Al_4Mo .

It is important to establish confidence in this method of analysis, and so the value of $K_{Al/Mo}$ obtained from thin foils was used to determine the composition of a known standard. An apparently stable line compound in the Al-Mo system is $Al_{12}Mo$, which can be precipitated in equilibrium with the solid solution based on Al. Samples of Al-13Mo (at.%) were aged at 650°C for 48 hours to promote coarsening of the $Al_{12}Mo$. In this way, large particles of the compound standard could be produced such that there would be essentially no spectral contributions from the surrounding Al-rich matrix. At first, CBED patterns were recorded from the compound standard so that its structure might be determined. In this way, the exact identification of the standard was established. The CBP's obtained with the beam aligned accurately parallel to the $\langle 001 \rangle$ and $\langle 111 \rangle$ zone axes are shown in Figs. 59 and 60. The various symmetries observed in these patterns are listed in Table 4, from which it is possible to deduce the possible diffraction groups to which the patterns belong. When the possible point groups corresponding to these diffraction groups are considered (Table 5), it follows that only the $m\bar{3}$ point group is consistent with the available data. The nature of the unit cell can be determined in the same manner as described above, and is found to be a face-centered reciprocal lattice and therefore a body-centered real lattice. By noting the possible missing reflections, and combining this information with the point group and type of unit cell yields a space group of $Im\bar{3}$ with a

OBSERVED SYMMETRIES

<u>Zone Axis</u>	<u>Whole Pattern</u>	<u>Projection Symmetry</u>	<u>Deduced Diffraction Group</u>
100	2mm	2mm	2mm1R 2mm
111	3	6	6R

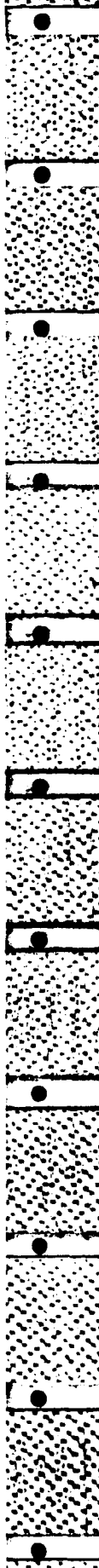
Table 4

Convergent beam pattern symmetries and the deduced projection diffraction groups for Al-Mo standard.

<u>Deduced Diffraction Group</u>	<u>Possible Point Groups</u>		
2mm1R	mmm	4/mmm	m3m
2mm	mm2	3m	6m2
6R	m3		
	3		

Table 5

Possible crystal point groups obtained from the deduced diffraction groups.
Note m3 is the only consistent point group for all three zone axis.



lattice parameter of 7.49 Å. This analysis is in good agreement with the data listed in the literature⁽³²⁾. When the integrated intensities for the x-ray peaks determined from several spectra recorded from the compound are used together with the value for $K_{Al/Mo}$ in equation (2), an average composition of Al-7.85Mo (at.%) is obtained. This is to be compared with the known value of Al-7.69Mo. Clearly, this result permits a great deal of confidence to be placed in the analysis.



Fig. 48 TEM micrographs of two examples of the Al-Mn precipitates displaying icosahedral symmetry a) with the 5-fold axis approximately normal to the foil, b) with the 3-fold axis approximately normal to the foil.

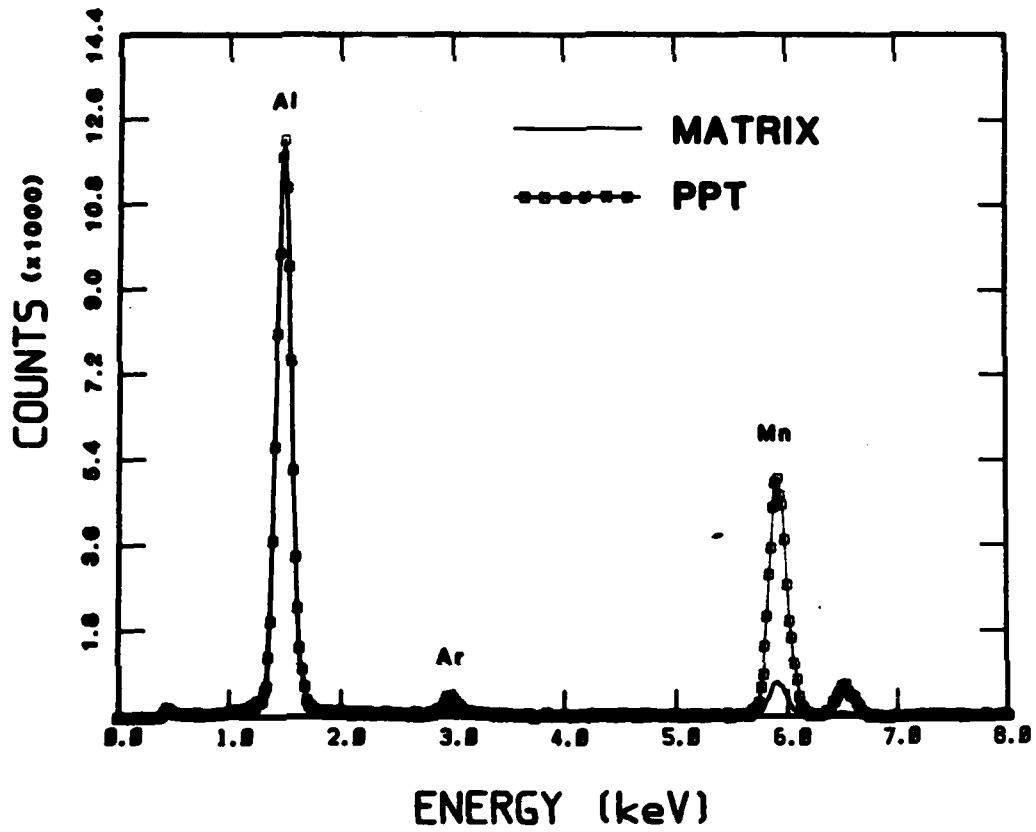


Fig. 49 Results from x-ray energy dispersive analysis (performed in the TEM) showing the high Mn content of the precipitates.

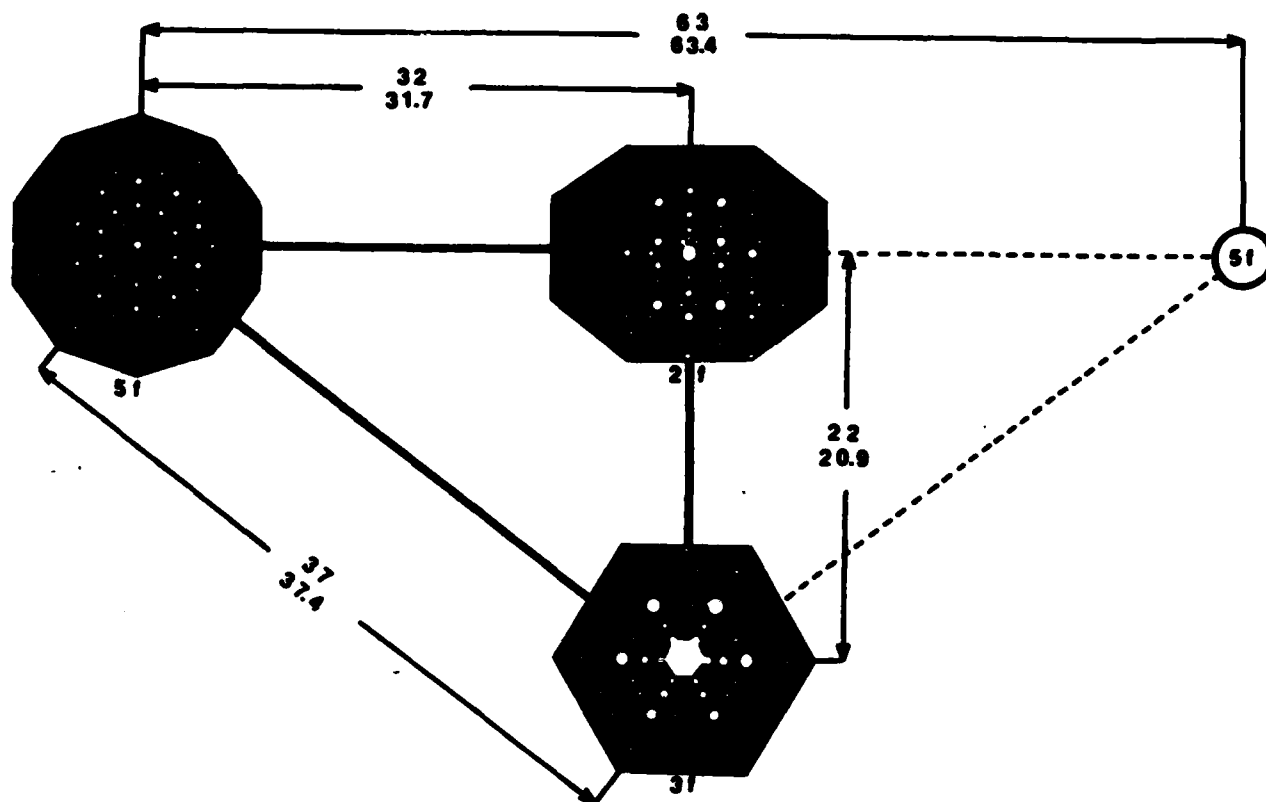


Fig. 50 Selected area diffraction patterns of the major zone-axes of the precipitate, showing the icosahedral symmetry. Also shown are the angles between these axes of symmetry as measured from the precipitate (top) and calculated for the icosahedron (bottom).

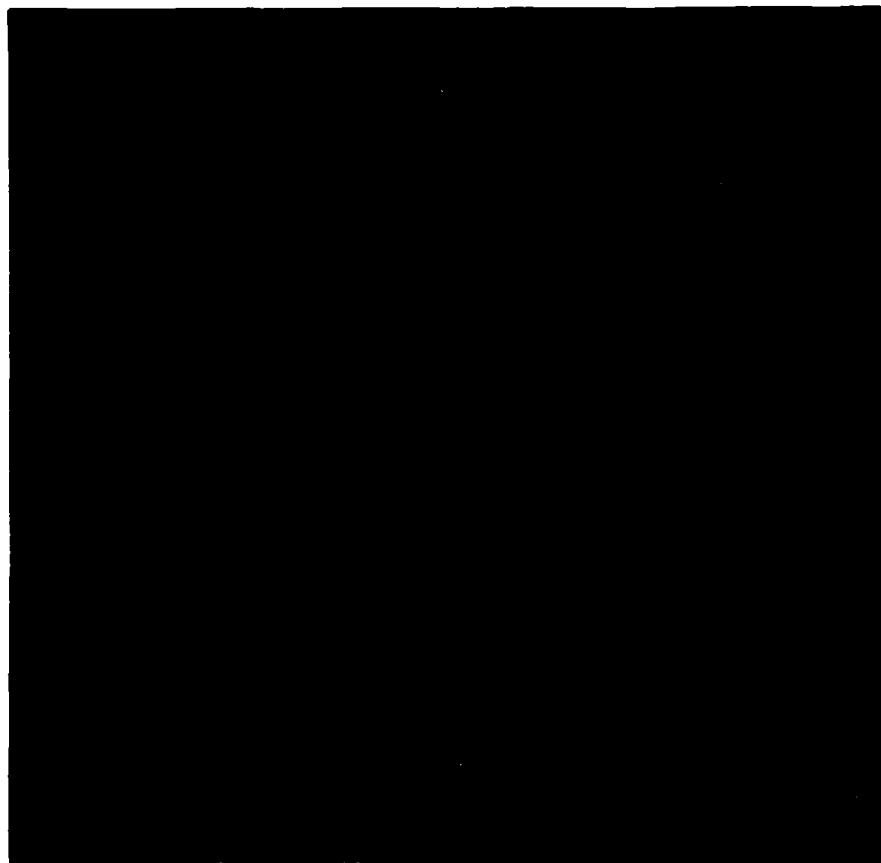
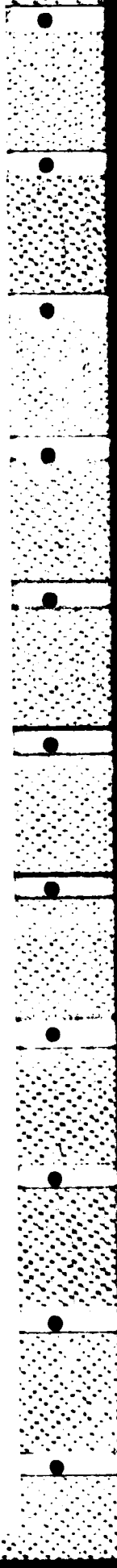


Fig. 51 Illustration of the icosahedral model in which the faces of the icosahedron represent (111) planes of multiply-twinned rhombohedral crystals.



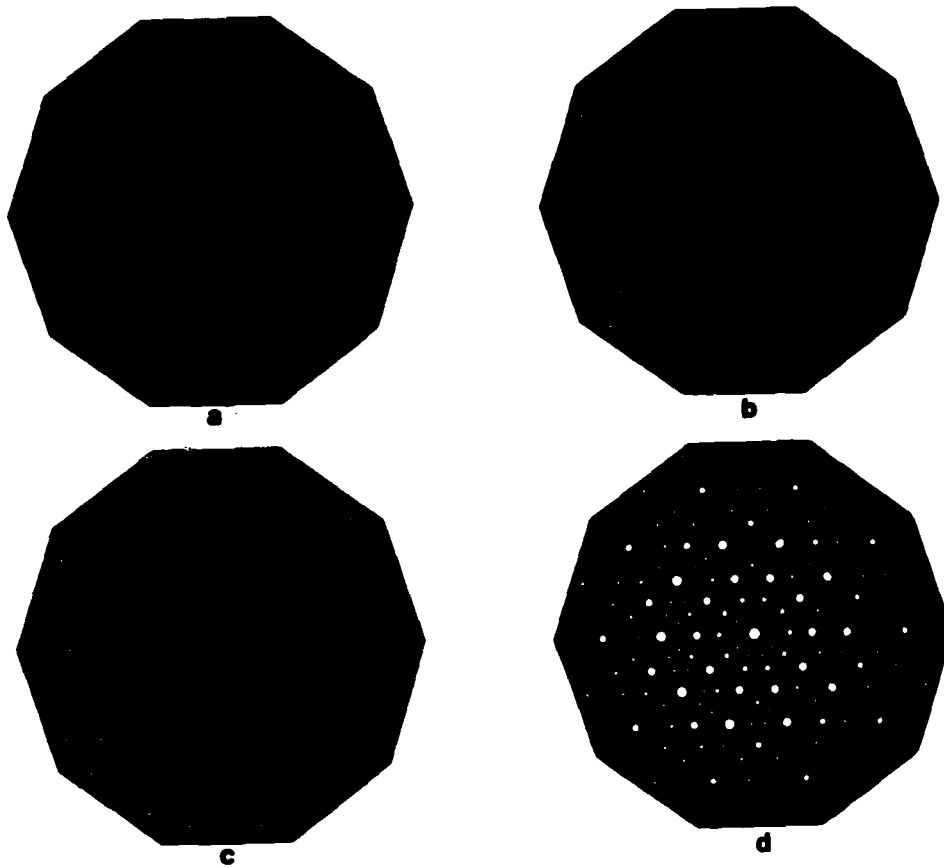


Fig. 52 Comparison of the simulated (a-c) and experimentally determined (d) diffraction patterns. a) contribution of first crystal b) contributions from all twenty multiply-twinned crystals c) effect of double diffraction d) experimentally obtained pattern.

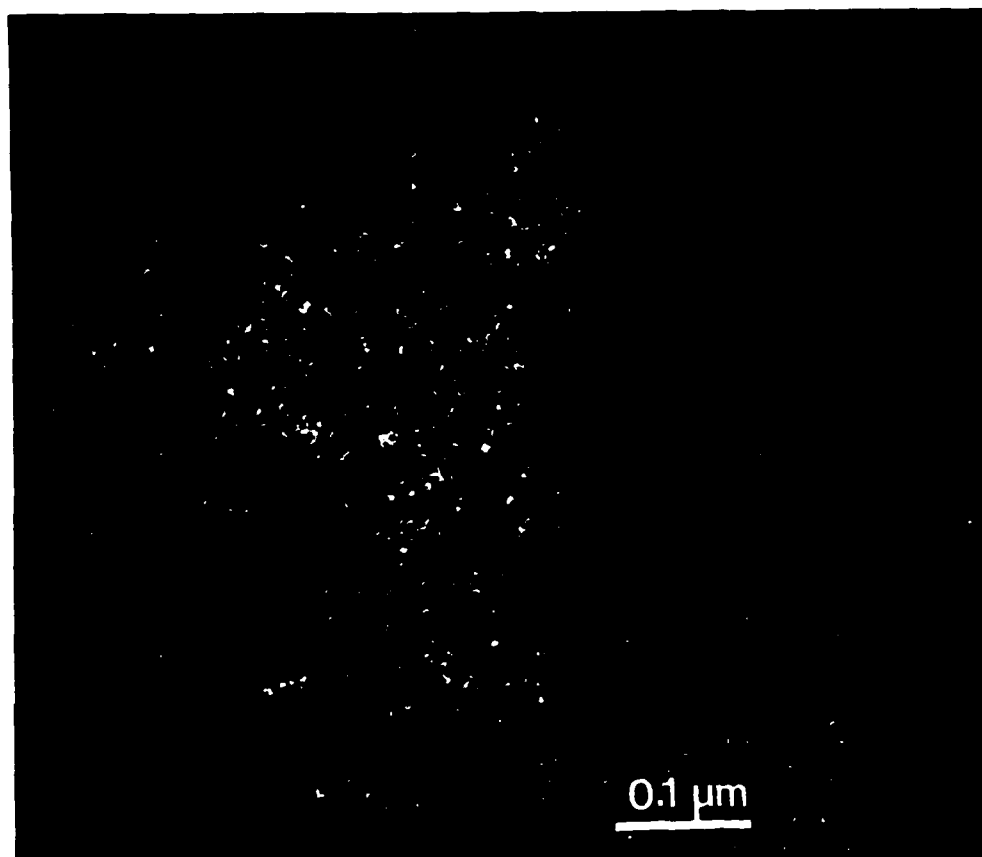


Fig. 53 Weak beam TEM micrograph ($g = 11\bar{1}$) of precipitate shown in Fig. 1a, showing extremely fine crystallite size.



Fig. 54 Micrograph of dispersed metastable secondary phase in α -Al matrix of melt spun Al-5.0 wt.%Mo ribbon.

001

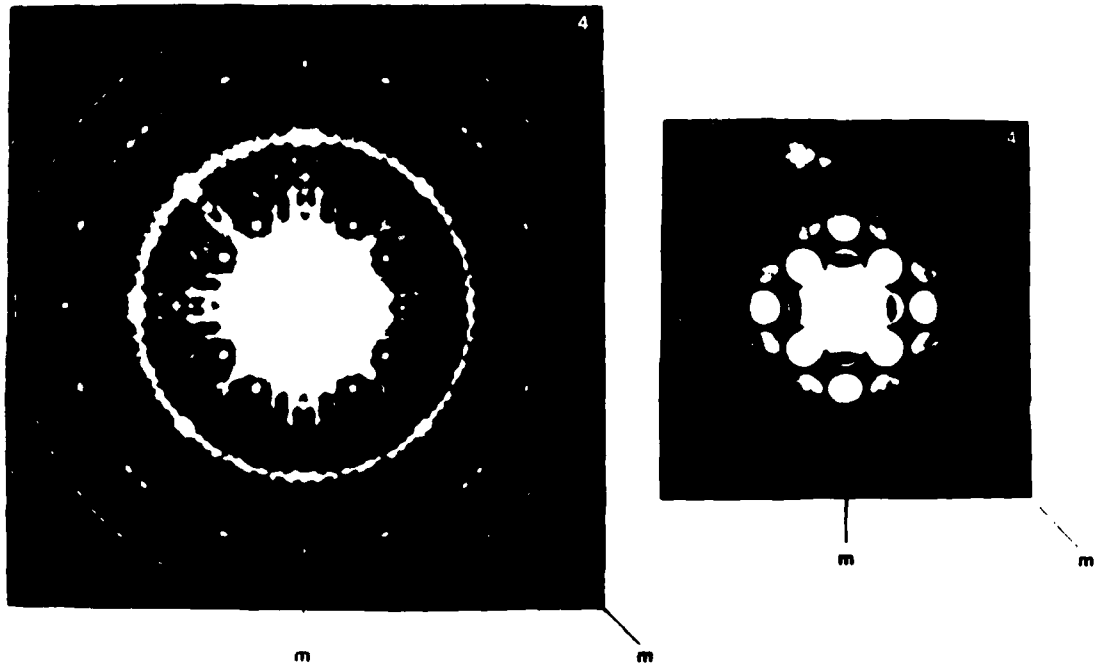


Fig. 55 Convergent beam patterns for the $\langle 001 \rangle$ zone axis of the metastable

111

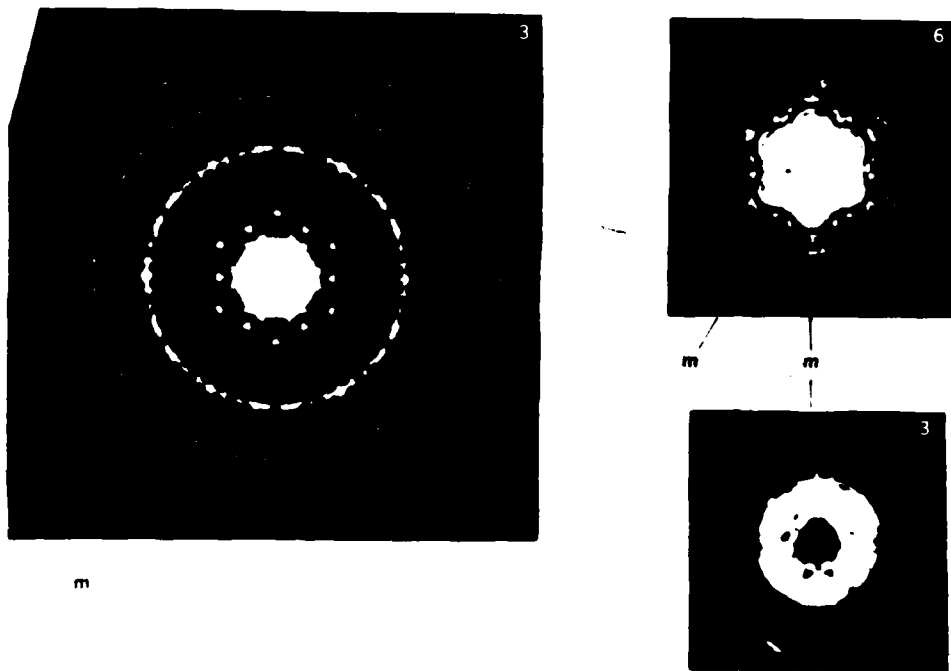


Fig. 56 Convergent beam patterns for the $\langle 111 \rangle$ zone axis of the metastable phase. Note that bright field information is present for this zone axis.

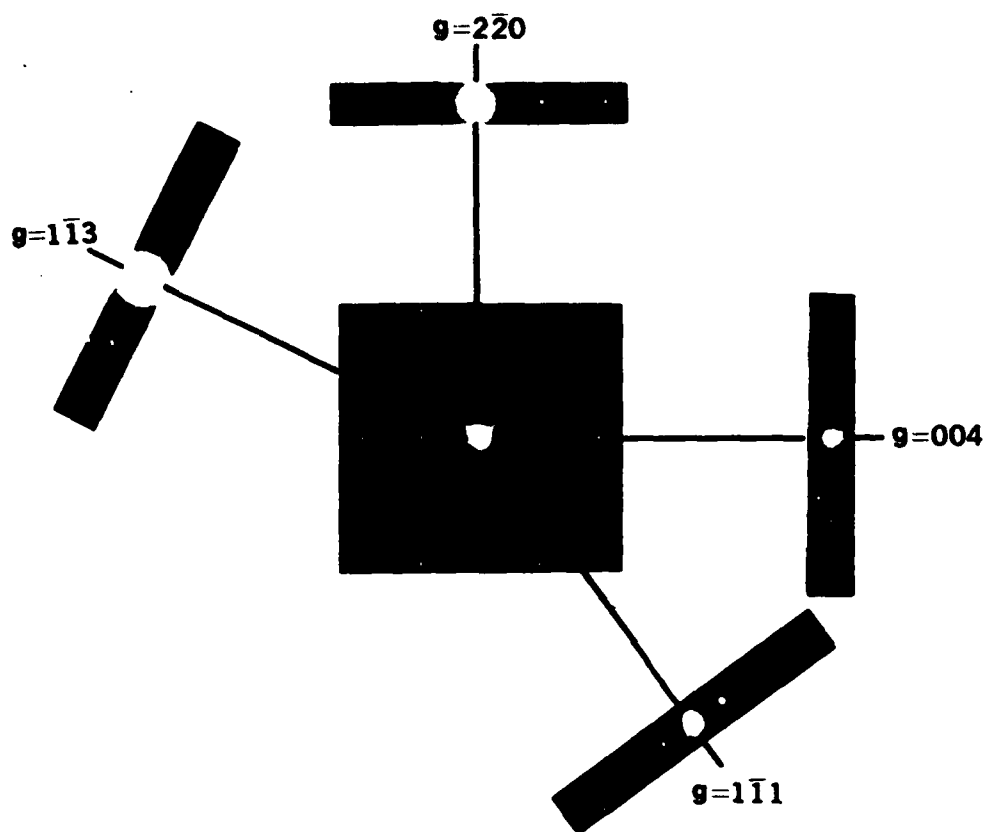


Fig. 57 $\langle 110 \rangle$ SAD pattern and systematic row obtained by tilting about zone.

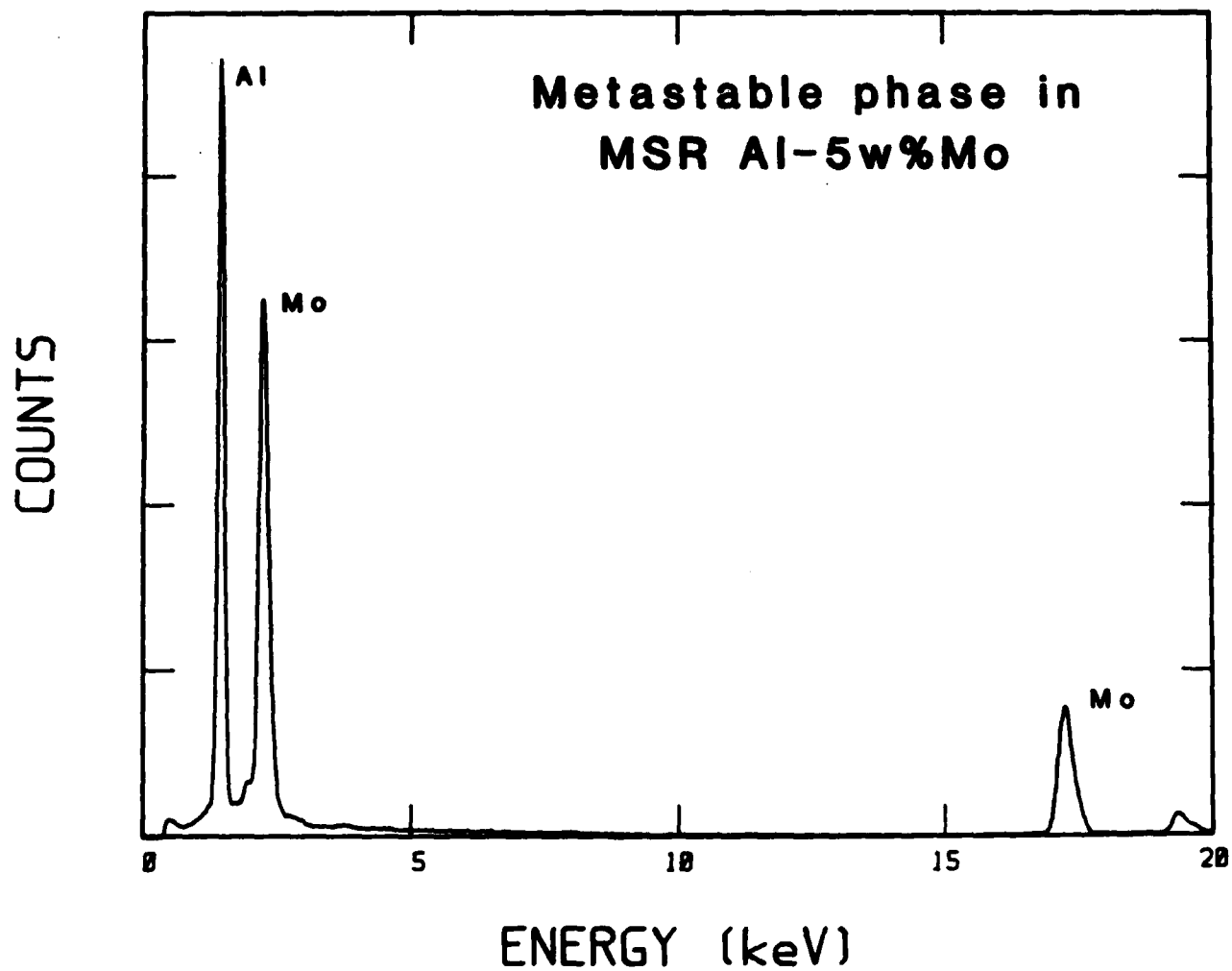


Fig. 58 Energy dispersive x-ray spectra from the metastable phase in Al-5.0 wt.%Mo melt spun ribbon.

001

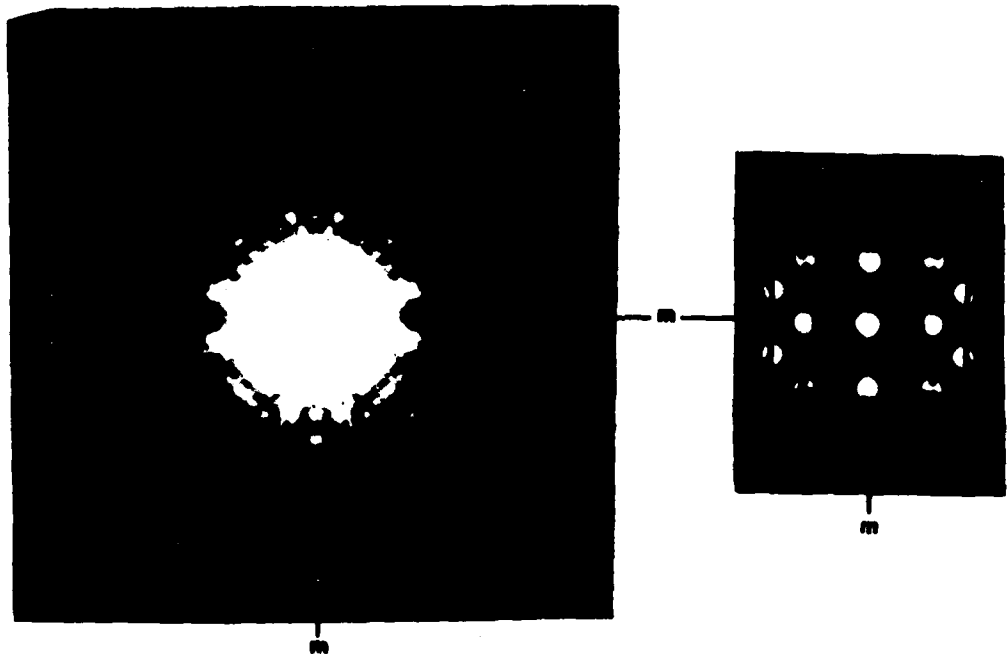


Fig. 59 Convergent beam patterns for the <001> zone axis in Al₁₂Mo.

111

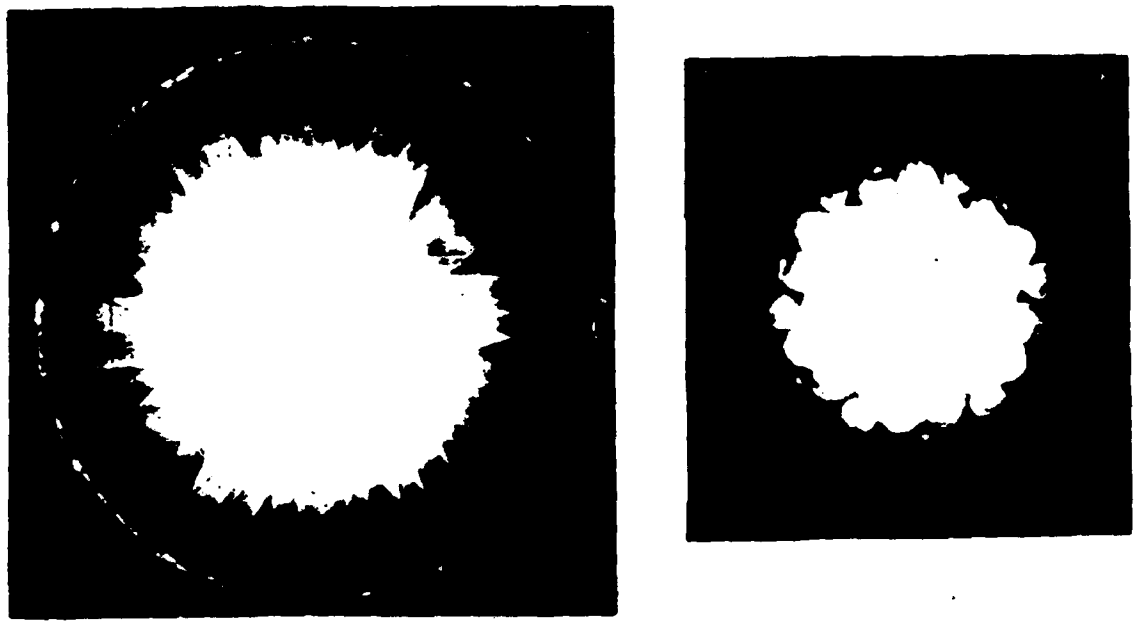
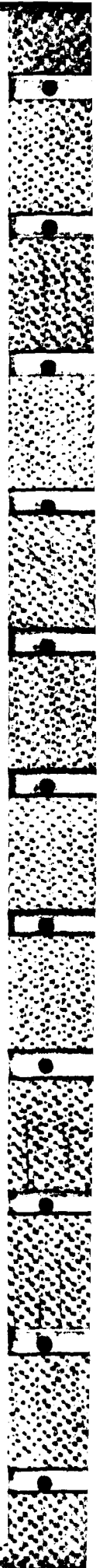


Fig. 60 Convergent beam pattern for the <111> zone axis in Al₁₂Mo.



6. DYNAMIC POWDER COMPACTION

In the first year's work, emphasis was placed on the compaction of rapidly solidified powders of Al-7091, which were fabricated by ALCOA and kindly supplied by Dr. H. Gegel of AFMAL. Of particular interest in this research is the response of the prior particle boundary regions to dynamic compaction. For example, to what degree has a good metallurgical bond been established. To explore this feature further, a model system was chosen for study. In particular, it is important to be able to identify the regions of the prior particle boundaries. For this reason, nominally pure Al powders ($< 44 \mu\text{m}$ diameters) were mixed with fine particulate of Y_2O_3 ($< 15 \mu\text{m}$ diameters). In this way, the prior particle boundaries would be marked by the chemically different particulate.

The mixture of powders were compacted using the device described in first annual report and foils for TEM were produced. Fig. 61 (a,b) shows two areas containing prior particle boundaries, which were identified by the presence of particles of Y_2O_3 . In addition to the deliberately added Y_2O_3 particles, other smaller inclusions may be observed. These latter inclusions may be seen more clearly in Fig. 62 (a and b), where they have formed in a sample in which no Y_2O_3 was added intentionally. The spatial distribution of these particles in this one grain of Al which straddles the prior particle boundary suggests that local melting in this region may have occurred. It is interesting to note that in all these Al compacts, the material appears to have recrystallized dynamically.

Small tensile samples were machined from the pieces of Al which had been dynamically compacted. The shape of the samples is shown in Fig. 63 and these do in fact conform with the standard specification of ASTM. The results obtained for both the as-compacted material and samples which had been heat-treated for two hours at 250°C are listed in Table 6. Although these values

Specimen	Tensile Strength	
	ksi	MPa
as-compacted	27.4	188.7
	27.7	191.0
heat-treated for 2 hours at 250°C	24.5	168.8
	26.6	183.7
	27.4	188.6
	28.1	193.7

Table 6

Tensile strengths for dynamically compacted powder of pure Al.

are similar to those expected from conventionally processed material (i.e. 30 ksi), none of the samples showed any significant ductility. The reason for the lack of ductility is probably related to the presence of oxide inclusions found at the prior particle boundaries in the compacted material. Examples of such particles may be seen in the micrographs in Fig. 64 (a-c). It should be noted that no degassing of the powders was performed in order to remove the hydration of the oxide layer that forms commonly on the surfaces of Al powders. Future work will involve degassing heat-treatments which may lead to improved ductilities in compacted samples.

Tensile specimens were also machined from dynamically compacted blanks of the alloy 7091. The results obtained from the as-compacted condition were rather disappointing both from the point of view of strength and ductility. Consequently, some test specimens were heat-treated for one hour either at 250° or 450°C, respectively. The results of all these tests are presented in Table 7. In addition, a test specimen of the same type as used for the compacted material was machined from a piece of extruded 7091, which had been kindly supplied by Dr. G.J. Hildeman of ALCOA. The strength of this sample is also included for comparison in Table 7. As can be seen from the table, the strengths of the dynamically compacted material is significantly lower than that of the extruded material. However, the powders of 7091 were produced by

Specimen	Tensile Strengths	
	ksi	Mpa
as-compacted	6.3	43.7
	9.8	67.8
heat-treated for 1 hour at 250°C	10.5	72.6
heat-treated for 1 hour at 450°C	33.8	233.0
	40.3	277.0
	40.3	277.0
as-extruded 7091	90.7	625.7

Table 7

Tensile strengths for dynamically compacted powders of 7091. Also included is a result for the tensile strength of extruded 7091 for comparison.

gas atomization and were not degased before compaction. It is thought that the low strengths are due to the lack of surface cleanliness and future work is being directed towards degasing of the particulate prior to compaction. Scanning electron micrographs of the fracture surfaces of the tensile samples of 7091 in the as-compacted condition and also the high temperature heat-treatment are shown in Fig. 65 (a,b). The fracture mode involving interparticle separation does not appear to change significantly with heat-treatment.

a)



b)



Fig. 61 Typical boundaries identified by presence of Y_2O_3 . These regions are along the boundary away from the oxide. The boundaries often outline particles as in a).

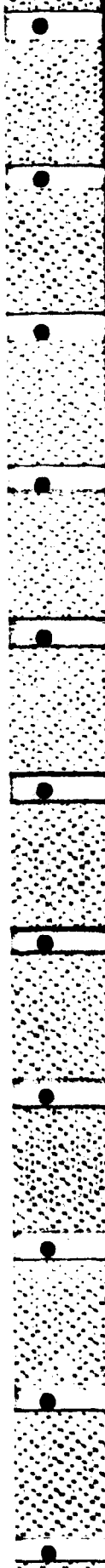


(a)



(b)

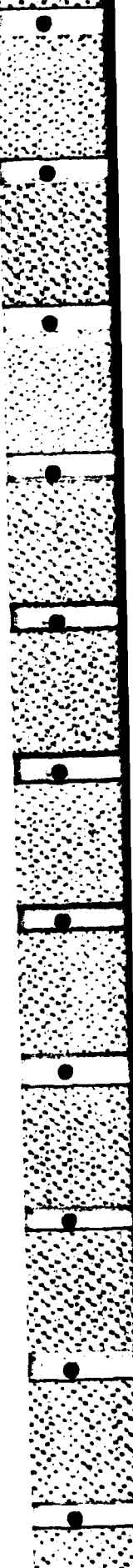
Fig. 62 A typical boundary. In a) a recrystallized grain traverses the boundary. b) Higher magnification image of the arrowed grain in a) showing apparent prior surface oxides.



ALUMINUM COMPACT TENSILE SPECIMENS



Fig. 63 Machined aluminum compact and compact tensile specimens.



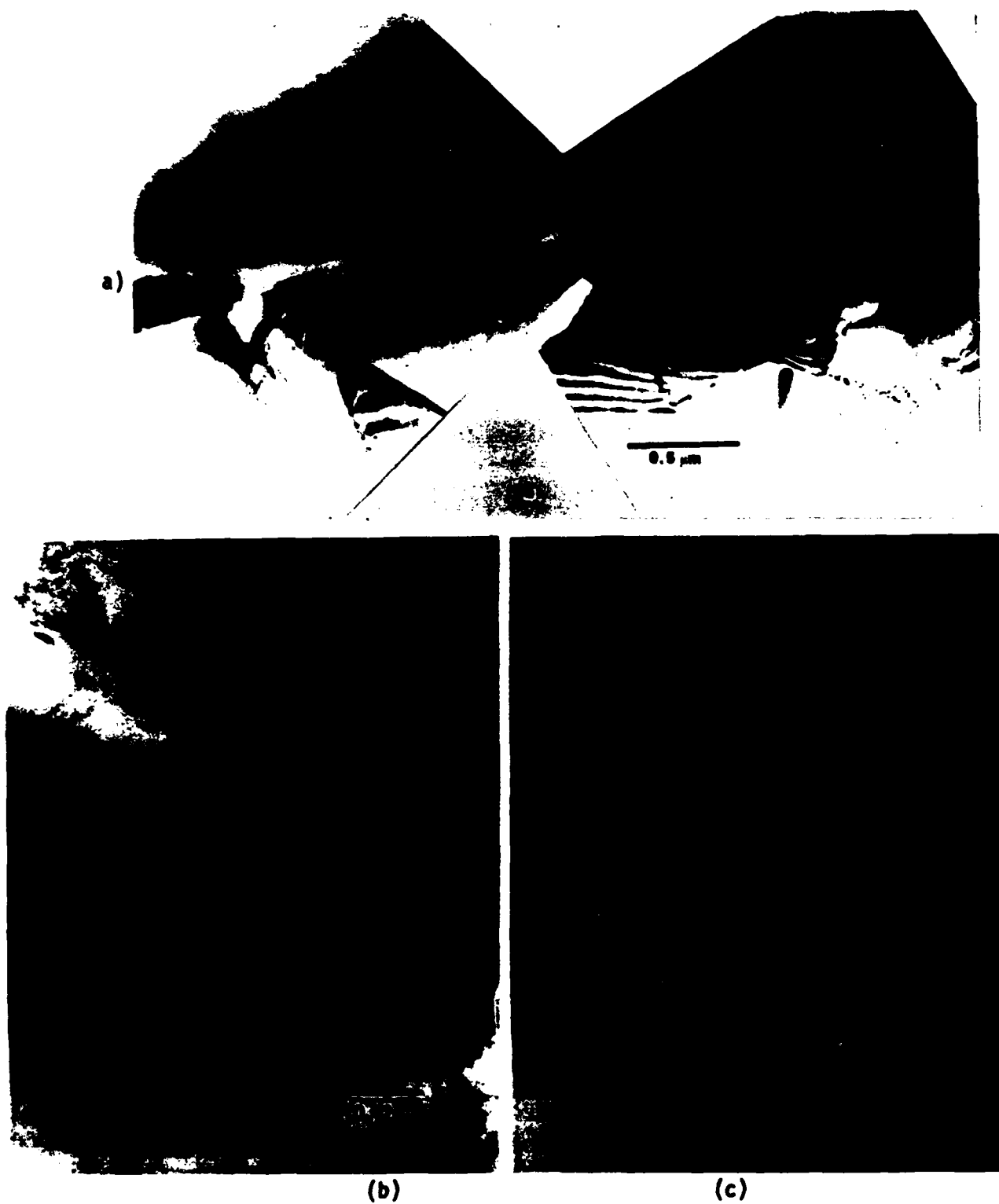
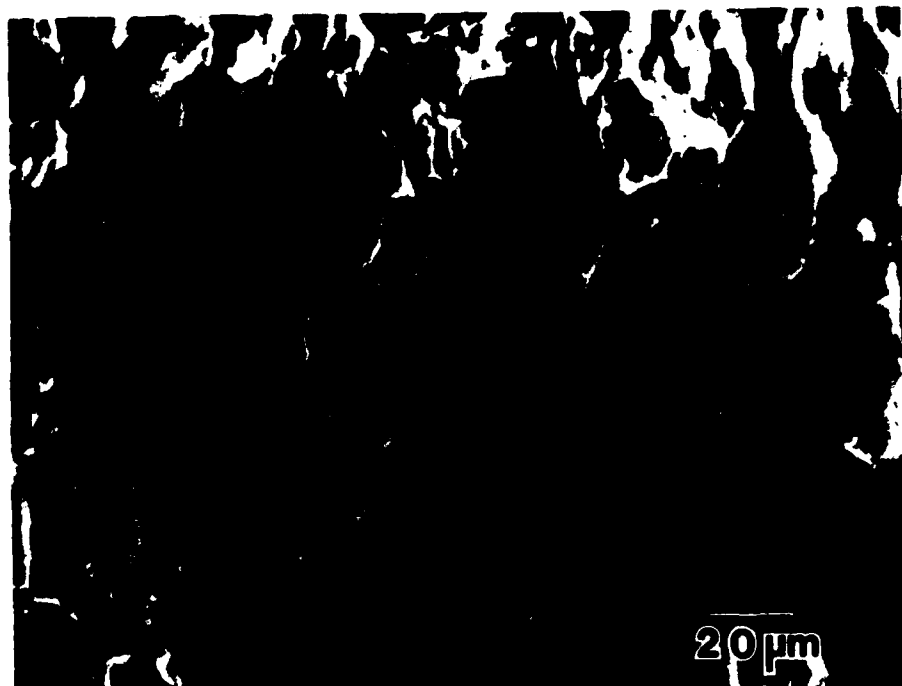


Fig. 64 a) A composite micrograph showing extent of boundaries.
b,c) Higher magnification of region in a) showing apparent prior surface oxides.

a)



b)

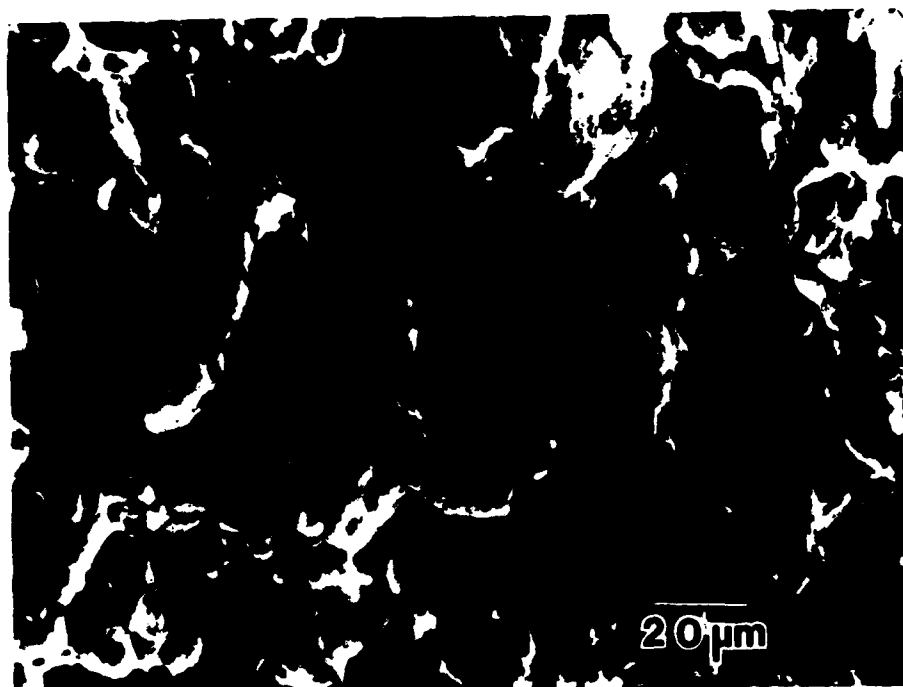


Fig. 65 SEM fractographs of 7091 Al compact tensile specimens of a) as compacted, b) heat treated 1 hr at 450°C. The fracture surfaces show little evidence of ductility in bonds.

7. PUBLICATIONS AND PRESENTATIONS

7.1 Publications from Present Work

- 1) J.W. Zindel, J.T. Stanley, R.D. Field, H.L. Fraser, "Microstructures of Rapidly Solidified Aluminum Alloys", Proceedings: Materials Research Society, Annual Meeting, Symposium F, Boston, MA, Nov. 14-17, 1983 (in press).
- 2) J.W. Sears, B.C. Muddle, H.L. Fraser, "Dynamic Compaction of Al Alloys", Proceedings: Materials Research Society, Annual Meeting, Symposium F, Boston, MA, Nov. 14-17, 1983 (in press).
- 3) J.W. Zindel, J.T. Stanley, R.D. Field, H.L. Fraser, "Rapid Solidification and Subsequent Analysis of Some Hypereutectic Al-Base Alloys", Rapidly Solidified Powder Aluminum Alloys, Proceedings: ASTM Symposium, Philadelphia, PA, April 4-5, 1984 (in press).
- 4) J.W. Sears, D.J. Miller, H.L. Fraser, "The Dynamic Compaction of Rapidly Solidified Al-Base Alloys", Proceedings: ASTM Symposium, Philadelphia, PA, April 4-5, 1984 (in press).
- 5) J.W. Zindel, J.T. Stanley, R.D. Field and H.L. Fraser, "Microstructural Comparison of Rapidly Solidified Al-Base Powders Produced by Laser Surface Melting, Melt-Spinning and Atomization", Proceedings: International Powder Metallurgy Conference, Toronto, Ontario, June 17-22, 1984 (in press).
- 6) M.J. Kaufman, J.T. Stanley, D.C. Van Aken, R.D. Field and H.L. Fraser, "Microstructure of Some Rapidly Solidified Al-Base Alloys", Proceedings: Fifth International Conference on Rapidly Quenched Metals, Wurzburg, W. Germany, Sept. 3-7, 1984 (in press).
- 7) D.C. Van Aken and H.L. Fraser, "The Microstructures of Rapidly Solidified Hyper-eutectic Al-Be Alloys", submitted to Acta Met.
- 8) R.D. Field and H.L. Fraser, "Precipitates in a Rapidly Solidified Al-Mn Alloy Possessing Icosahedral Symmetry", (submitted for publication: J. Mat. Sci. Eng. Letter).

7.2 Presentations Other Than Those Listed Above

- 1) R.D. Field and H.L. Fraser, "Microstructures of Rapidly Solidified Hypereutectic Al-Mn Alloys", AIME Fall Meeting, Detroit, MI, Sept. 16-20, 1984.
- 2) J.T. Stanley and H.L. Fraser, "The Effect of Undercooling on the Microstructure of Hypereutectic Al-Ni and Al-Co Alloys", AIME Fall Meeting, Detroit, MI, Sept. 16-20, 1984.
- 3) J.W. Zindel and H.L. Fraser, "Microstructural Analysis of Rapidly Solidified and Consolidated AlFeMo Alloys", AIME Fall Meeting, Detroit, MI, Sept. 16-20, 1984.

- 4) F.C. Grensing and H.L. Fraser, "A Comparative Microstructural Investigation of Al-Mo Alloys Processed Using Various RSP Techniques, AIME Fall Meeting, Detroit, MI, Sept. 16-20, 1984.
- 5) D.C. Van Aken and H.L. Fraser, "Rapid Solidification of Aluminum 2 Weight Percent Beryllium: A Microstructural Comparison of Laser Surface Treated and Melt-Spun Ribbon, AIME Fall Meeting, Detroit, MI, Sept. 16-20, 1984.
- 6) D.J. Miller and H.L. Fraser, "Microstructure Studies of Dynamically Compacted Material", AIME Fall Meeting, Detroit, MI, Sept. 16-20, 1984.

8. REFERENCES

1. H. Jones, 1969 *Matls. Sci. Eng.*, 5, 1.
2. C.M. Adam, R.G. Bourdeau and J.W. Broch, 1983, AFMAL-TR-81-4188.
3. E. Scheil and Y. Masuda, 1955, *Aluminium*, 31 51.
4. W.J. Boettinger, 1982, "Rapidly Solidified Amorphous and Crystalline Alloys", eds. B.H. Kear, B.C. Giessen and M. Cohen, Elsevier, New York, p. 15.
5. R.K. Garrett and T.A. Sanders, *Matls. Sci. Eng.*, 1983, 60, 269.
6. J.H. Perepezko and W.J. Boettinger, *Alloy Phase Diagrams*, 1983 (edited by L.H. Bennett, T.B. Massalski and B.C. Giessen), vol. 19, Elsevier, North-Holland.
7. D.J.H. Cockayne, I.L.F. Ray and M.J. Whelan, *Phil. Mag.* 20, 1265 (1969).
8. D.C. Van Aken and H.L. Fraser, submitted to *Met. Trans. A*.
9. D.J. Mazey, R.S. Barnes, and A. Howie, *Phil. Mag.* 7, 1861 (1962).
10. D.M. Maher and B.L. Eyre, *Phil. Mag.* 23, 409 (1971).
11. J.H. Perepezko, D.H. Rasmussen, I.E. Anderson and C.R. Loper, Jr., *Sheffield International Conf. on Solidification and Casting of Metals*, 1979, p. 169, Metals Society, London.
12. M.J. Kaufman and H.L. Fraser, accepted for publication *Int. J. Rapid Solidification* vol. 1, 1984.
13. J.W. Zindel, J.T. Stanley, R.D. Field and H.L. Fraser, to be published in *Rapidly Solidified Powder of Aluminum Alloys* (1984), ASTM publication, Philadelphia, PA.
14. Y. Nakagawa, *Acta Met.* 6, 704 (1958).
15. R.N. Grugel and A. Hellawell, *Met. Trans. A* 12A, 669 (1981).
16. R. Hultgren et al., *Selected Values of the Thermodynamic Properties of the Elements*, 1973, ASM, Metals Park, Ohio.
17. W. Haller, *J. Chem. Physics*, 42, 686 (1968).
18. J.W. Cahn and G. Kalonji, *Proc. Conf. Solid-Solid Phase Transformations*, 1982 (edited by H.I. Aaronson, D.E. Laughlin, R.F. Sekerka and C.M. Wayman), p. 3, AIME, Warrendale, Pa.
19. R.E. Anderson, private communication.

20. L. D. Marks, Phil. Mag. A, 49-1, 1984, pp. 81-93.
21. A. Howie and L. D. Marks, Phil. Mag. A, 49-1, 1984, pp. 95-109.
22. S. Harriague and H. Leibovich, Met. Trans. 2A, Dec. 1984, pp. 3485-3486.
23. Y. Fukano and C. M. Wayman, JAP, 40-4, March 1969, pp. 1656-1664.
24. S. Mader, J. Vac. Sci. Tech., 8-1, Jan/Feb, 1971, pp. 247-250.
25. Y. Saito, J. Cryst. Growth, 47, 1979, pp. 61-72.
26. K. Heineman, M. J. Yacaman, C. Y. Yang, and H. Poppa, J. Cryst. Growth, 47, 1979, pp. 177-186.
27. M. J. Yacaman, K. Heinemen, C. Y. Yang, and H. Poppa, J. Cryst. Growth, 47, 1979, pp. 187-195.
28. C. Y. Yang, J. Cryst. Growth, 47, 1979, pp. 274-282.
29. C. Y. Yang, M. J. Yacaman and K. Heineman, J. Cryst. Growth, 47, 1979, pp. 283-290.
30. E. Louis, R. Mora, J. Pastor, Met. Sci., 14-12, Dec. 1980, pp. 591-593.
31. Buxton, R.F., Eades, J.A., Steeds, J.W. and Rackham, G.M., Trans. R. Soc. London, 1976, A281, 171.
32. Pearson, W.B., "A Handbook of Lattice Spacings and Structures of Metals and Alloys, Pergamon Press, London, 2, 1967, p. 125.

20. L. D. Marks, Phil. Mag. A, 49-1, 1984, pp. 81-93.
21. A. Howie and L. D. Marks, Phil. Mag. A, 49-1, 1984, pp. 95-109.
22. S. Harriague and H. Leibovich, Met. Trans. 2A, Dec. 1984, pp. 3485-3486.
23. Y. Fukano and C. M. Wayman, JAP, 40-4, March 1969, pp. 1656-1664.
24. S. Mader, J. Vac. Sci. Tech., 8-1, Jan/Feb, 1971, pp. 247-250.
25. Y. Saito. J. Cryst. Growth, 47, 1979, pp. 61-72.
26. K. Heineman, M. J. Yacaman, C. Y. Yang, and H. Poppa, J. Cryst. Growth, 47, 1979, pp. 177-186.
27. M. J. Yacaman, K. Heinemen, C. Y. Yang, and H. Poppa, J. Cryst. Growth, 47, 1979, pp. 187-195.
28. C. Y. Yang, J. Cryst. Growth, 47, 1979, pp. 274-282.
29. C. Y. Yang, M. J. Yacaman and K. Heineman, J. Cryst. Growth, 47, 1979, pp. 283-290.
30. E. Louis, R. Mora, J. Pastor, Met. Sci., 14-12, Dec. 1980, pp. 591-593.
31. Buxton, R.F., Eades, J.A., Steeds, J.W. and Rackham, G.M., Trans. R. Soc. London, 1976, A281, 171.
32. Pearson, W.B., "A Handbook of Lattice Spacings and Structures of Metals and Alloys, Pergamon Press, London, 2, 1967, p. 125.

END

FILMED

1-85

DTIC